Cavitation in a Nozzle of Fuel Injector for Diesel Engine

RADITYA HENDRA PRATAMA

(Degree)
博士（工学）

(Date of Degree)
2016-09-25

(Date of Publication)
2017-09-01

(Resource Type)
doctoral thesis

(Report Number)
甲第6761号

(URL)
https://hdl.handle.net/20.500.14094/D1006761

博　士　論　文

Cavitation in a Nozzle of Fuel Injector for Diesel Engine

(ディーゼル機関の燃料インジェクタ内キャビテーション)

平成２８年０８月

神戸大学大学院海事科学研究科

RADITYA HENDRA PRATAMA

Doctoral Dissertation

Cavitation in a Nozzle of Fuel Injector for Diesel Engine

(ディーゼル機関の燃料インジェクタ内キャビテーション)

August 2016

Graduate School of Maritime Sciences

Kobe University

RADITYA HENDRA PRATAMA

DOCTORAL DISSERTATION

CAVITATION IN A NOZZLE OF FUEL INJECTOR FOR DIESEL ENGINE

RADITYA HENDRA PRATAMA

SUPERVISOR:
PROF. AKIRA SOU

GRADUATE SCHOOL OF MARITIME SCIENCES
KOBE UNIVERSITY
JAPAN
2016

Dedication

I would like to dedicate this dissertation work to my family, relatives, and friends. A deep gratitude to my parents, Hendro Saksanto and Susy Hariyati who always send me the best prayer for my future and a word of encouragement. Thanks to my brothers and sister, Yoyok Suksmo Indiarto, Ira Hendrawardhani, and Alan Hendrowicaksono who always support in my difficult time, and send me photos of them with their families from Indonesia which are so special to me. Special thanks to the special one, for supporting me until the end of this work. Last but not least, I would like to dedicate this dissertation to Allah, The Creator of the universe, to show Him my deepest gratitude for giving me a chance to learn (probably) the smallest thing of His knowledge.

Acknowledgement

I would like to express my gratitude to everyone who supports me to finish this dissertation and all of the works in my doctoral course program. Special gratitude to Prof. Akira Sou as my supervisor for my studies in student exchange, master, and doctoral course programs for 6 years. I would like also to express my gratitude to Prof. Shigeru Nishio and his students, Mr. Shibata, Ms. Nishimura, and Mr. Aizawa from Naval Architecture Laboratory and also Prof. Tokihiro Katsui from Fluid Dynamics Laboratory for their cooperation in this research so I can present some results of PIV analysis and CFD simulation into this dissertation. I would like also to thank Prof. Tomohisa Dan for being one of the reviewers in my final doctoral defense. Special thanks to Dr. Hideaki Yokohata and Mr. Yoshitaka Wada from Mazda Motor Corporation for their supports and advises regarding nozzle designs as well as for the research funds. I would like also to thank Prof. Keiya Nishida, Prof. Akira Nakashima, Dr. Min Guo, and Mr. Nagisa Shimasaki from Hiroshima University for their cooperation in this research so I can present some results of stereoscopic PIV analysis into this dissertation. Thanks to Photron and Kanomax for lending us a high speed camera and supporting us in some visualization experiments. Thanks to Mr. Hatai from Mizuho Chemical and Mr. Ao from Kobe Engineering for their cooperation in nozzle design and production. Thanks to all of the members in experiment team: Mr. Sugimura, Mr. Ohashi, Mr. Takano, Mr. Shimoda, Mr. Tomisaka, Mr. Mashida, Mr. Kibayashi, Mr, Egawa, Ms. Uzawa, Mr. Nakatsu, Mr. Yamada, Mr. Rubby, Mr. Kasahara, Mr. Nakano, Mr. Kotani, and Ms. Horie. Thanks to Mr. Komuta and Mr. Matsubara for their supports during the experiment. Thanks to all of my colleagues in Energy & Fluid Science Laboratory and Kobe University who support my study and share their time to let me feel comfortable to study in this university. I would like also express my gratitude to Ministry of Education, Culture, Sports, Science and Technology (MEXT) of the Japanese Government, Kobe University, and Dr. Nobuko Umeki for supporting my financial and research funds.

Abstract

With the stringency of regulation of diesel engine exhaust gas emission, a large effort has been paid to decrease the exhaust gas emissions by improving the combustion quality and to increase diesel engine thermal efficiency. According to the previous studies, cavitation occurs in a nozzle of diesel fuel injectors and it enhances fuel spray atomization, which leads to a better mixture of fuel and air, a better combustion, and a clean exhaust gas. However, the way to quantitatively predict cavitation in a fuel injector with complicated geometry and how it affects the injected liquid jet have not been clearly understood yet.

In this study, experiments on cavitation in a large scale of transparent two-dimensional nozzles and cylindrical nozzles with symmetric or asymmetric inflows and simplified or real geometries were conducted to understand the mechanism and condition of cavitation occurrence in Valve-Covered Orifice (VCO) nozzle and mini-sac nozzle, which are generally used in diesel engines. Visualizations were conducted to clearly capture the cavitation inside the nozzle and the jets by using a digital camera or a high-speed camera. Particle image velocimetry (PIV) analysis was conducted to understand internal flow characteristics in the nozzle-hole and sac part.

Cavitation in a two-dimensional nozzle, whose geometry represents a VCO nozzle, with an asymmetric inflow and various needle lifts was visualized to investigate the effects of transverse inflow on cavitation and liquid jet. The result shows that cavitation and the jet occur asymmetrically especially when needle lift is low. The low needle lift increases the thickness of the separated boundary layer and cavitation, and thus liquid jet injection angle. Quantitative analysis by means of the modified cavitation number, which is based on local pressure at vena contracta, can predict the onset and development of cavitation in the asymmetric nozzle.

Visualization and numerical simulation of cavitation in a single cylindrical nozzle with an asymmetric inflow at various needle lifts and upstream-volume width were carried out to understand the internal flow of VCO nozzle. As a result, the formation of a string cavitation and a swirling hollow cone liquid skirt were found to take place at low needle lift with large lateral momentum. After all the observation, the string cavitation regime maps were derived. By using this map for given upper-volume width, the cavitation regime can be predicted based on mean flow velocity in the nozzle hole and needle lift ratio under the atmospheric pressure condition.

Visualization of large scale two-dimensional mini-sac nozzles was conducted to understand the effects of nozzle geometries, i.e. the needle geometry including its angle and the needle lift, and the sac geometry including sac depth, sac radius, nozzle hole position, and nozzle angle. Particle image velocimetry (PIV) analysis was conducted to see the flow inside the sac and nozzle, vortex flow at the nozzle exit, as well as to evaluate the turbulence intensity in the sac and nozzle. The results clarified that a flow fluctuation in the sac, especially in the nozzle-hole upstream, induces unsteady cavitation in the nozzle-hole. Not only the cavitation thickness but also the liquid jet angle fluctuates largely, especially when

the needle lift is low and needle angle is large due to the unsteady inflow caused by complex sac geometry. The averaged PIV result showed an obvious correlation between the inflow angle at the nozzle inlet edge and the cavitation thickness, which determines contraction coefficient, cavitation length, turbulence intensity, and jet angle. It was found that vortex flow occurs as a result of cavitation shedding from the reattachment point, which increases jet angle. It was clarified that recirculation flow velocity in the sac is higher for a nozzle with a smaller sac than that in a larger sac, which may cause string cavitation in mini-sac nozzles.

Cavitation in a scaled-up 3-holes mini-sac nozzle with various needle lifts was visualized. The refractive index matching by mixing sodium iodide into the water was adopted for stereoscopic PIV analysis in the sac where string cavitation occurs. The results revealed string cavitation occurs at the core of a recirculation flow in the sac.

This study concluded that two-dimensional (2D) nozzles and simplified nozzles give us a clear knowledge on cavitation in complex fuel injector. The results provide us a new design strategy of fuel injector, i.e. by controlling the angle and turbulence intensity of the inflow into a nozzle we can control cavitation to enhance fuel spray atomization for clean combustion.

Table of Contents

List of Tables

List of Figures

List of Symbols

Roman Symbols

A : Cross-sectional area of two-dimensional nozzle-hole

c : Concentration of sodium iodide solution

C_d : Coefficient of discharge

D : Diameter of nozzle-hole

D_{SC} : Diameter of string cavitation

D_{SC}' : Diameter of string cavitation before correction

D_{SC}^* : Ratio of string cavitation diameter

D_H : Hydraulic diameter of nozzle-hole

H_S : Height of sac (2D mini-sac nozzle)

L : Length of nozzle-hole

L_{SN} : Length between needle-seat corner to nozzle inlet corner (2D mini-sac nozzle)

L_C : Length of cavitation

m_{H2O} : Mass of water

m_{NaI} : Mass of sodium iodide

n : Refractive index of sodium iodide solution

P_b : Back pressure

P_v : Vapor pressure

Re : Reynolds number

R_S : Radius sac (2D mini-sac nozzle)

r : Radius of nozzle inlet

S : Needle lift (2D mini-sac nozzle)

T : Temperature of liquid

t : Thickness of nozzle plate (2D nozzle)

V : Mean flow velocity

V_{in} : Velocity of upstream flow

V_{SupCav} : Velocity at super cavitation condition

W : Width of nozzle-hole

W_C : Width of cavitation (cavitation thickness)

W_c : Width of core flow

W_{UL} : Distance from nozzle left wall to upstream left-end wall (asymmetric 2D Nozzle)

Z : Needle lift (cylindrical nozzle)

Greek Symbols

α : Void fraction

γ : Surface tension

θ : Total jet angle

θ_L : Left jet angle

θ_R : Right jet angle

θ_N : Nozzle angle

θ_{Ne} : Needle angle

θ_{SupCav} : Total jet angle at super cavitation condition

λ : Friction coefficient

σ : Cavitation number

σ_C : Modified cavitation number

μ : Dynamic viscosity

ν : Kinematic viscosity

ρ : Density

Abbreviations

2D : Two-Dimensional
3D : Three-Dimensional
CFD : Computational Fluid Dynamic
HIC : Helical-Flow Induced Cavitation
IHF : Imperfect Hydraulic Flip
LDV : Laser Doppler Velocimetry
PIV : Particle Image Velocimetry
RIC : Recirculating-Flow Induced Cavitation
SBL : Separated Boundary Layer
THC : Total Hydraulic Flip
VCO : Valve Covered Orifice

Chapter 1
Introduction

1.1 Background

Most of the people in the world today are satisfied with the convenience of energy and technology-based devices in their daily life. One of the reliable devices as a power generator which is very useful to fulfill the human demand in many aspects is a diesel engine. The diesel engine has been improved on its features as well as its main works. One of the most important matters in the diesel engine is thermal efficiency, that many researchers have paid their effort to improve the thermal efficiency of diesel engine, Hence a lot of works have been done to improve the atomization process of fuel spray in a diesel engine. Yet a lot of matters have not been clearly revealed and remain as a 'mystery'. To improve the diesel engine thermal efficiency and reduce exhaust gases, the internal flow in fuel injector has been investigated.

The emission from a combustion engine is one of the causes of air pollution which affects environment and climate on the Earth. A lot of parties are involved to reduce exhaust emissions from diesel engines by the regulation approach and technological approach. Regulations which limit the amount of flue gasses produced by the engine are being stringent. In Europe, the European Union (EU) sets the standards of exhaust gas emissions for all road vehicles, trains, barges, non-road mobile machinery, airplanes, and ships. The EU has introduced Euro 6 for diesel vehicles which is effective from September 1, 2014 [1]. Figure 1.1 shows a simplified chart depicting the progression of European emission standards for Diesel passenger cars.

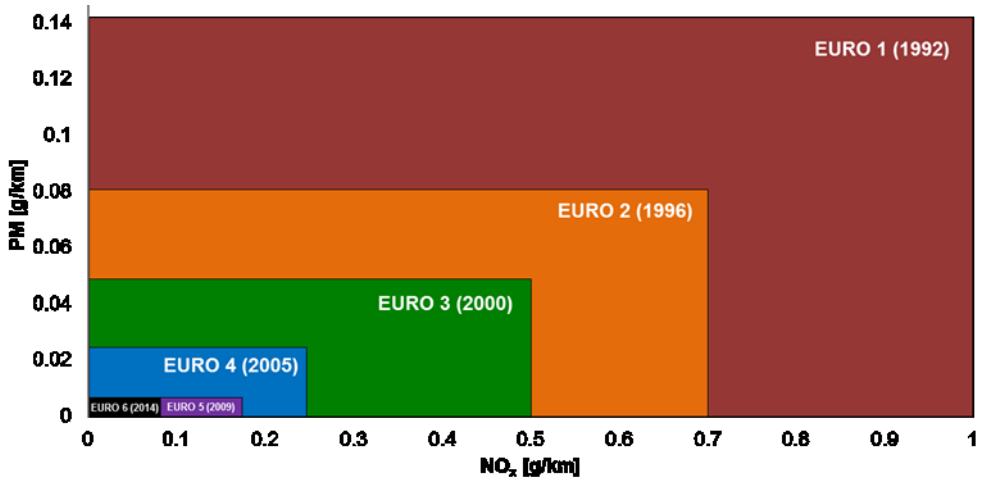

Figure 1.1 Progression of European emission standards for Diesel passenger cars

Due to the stringency of the exhaust gas emission regulations which come into force in many countries, there is no other choice but to improve the combustion quality and decrease the exhaust gas emissions. From the technological approach, various studies have been done

to meet the exhaust emission standards. Emission reduction can be obtained by several ways, e.g. selective catalytic reduction (SCR), combustion improvement, alternative fuel, etc. The spatial and temporal distributions of fuel droplets as well as droplet size distribution in the combustion chamber determine the quality of the combustion. If fuel is not well distributed in the combustion chamber, the combustion does not occur completely and produces a dirty exhaust.

According to the basic knowledge on the fuel spray atomization process, it can be concluded that a good atomization leads to a good combustion with high thermal efficiency and cleaner exhaust gas with less PM emission. The fine spray as a result of good atomization is considered as a good spray since its surface area in contact with hot air is large, thus it leads to a good mixture preparation, and results in ideal combustion. A lot of efforts have been paid to improve the quality of atomization, such as the modification of the injector shape and the combustion chamber shape. According to the previous studies, cavitation occurs in the injector, and enhances the spray atomization process. Knowing the effects of cavitation in the nozzle of fuel injector helps the fuel injector manufacturer to design a better injector.

1.2 Cavitation

Cavitation is a two-phase phenomenon, i.e. gas appears in a liquid body. Cavitation is called as “cold boiling” that the formation of vapor occurs without any heating. Cavitation usually occurs at a separation point where a moving liquid gets accelerated which leads to an increase of dynamic pressure and decrease of static pressure. Cavitation occurs as a result of local pressure drop below the vapor saturation pressure.

Cavitation usually occurs at the inlet of a fluid-line component, where a sudden contraction takes place. As illustrated in Figure 1.2, in an axisymmetric nozzle, fluid pressure may drop below the vapor pressure at the nozzle inlet due to the decrease of local static pressure and results in cavitation in the recirculation zone. It explains the occurrence of cavitation phenomenon in a nozzle of fuel injector observed in several studies which are explained later.

Studies of cavitation are included in physics and engineering fields. In physics field, a lot of researchers have worked with this phenomenon in the area of cavitation and bubble dynamics. The formation of a bubble and the collapse of a bubble in incompressible fluid were first formulated by Rayleigh in 1917 [2]. It was formulated by taking into account the internal and external pressures to calculate the spherical bubble growth and collapse. Further study on bubble formation and collapse in a moving fluid was developed by Plesset in 1949. [3] It was defined in the paper that there are three regimes of liquid flow over a body, i.e. non-cavitating flow, cavitating flow with a small number of cavitation bubbles in the field of flow, and cavitating flow with a single large cavity about the body. Numerical and experimental studies were conducted by examining the results on the second regime, i.e. cavitating flow with a small number of cavitation bubbles in the field of flow. Figure 1.3 shows experimental images of the three regimes of cavitation flow, as reported in the paper [3]. Studies on cavitation and bubble dynamics including phase change, nucleation, bubble dynamics, bubble

collapse, dynamics bubble oscillation, translation of bubbles, homogeneous bubbly flows, cavitating flows, and free streamline flows, were discussed in detail by Brennen [4].

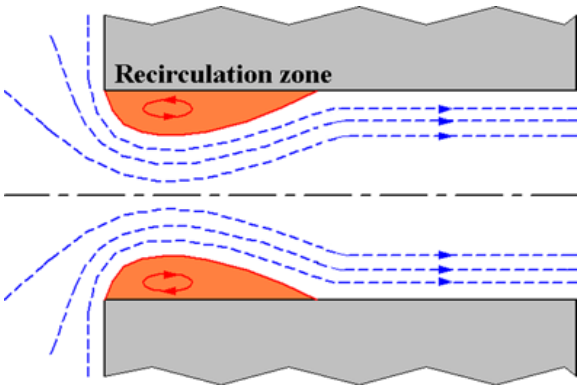

(a) Streamlines along the nozzle for an axisymmetric nozzle (Payri et al.) [5]

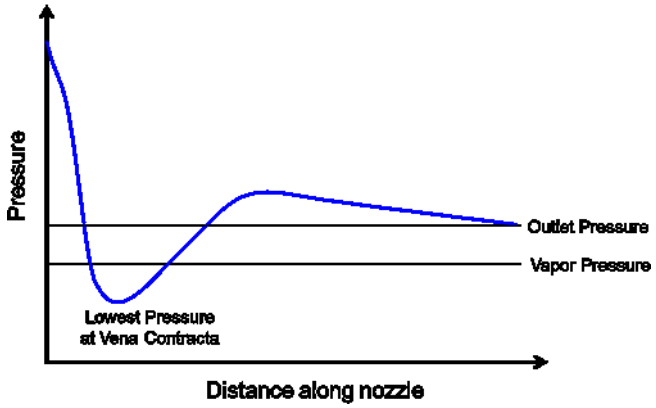

(b) Pressure along the axisymmetric nozzle

Figure 1.2 Streamlines and pressure along a nozzle

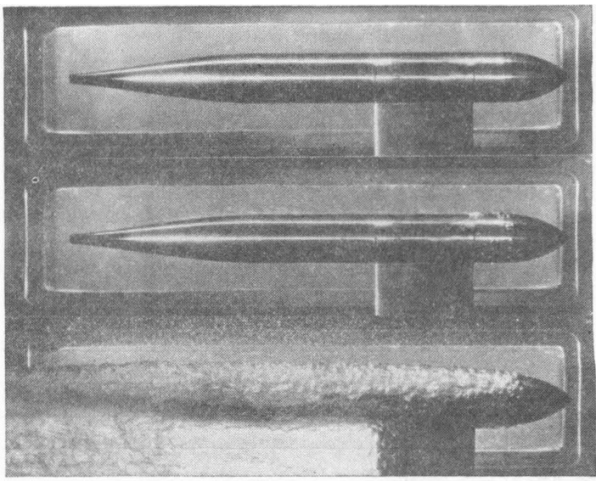

Figure 1.3 Images of three regimes of flow (Plesset) [3]

Cavitation in vortical structures, so-called vortex cavitation, is usually found on the blade surfaces of propeller or impeller. As stated by Arndt that vortex cavitation often occurs

in the cavitation inception process in many turbulent flow cases [6]. When the static pressure in the core of a linear vortex is decreased below the liquid vapor pressure due to a large vortex circulation, a small bubble or nucleus will grow in this region. The growing bubble in the core of a linear vortex is called as vortex cavitation. If bubble enters to a long vortex core, the initially almost spherical bubble expands following the vortex core axis and becomes a long vortex cavitation bubble. Vortex cavitation usually occurs in a concentrated region of vorticity, e.g. in the tip regions of lifting surfaces (fin, rudder, etc.). An example of image of collapsing vortex cavitation is shown in Figure 1.4 as reported by Choi et al [7]. In mini-sac nozzle of a fuel injector, vortex cavitation is observed in the sac part. It usually occurs from the nozzle hole elongated trough the sac part and connects to other nozzle-hole. The term 'string cavitation' is commonly used in this field.

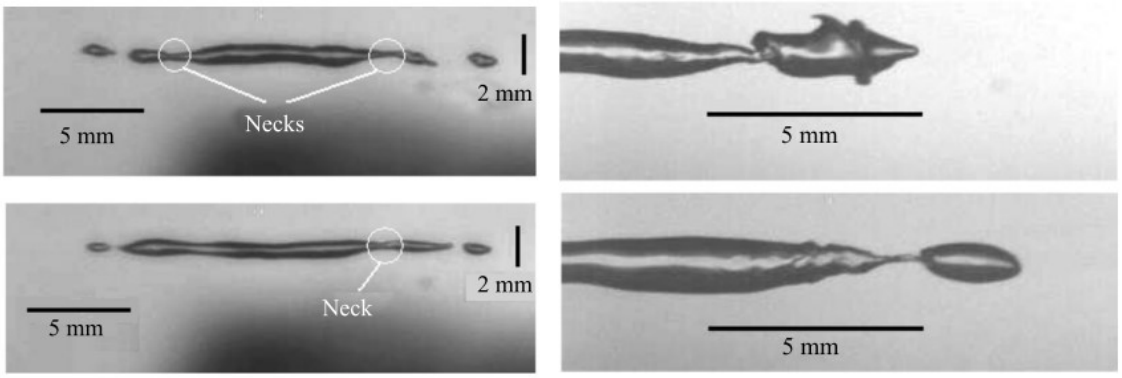

Figure 1.4 Collapsing vortex cavitation bubbles (Choi et al.) [7]

In the engineering field, cavitation is investigated to understand its behavior as well as its effects on the surrounding materials. It is well known that cavitation induces erosion which has to be avoided in most cases. One of the most cited studies on cavitation erosion was done by Philipp and Lauterborn by conducting an experiment on single bubble collapse and its effect on surface-damage of a metal specimen. The results conclude that the destructive effect of cavitation is mainly caused by the bubble collapse near the solid surface. The damage occurs when the initial bubble distance to the solid surface is less than twice of its maximum radius. Figure 1.5 shows an image of cavitation bubble dynamics in the vicinity of a solid boundary as reported in the paper [8].

Another research on cavitation has been done by Chan to investigate its occurrence in pump impellers as shown in Figure 1.6. In the paper, the minimum net positive suction head (NPSH) was defined as an indicator to evaluate the risks of erosion [9]. Cavitation erosion on a controllable pitch propeller (CPP) blade was examined by experiment and numerical simulation by Bertetta et al., which confirmed the numerical predictions became a very useful tool for the future propeller design. One of experimental and numerical result images is shown in Figure 1.7 [10].

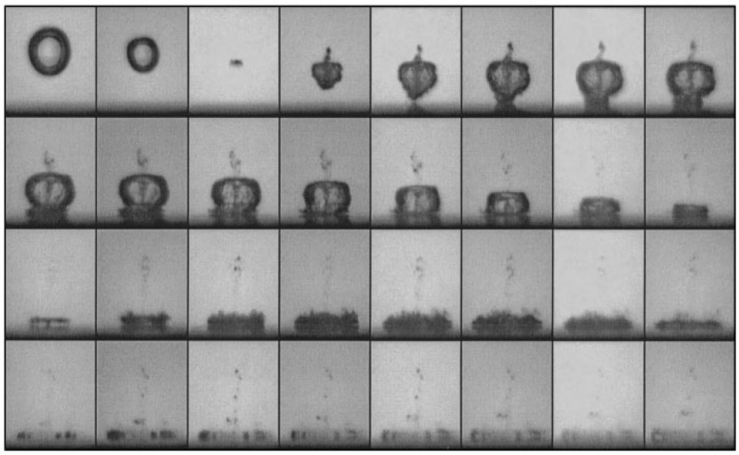

Figure 1.5 Cavitation bubble dynamics in the vicinity of a solid surface (Philipp and Lauterborn) [8]

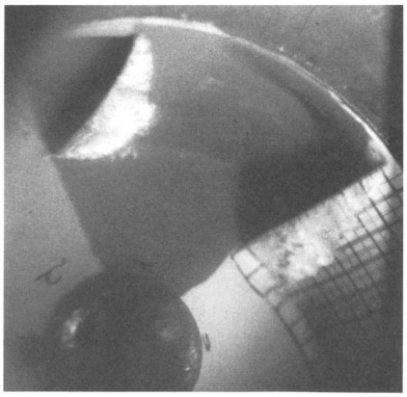

Figure 1.6 Cavitation form at 1450 r/min and NPSH = 11.5 m, as reported by Chan [9]

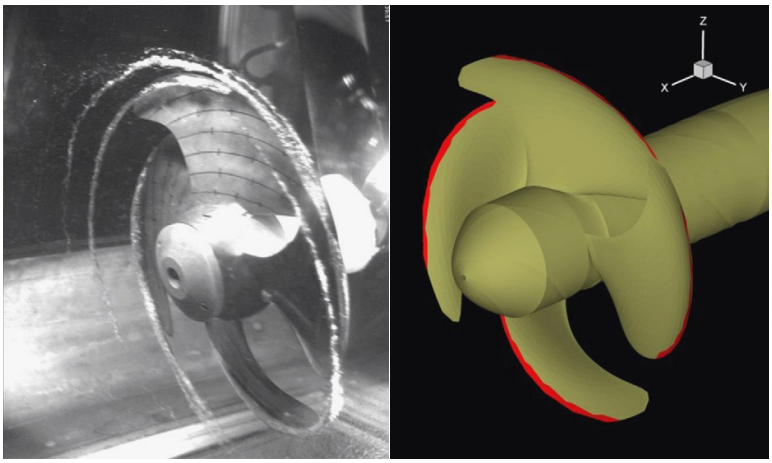

Figure 1.7 Observed and predicted cavitation extent on a propeller (Bertetta et al.) [10]

Special attention on cavitation phenomena in a nozzle of fuel injector has been paid. In the previous discussion, drawback effects of cavitation phenomena were focused, while in a nozzle of a fuel injector positive effect of cavitation to enhance jet deformation and fuel atomization is also examined. Moreover, a lot of researchers have paid their efforts to

understand cavitation in a nozzle and the spray characteristics both by experimental work and numerical simulation. The detail discussion of cavitation in a nozzle of fuel injector will be explained later.

1.3 Diesel Fuel Injector

Diesel engines performance is influenced by their combustion quality which is affected by fuel injection system. As we know, the aim of the injection system is to inject fuel into the combustion chamber of a diesel engine. The fuel characteristic, especially related to the atomization process, determines the engine performance, emission, and noise. The diesel fuel injection system works at extremely high injection pressures. It means that the materials and system components should be selected to endure the high pressures so it can perform for the designated lifetime and provide reliability for overall diesel engine system. Since the nozzle size is small, the manufacturing precision is strict. In addition, diesel injection system requires detail control requirements.

In order to achieve that goal, the proper injection timing must be set. In order to meet power output requirement, the amount of injected fuel must be controlled. However, accurately injecting a proper amount of fuel at proper injection timing is still not enough to achieve good combustion. Other factors are also important to provide a proper fuel spray, i.e. fuel atomization, bulk mixing, and air utilization. By atomizing fuel into very small fuel droplets, good quality of combustion will be achieved because fine particles let all the injected fuel vaporized The remaining fuel-liquid droplets burn poorly or flow out of the engine. That is why fuel atomization becomes a primary design parameter for the diesel fuel injection system. While fuel atomization is very important in diesel combustion, providing sufficient oxygen for the evaporated fuel during the combustion process is also required to get good combustion quality and reach optimum engine thermal efficiency. The proper amount of oxygen supplied by the intake air is required and it must be mixed with the fuel in order to get a complete combustion. Air utilization during the injection process is one of the most important factors to get good combustion. Air utilization means the optimization of utilizing the provided compressed air in the combustion chamber by letting the injected jet mix with it. There are many ways to optimize the air utilization, one of which is by dividing the injected fuel into several jets. This method will directly connect to fuel injector design, that is, the proper multi-hole nozzle design should be done [11].

In diesel engines, since direct injection of a fuel plays a main role in the diesel combustion, a lot of factors are investigated to inject an ideal fuel spray which leads to improvement in the efficiency of diesel engines. Moon et al. investigated the air entrainment, fuel evaporation and mixing process of diesel sprays injected from micro-orifices for direct-injection diesel engines. They analyzed the mixture formation process by using a laser absorption scattering (LAS) technique in order to provide the information of quantified liquid and vapor mass concentration, entrained air concentration and equivalence ratio [12]. Villermaux et al. analytically and experimentally investigated the ligament-mediated of spray formation [13]. Potz et al. explained the nozzle geometry effect on spray and combustion.

They mentioned about that the geometries of nozzle-hole, sac hole, and needle seat, as well as their precisions, affect the spray characteristics which determine the quality of combustion and exhaust gas emission. The diesel injectors have multi injection holes. There are two types of standard multi-hole nozzle, i.e. sac type and valve covered orifice (VCO) nozzle. Figure 1.8 illustrates the nozzle type based on their sac shape and volume. The figure also shows a qualitative explanation about the advantage of each nozzle type that the smaller sac-hole volume enhances its advantage in hydrocarbon emissions while the larger sac-hole volume improves the spray symmetry and has a robust design [14]. Another study told us about the development of diesel injection system. As explained by Mahr in his paper, nozzle geometries have a strong influence on emission as shown in Figure 1.9. The spray-hole geometry has a strong influence on soot and NOx while sac-hole geometry has a strong influence in hydrocarbon. Moreover, seat geometry has a strong influence on noise [15].

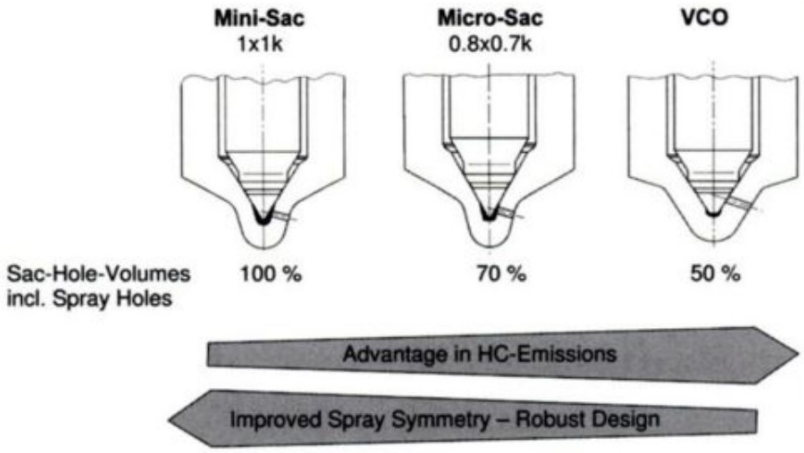

Figure 1.8 Comparison of mini-sac hole, micro-sac hole, and VCO nozzle (Potz et al.) [14]

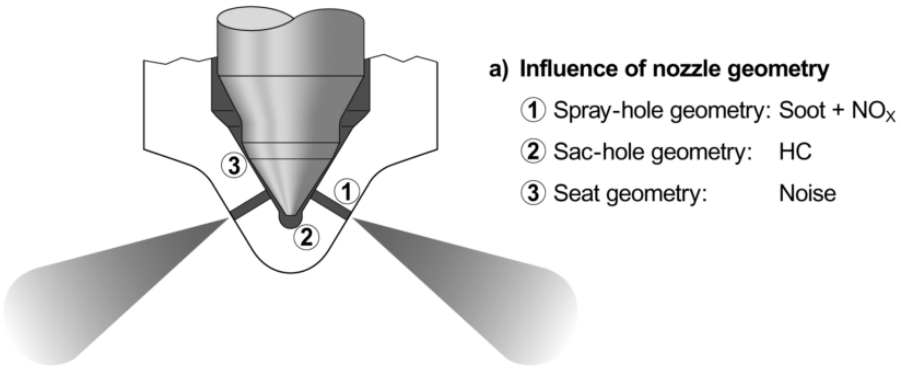

Figure 1.9 Influence of nozzle geometry on exhaust gas emissions (Mahr) [15]

1.4 Cavitation in Diesel Fuel Nozzle

It has been pointed out by Bergwerk [16] that cavitation occurs in a nozzle of a liquid injector, e.g., a fuel injector for a diesel engine and gasoline engine, and affects the injected spray characteristics. Before the study, it has been considered that the aerodynamic effect

plays the most important role in the injected fuel breakup. The cavitating flow in the nozzle is known to play the primary effect on fuel atomization and thus, cavitation phenomenon inside the nozzle is one of the main factors which play an important role in the diesel combustion process. Since the fuel atomization process is only well understood at low and medium velocity, further investigation is required in the range of velocities employed in the diesel nozzle in which no general understanding exists. Furthermore, the action of surrounding gas and the initial ruffling of the jet surface induced by the nozzle have to be taken into account at any fundamental theory of jet breakup in diesel nozzle [16]. Principal characteristics of diesel fuel spray which govern the diesel combustion, i.e. spray angle, spray tip penetration, droplet size, and their fluctuation during the nozzle fuel injection, should be taken into account as a basic consideration in diesel fuel spray atomization analysis.

1.4.1 Cavitation in Large Nozzle

The work on cavitation in fuel injector was started by Bergwerk [16] by using a simplified scaled up symmetric nozzle with water and fusus oil as the liquid to visualize the cavitating flow and the jet phenomena, and also to find the critical pressure of non-cavitating flow (today we call this flow as hydraulic flip), as well as the discharge coefficient. As we can see in Figure 1.10, this work introduces us the effect of cavitation on the initial ruffling of the jet surface as well as hydraulic flip in a simplified large symmetric nozzle.

The relation between cavitation and the spray was clarified through a visualization of a symmetric scale-up nozzle of 4 mm in diameter by Hiroyasu et al. [17], [18]. The utilization of the large scale transparent nozzle allows us to observe cavitation occurring in a nozzle. Although a large-scale nozzle does not exactly represent an actual nozzle, approach is useful to visualize cavitation which can be seen by naked eye or other optical aid tools. Not only the cavitation but also liquid jet can be clearly observed in the experiments. It reveals that development of cavitation from the inlet to near of the nozzle exit, which is often called super cavitation [19], enhances liquid spray atomization.

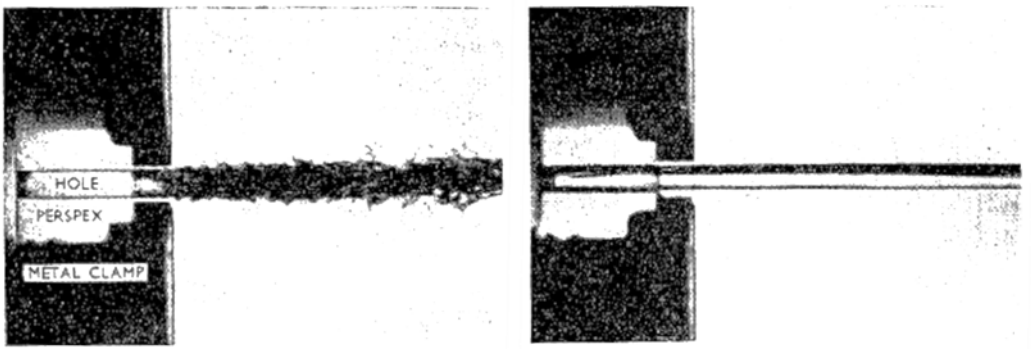

Figure 1.10 Photograph by transmitted light of discharge from the scaled-up orifice (Sac diameter 10 mm. Liquid: Shell fusus oil) (Bergwerk) [16]

Experiment by using large scale simplified geometry was conducted by Ganippa et al. [20] to understand the cavitation in nozzle with asymmetric inflow and the jet. They also

examined the effect of nozzle angle by varying the nozzle angle to 90°, 85°, 80° and 0°. The visualization results were used to describe the cavitation and the spray pattern qualitatively.

Experiment by Stanley et al. [21] by using large scale nozzle was done to visualize periodic cavitation shedding in a cylindrical orifice with L/D = 4.85 by a high-speed visualization. Refractive index matching was done to improve the cavitation visualization in the orifice. No peak frequencies were identified in the spectrum. Another work by the authors was done by using a cylindrical orifice with L/D = 5 to simply show the relation between cavitation number and normalized cavitation length in the nozzle. They measured the nozzle axial velocity near the nozzle exit by using Particle Image Velocimetry (PIV) analysis [22].

The work by He et al. [23] uses 5-times scaled-up transparent VCO nozzles with different length–diameter ratios (L/D = 4, L/D = 6 and L/ D = 8) to visualize and study the cavitation characteristics of diesel and biodiesel fuels. This work investigates the cavitation occurrence and the spray cone angle for the six different conditions, and the results confirms that biodiesel was more difficult to cavitate than diesel and the longer the nozzle orifice is, the weaker cavitation becomes in the orifice, because biodiesel has larger density, viscosity, and surface tension with lower vapor pressure than diesel.

1.4.2 Cavitation in Simplified Geometry Nozzle

Sou et al [24]–[26] conducted a high-speed visualization and LDV (Laser Doppler Velocimetry) measurement of turbulent cavitation flow in two-dimensional (2D) symmetric nozzles [24], [26] and a symmetric cylindrical nozzle [25]. Figure 1.4 shows the distribution of mean liquid velocity in a 2D nozzle by LDV measurement [24]. It shows the velocity in the nozzle. The studies clarified that cavitation clouds are shed from the tail of a recirculation zone filled with cavitation film, which induces a large deformation of a discharged liquid jet. The cavitation occurs due to the recirculation flow, in which flow separation occurs at the nozzle inlet. From this work, cavitation and liquid jet are classified into some regimes, i.e. no cavitation with wavy jet, developing cavitation with wavy jet, super cavitation with spray, and hydraulic flip with flipping jet as shown in Figure 1.5 [24]. Liquid jet deformation depends on cavitation regime, i.e., ligament formation and spray angle are affected by the normalized cavitation length. Cavitation and liquid jet near the nozzle exit are not strongly affected by the Reynolds number but by the cavitation number.

Ramamurthi and Patnaik [27] conducted an experiment in a simplified scaled-up symmetric sharp-edged nozzle to understand the influence of periodic flow disturbances on the formation of cavitation. The pressure drop and discharged coefficient of two various nozzle length to diameter ratio (L/D), i.e. L/D = 2.5 & 5 were compared in the study. Following the works by Sou et al, similar works have been done to visualize the cavitation in nozzle with simplified geometry and the jet. Park et al. [28] and Suh et al. [29] conducted experiments in symmetric planar single hole nozzle with large scaled to investigated the effects of nozzle length ratio (L/W) on cavitation development and the resulting atomized jet. They conducted a droplet measurement by utilizing phase Doppler particle analyzer (PDPA) to get the droplet Sauter mean diameter (SMD). Suh et al. investigated cavitation in simplified

geometry of scaled-up symmetric single-hole nozzle by varying fuel type, i.e. diesel and biodiesel fuels, as well as tapering the nozzle to see its effects on cavitation and the jet [30]. The recent work was done by Hult et al. in which investigation of interior flow and near-nozzle spray development in a marine-engine diesel fuel injector was done to examine the characteristics of fuel flow in a simplified marine diesel injector with 2 holes of 0.8 mm in diameter, L/D = 5, and 78° and 58° in nozzle angle [31]. Mauger et al. [32], [33] conducted visualizations of a quasi-2D channel flow to understand the pressure drop in the channel by using shadowgraph-like imaging technique. The result provides qualitative information on density gradients which may useful for void fraction prediction. The above mentioned works were done mainly to understand the cavitation regime, cavitation occurrence in a nozzle with simplified geometry, and the effect on the injected jet.

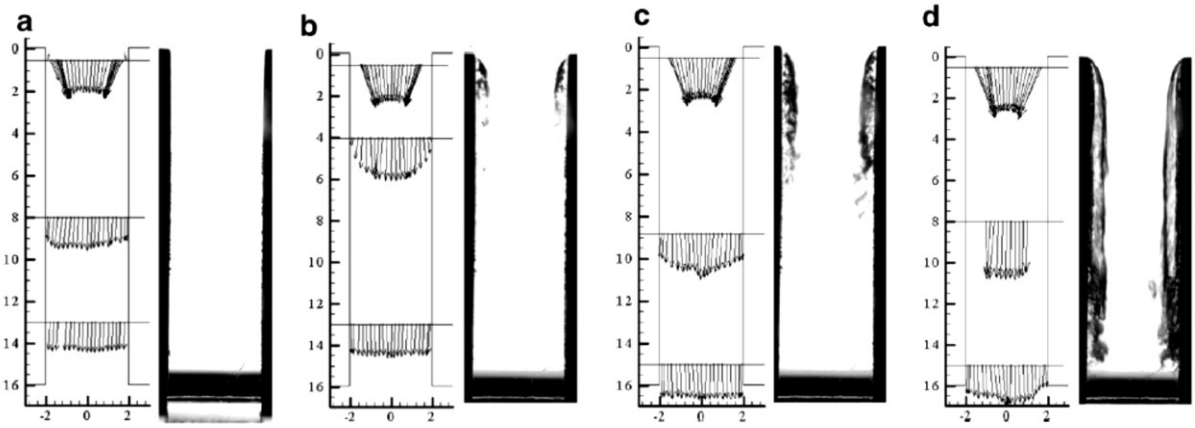

Figure 1.11 Distributions of mean liquid velocity in a 2D nozzle by LDV measurement (a) Re = 50,000, (b) Re = 58,000, (c) Re = 64,000, (d) Re = 70,000 (Sou et al.) [24]

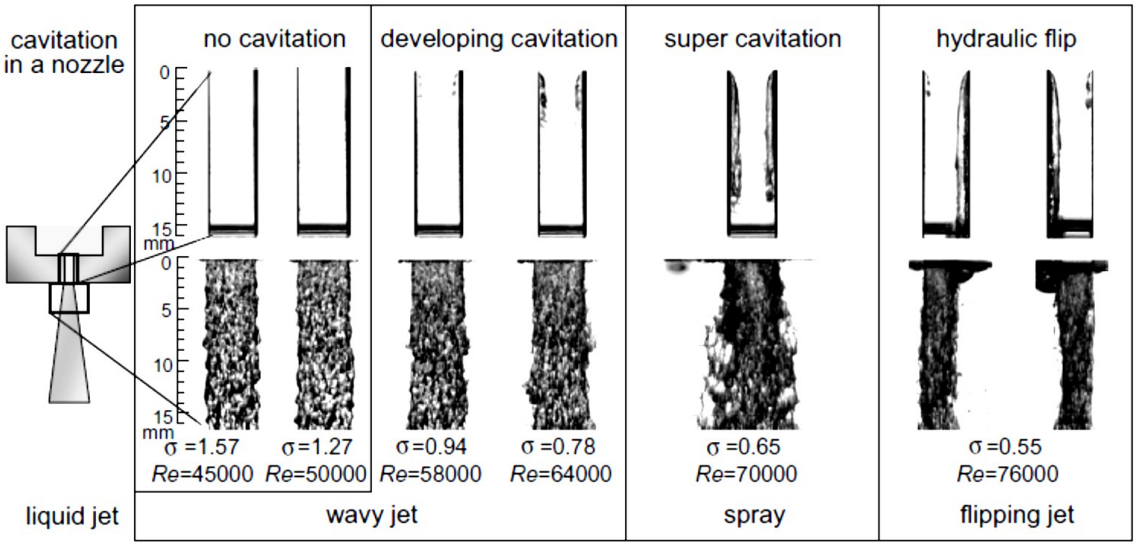

Figure 1.12 Cavitation in a 2D nozzle and liquid jet (Sou et al.) [24]

1.4.3 Cavitation in Real Size Nozzle

Following the finding using scaled-up nozzles, visualizations of cavitation in real size symmetric nozzles were carried out by a number of researchers. Badock et al. [34] investigated cavitation phenomenon in real size diesel injection nozzles utilizing Bosch Common Rail system by shadowgraph techniques. The experiment was conducted to understand the internal flow of cavitated nozzle and the spray breakup at the hole exit in pressurized chamber (up to 1.5 MPa). The captured images are too blurred to be useful for quantitative measurements of the cavitation film thickness.

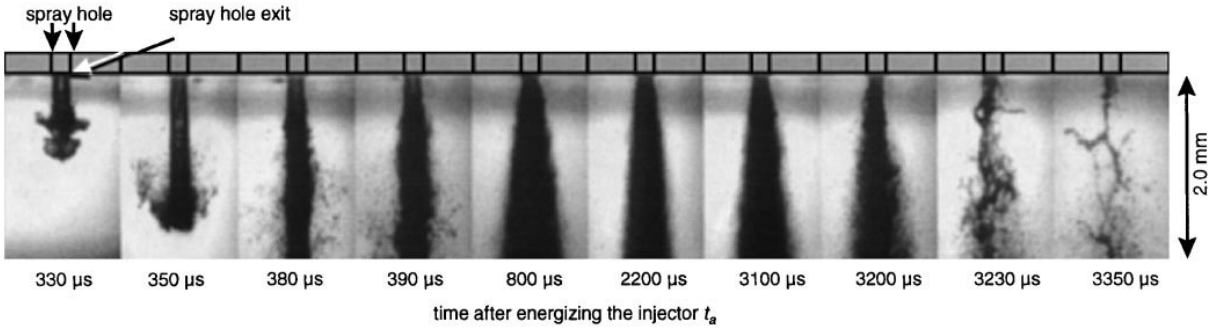

Figure 1.13 Visualization of free jet in the near nozzle region with the shadowgraph technique: rail pressure = 25 MPa, chamber pressure = 1.5 MPa, energizing time = 2 ms, spray hole diameter = 0.20 mm, length = 1.0 mm (Badock et al.) [34]

Experiment on cavitation in real size VCO nozzles was done by Miranda et al. [35]. They stated that the details of the cavitation process in real size nozzles are very difficult to be observed. In order to observe the cavitation in true VCO nozzle, they replaced the tip of a standard VCO nozzle by a glass prism which has a conical recess for the needle tip and two opposing holes of about 1 mm in length and 0.3 mm in diameter, as shown in Figure 1.14. Refractive index matching was done in this work by mixing diesel fuel with α-methylnaphthalene to match the refractive index of the glass prism. Different from other works, they submerge the injector tip into the mixture liquid to avoid distortion and other optical problem caused by the nozzle tip shape. They varied the chamber pressure as well as the injection pressure by changing the needle lift. Image of cavitation at various needle lifts and cavitation numbers were presented in this work.

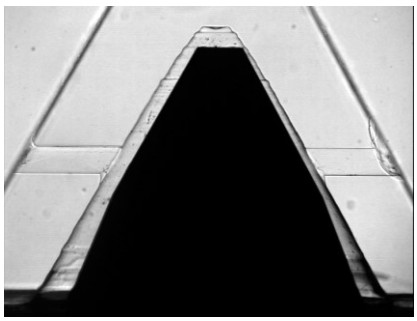

Figure 1.14 Side view of the real size transparent VCO nozzle (Miranda et al.) [35]

Collicott and Li [36] carried out an experiment by using true scale single-hole tilted nozzle with true injection pressure to understand and proof the scaling laws that there are too many unknown matters in the unsteady non equilibrium cavitating flows, such as homogeneous or inhomogeneous nucleation of cavitation, the onset of 3-D flow with small inlet cross-flow or hole tilt, cavitation bubble collapse and shedding at time scales often comparable to transit time through the orifice, boundary layer-roughness interactions, turbulent transport through an adverse pressure gradient to the exit plane, liquid column break-up outside the orifice, and droplet propagation and interaction within the measurement volume. The nozzle diameter used in the experiment is approximately 0.2-0.4 mm with pressures up to 210 MPa. As a result, images of cavitation in orifice are presented. Most of them show a motion blur due to the very high injection pressure and flow velocity. As a conclusion, they stated that identical result from a repeat attempts cannot be obtained due to surface roughness and the features near the inlet to the orifice, thus orifices production with greater similarity is required.

1.4.4 Cavitation in Real Geometry Nozzle

Mitroglou et al. [37] investigated the cavitation behavior in real scale mini-sac nozzle with transient flow by a high-speed visualization. They used 6-holes mini-sac type nozzle in the experiment and injected a liquid for 2 ms for single injection duration. From the results, they concluded every phenomenon for every events they captured in the transient flows, one of which the string cavitation occurrence in the nozzle and sac. Before this work, Mitroglou et al. [38] conducted an experiment by using scaled-up and real scale VCO nozzles with 6-holes and injected in transient mode. The work was also done to observe and investigate string cavitation occurrence as well as the spray cone angle for every needle lift.

Arcoumanis et al. [39]–[41]conducted an experimental works with scaled-up real VCO nozzle geometry with 6-holes. Laser Doppler Velocimetry (LDV) was conducted to obtain velocity data in cross sectional area of the sac. They used the experimental data to validate their existing CFD model. From the results, they concluded that variations in the flow pattern between holes do exist even in axisymmetric vertical multi-hole nozzles. Those variations are due to geometric effects such as needle eccentricity, and also the complex two-phase flow present in the sac volume and holes after the onset of cavitation.

Hayashi et al [42] have done a study whose purpose is to find the fundamental relationship between internal flow and spray formation of the nozzle as feedback for the nozzle design. They established flow visualization method in the real size nozzle and investigated the relationship between the transient nozzle internal flow, cavitation, and spray formation by using a mini-sac nozzle and valve covered orifice (VCO) nozzle in their study. They also examined the flow in the nozzle sac and hole by micro-PIV and computational fluid dynamics (CFD) analysis. In the experiment, an acrylic transparent nozzle, which has a similar refractive index of 1.49 to the diesel fuel of 1.46, was used. The geometry of the sac and the holes were made as similar as the original ones, as well as the inlet roundness of the holes. Shadowgraph technique was used and micro-PIV was conducted to measure the

velocity of internal flow in the nozzle. They introduced RANS scheme with standard k-ε model and used linearized Rayleigh model in their study to express the behaviors of cavitation bubble. The experiment results indicate that film type cavitation occurs frequently in the VCO nozzle. String cavitation affects spray formation more than the film cavitation, as the spray cone angle increases by the increases of the string cavitation thickness when needle lift is low. The experiment result shows the existence of one or two instant string cavitations which connect together. The streamline image, which is generated by the CFD in the study, clearly shows the existence of a spiral flow and low pressure region in the mini-sac nozzle hole under low needle lift condition. In VCO nozzle, flow separation is observed in the nozzle-hole inlet instead of vortex structure [42], [43]. From these works, string cavitation occurrence in a nozzle and its effects on the spray can be understand, however the mechanism of how the string cavitation occurs has not been clarified yet.

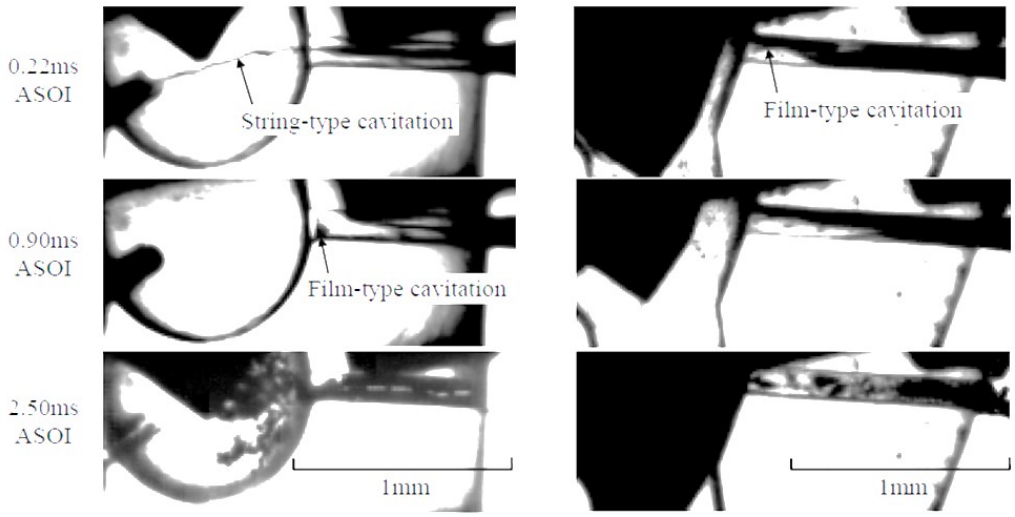

(a) 3-hole mini-sac nozzle (b) 3-hole VCO nozzle

Figure 1.15 Transient characteristics of cavitation in the mini-sac nozzle and VCO nozzle (Hayashi et al.) [42]

1.4.5 Cavitation in Complex Geometry Nozzle

As reported by other researchers [16], [17], [19], [34], atomization of fuel spray in a combustion chamber is initially caused by turbulence and cavitation in the jet rather than the influence of surrounding air. Furthermore, Soteriou et al. [44] mentioned in their work that cavitation is affected by running conditions, time, and injection system, which affects the discharge coefficient. As we may observe in large-scale nozzle models, total hydraulic flip occurs and the effect is obvious, while it also occurs in real size nozzles but is difficult to be observed. The actual hydraulic flip should be imperfect due to the difficulty in manufacturing process and this phenomenon cannot be clearly observed due to its tiny scale, and thus optical apparatus with a large scale, single hole, and transparent model is necessary to capture it. As a result of their works, they stated that the hollow cone spray is induced by a swirl flow motion into the nozzle when the needle valve and its seat are not concentric. The spray structure is

affected by the internal flow patterns and is not a result of interaction of the jet with surrounding air. The formation and cavitation development depend on the flow rate and the cavitation number, i.e. the relative pressure drop across the nozzle. The upstream flow of the nozzle-hole classified into several flow fields, in which multiple large vortices are formed. By CFD we can obtain useful trends of cavitation, however its accuracy is not enough. In addition to the results, they did an experiment on a nozzle with complicated geometry in order to increase the geometric complexity to produce multiple flow fields and thus one step closer to the actual nozzle geometry. The complicated geometry of nozzle upstream was found to produce some significant secondary flow fields as shown in Figure 1.16. As a consequence of these multiple flow fields, spiraling flow was observed inside the hole with one or two vortex structures.

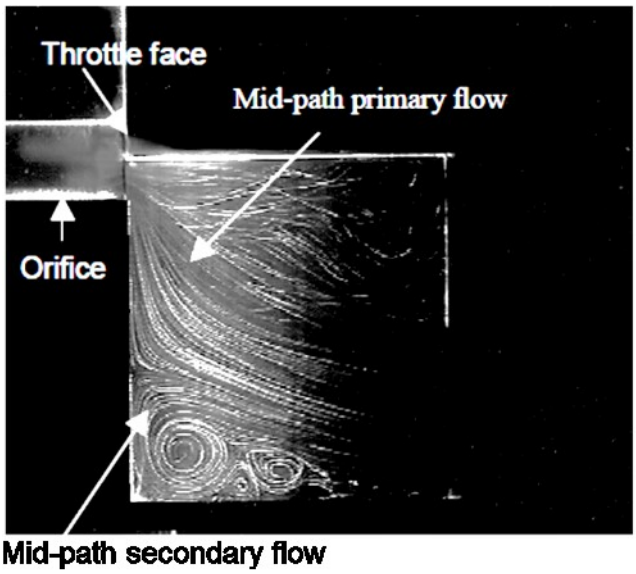

Figure 1.16 Multiple flow fields in the more complex geometry nozzle (Soteriou et al.) [44]

As reported by Andriotis et al. [45], they have conducted an experiment on flow in nozzle injector with complicated geometry to provide experimental data of string cavitation as well as to explain the formation, its area, lifetime, and its effects on the internal nozzle hole flow since there is no reliable model for predicting string cavitation in fuel injector. It is important to understand flow mechanisms in the diesel fuel injector for nozzle designing process. The experiment was conducted by using cylindrical and tapered five-hole nozzles, whose position in the sac and the distance between holes are not evenly distributed. Variation of the needle lifts was also taken into account in this experiment. The results showed that string cavitation forms at the core of recirculation zones. The string cavitation may occur from the sharp corners inside the nozzle or from the nozzle-hole exit. Figure 1.17 shows the typical image of string cavitation forms inside the nozzle volume at two different time instances, view from the bottom view and the side while Figure 1.18 shows image of tapered 5-hole nozzle with no string cavitation at high needle lift, string cavitation next to hole 4 at low needle lift, and air bubbles introduced into the sac volume at high needle lift.

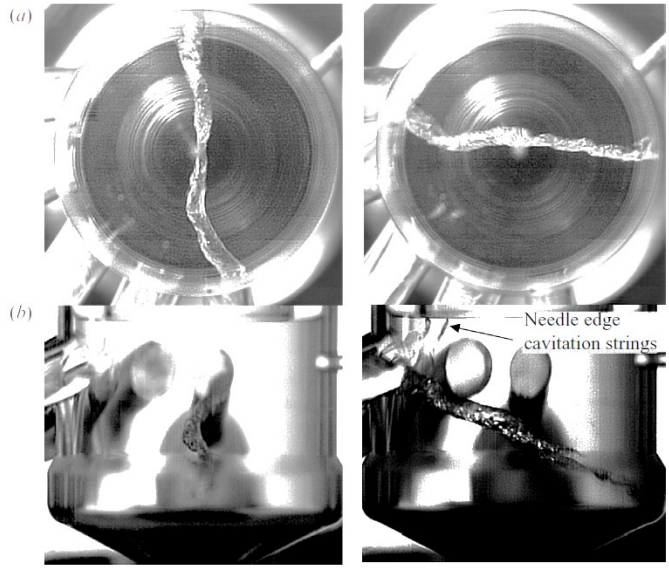

Figure 1.17 Typical image of string cavitation formed inside the nozzle volume at two different time instances (a) bottom view and (b) side view (Andriotis et al.) [45]

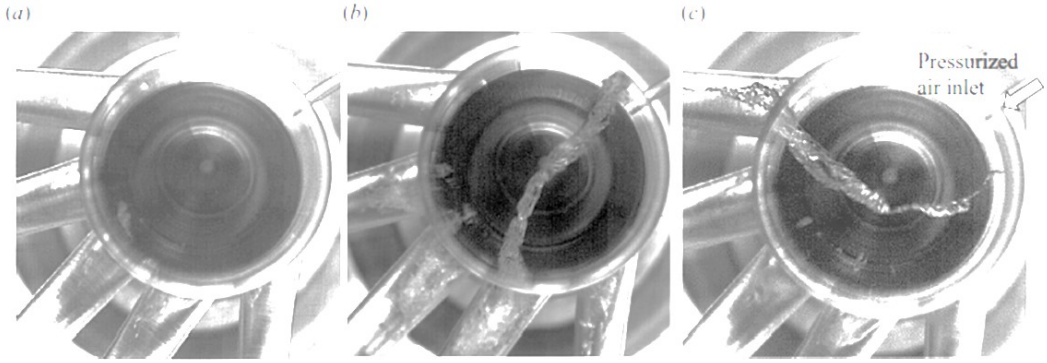

Figure 1.18 Image of tapered 5-hole nozzle with (a) no string cavitation at high needle lift, (b) string cavitation next to hole 4 at low needle lift and (c) air bubbles introduced into the sac volume at high needle lift (Andriotis et al.) [45]

A work done by Reid et al. [46] shows an optical comparison of the cavitation characteristics of diesel and bio-diesel blends in a true-scale nozzle optical diesel injector with high rail pressure. They used a nozzle with complicated geometry as can be seen in Figure 1.19. From the results they concluded that cavitation inception and its development for different fuels occurs at different cavitation number due to different fuel properties and thus a more comprehensive analysis of the fuel properties is necessary, especially the dissolved gas content. Special note also given that string cavitation occurs simultaneously with the film cavitation in the nozzles below the needle.

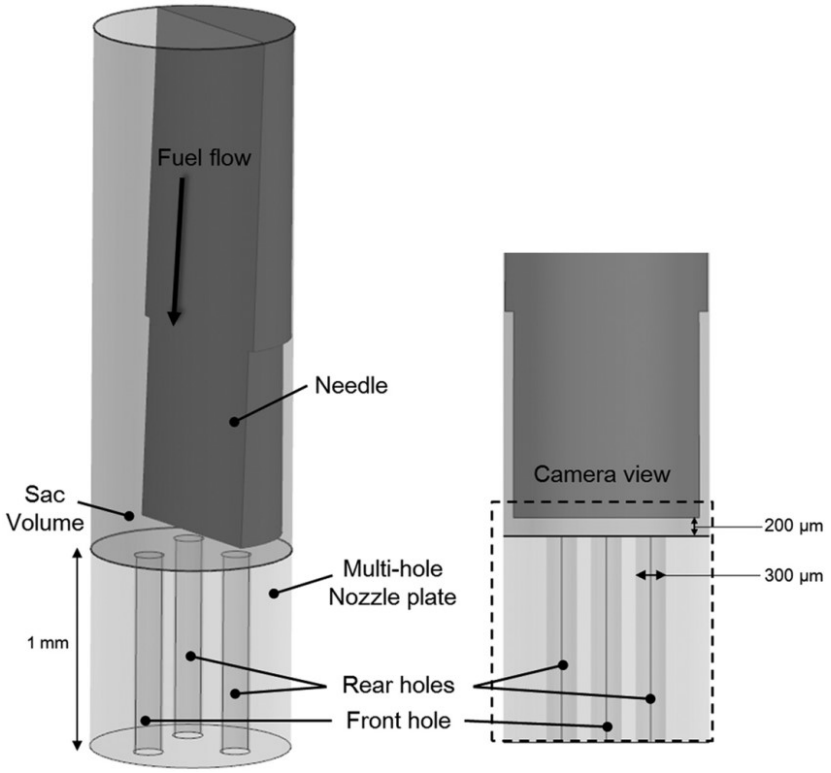

Figure 1.19 Optical nozzle with complicated geometry used by Reid et al. [46]

1.5 Numerical Simulation on Nozzle Internal Flow

In the visualization of cavitation in a nozzle of fuel injector, only the shape information of cavitation can be obtained. Flow field can be obtained experimentally, however, only at some specific points. Thus numerical simulation on cavitation in a nozzle of fuel injector is very important to get overall prediction of flow characteristics. Since cavitation is a complicated two-phase flow phenomenon, a lot of researchers paid their efforts to develop a model which can predict the nozzle internal flow correctly.

Martynov et al. [47] focus on the effects of cavitation disturbances on jet and spray break-up, thus as a first step they did a study on liquid quality and viscous shear stress effects on cavitation flow. For the model of hydrodynamic cavitation, they used a model which is based on the single-fluid homogeneous mixture cavitation model. As a result, they concluded that the shear-stress mechanism of cavitation shows a consistent result compared to the result of cavitation flow measurement in liquids with different viscosity, which was done by other researchers.

Argueyrolles et al. [48] concerned with choking phenomenon in the nozzle, which may affects engine performance and gas emissions. They conducted experiment and CFD simulation to understand the effect of nozzle geometry, such as hole conicity and hydro-grinding percentage, on the choking occurrence. The simulation was done to a 6-hole nozzle with two variations of hole conicity, and length to diameter ratio approximately equal to 6.5, by k-ε turbulence model. From the simulation results, they obtained the liquid volume fraction which is directly linked to the choking phenomenon. They concluded that numerical

calculations allow analyzing the interactions between operating conditions and various nozzle geometries, and thus the best design based on nozzle-hole geometry and choking phenomenon can be obtained.

Another CFD work done by Ishimoto [49] was focused on primary breakup phenomenon of injected liquid jet which is influenced by the micro-cavitation and is related to the consecutive formation of liquid film, and generation of droplets of a lateral flow in the outlet section of the nozzle. The simulation was taking into account the micro-cavitation generation based on the Barotropic Large Eddy Simulation-Volume of Fluid model in conjunction with the Continuum Surface Force model to clarify the detailed atomization process. From the simulation, aspects and volume fraction of micro-cavity, liquid core shapes, spray angle and spray velocity profile can be obtained, which are difficult to confirm by an experiment.

Watanabe et al. [50] explain the vortex flow change due to needle geometries in mini-sac nozzle, by visualizing and analyzing the internal flow by means of micro-PIV and CFD. They used commercial CFD code FIRE ver. 2008 (AVL) for the numerical simulation. The measured transient needle-lift and inlet pressure were taking into account for the computational model. The Reynolds-averaged Navier–Stokes simulation scheme with standard k–ε model was used to simulate the turbulent flow in the nozzle and spray chamber, while the cavitation bubble behavior is simulated by the linearized Rayleigh model. From the simulation result, a swirling flow was observed in the nozzle upstream which may results in string cavitation.

1.6 Visualization and Measurement Techniques

The flow visualization in fluid dynamics is conducted to see the flow patterns and to get qualitative or quantitative information of the flow. Since most fluids, such as water and air, are transparent, the flow pattern is invisible by the naked eye. Thus, flow visualization is the way to make the flow patterns visible. In the experiment of fluid dynamics, there are three methods of flow visualization, i.e. surface flow visualization, particle tracer methods, and optical methods [51]. Surface flow visualization is done by applying colored oil to the surface of a flowing liquid which results in a pattern of the colored oil flow. Particle tracer visualization is done by introducing particles, such as microspheres, into the fluid flow to trace the fluid motion. In turbulent flow, illumination of particles by a laser sheet can be applied in order to visualize a plane of a complicated fluid flow pattern. By this particle tracer visualization, velocity can also be obtained by particle image velocimetry (PIV) velocimetry method. Note that we assume that the particles accurately follow the flow streamlines. In the case of optical methods, there are some well-known optical methods such as shadowgraph, Schlieren photography, and interferometry. These methods utilize particular optical components and require special technique to do the visualization. In computational fluid dynamics (CFD), the results can show all the fluid properties in space and time. However, this information should be verified by the experimental flow visualization results since the CFD results cannot guarantee its accuracy due to the limitation of calculation model application.

Therefore flow visualization is as important as numerical simulation to reveal the flow phenomenon [52], [53]. In this section, four visualization techniques, which were used in the experiments discussed in this dissertation, will be briefly explained.

1.6.1 Backlight Imaging

In the research, it is a common consideration to cavitation and the injected liquid so the important phenomena of spray atomization process can be analyzed and discussed. Since the injection pressure is high, and thus the velocity, visualization has to be done by a very short exposure time or a very fast camera shutter-speed in order to obtain a still-image which looks like a static object without any motion blur. As the consequence of the very short exposure time or the very fast camera shutter-speed, the coming light intensity to camera will be very restricted. One solution to obtain a bright image by a low light intensity is by increasing the camera sensor sensitivity (ISO), however, this is not the best solution since it generates image noise which decreases the quality of the captured image. Another solution is by exposing the object between the camera and the light source in a straight line and therefore a bright image can be captured. It should be note that the captured object in the image will be shown as a dark object since it obstruct the incoming light to the camera sensor. Nevertheless, the dark area clearly shows its boundary with the bright background and thus clearly shows the shape of the object, which is very important to interpret the overall phenomenon.

A study to optimize optical system for backlight imaging was conducted by Ghandhi and Heim [54]. They proposed the optical system to increase the luminous efficiency by adding collimated light source, engineered diffuser, and field lens into the system, while the standard system only uses uncollimated light source and standard diffuser in the optical system, as shown in Figure 1.20. As a result, improvement of optical system was obtained by more than two times luminous efficiency than the standard optical system. In addition, the optimized system is cheap and does not significantly increase the system complexity.

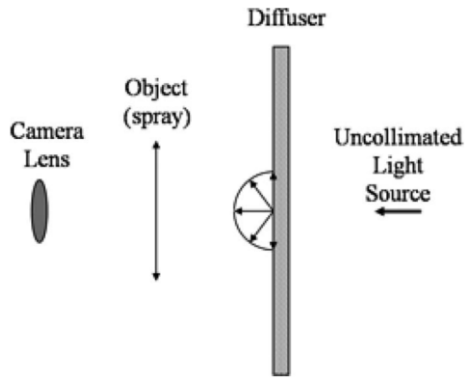

(a) Standard flood illumination system

Figure 1.20 Schematic configuration of standard flood illumination system and the proposed optimized lighting system by Ghandhi and Heim [54]

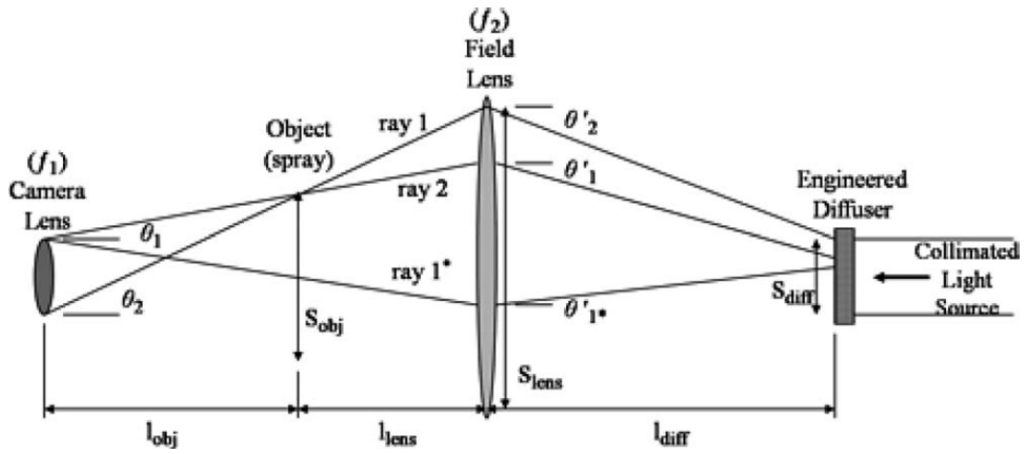

(b) Optimized lighting system

Figure 1.20 Schematic configuration of standard flood illumination system and the proposed optimized lighting system by Ghandhi and Heim [54]

1.6.2 High Speed Imaging

High-speed imaging is visualization method to capture a very fast-moving phenomenon. For an example, a detail motion of football player kicking a ball or a bullet motion when hitting an object can only be captured by a high-speed imaging. In many fields of study, the most important factors of high-speed imaging are spatial resolution and record-length. A work by Versluis [55] reviews high-speed imaging basics, especially for high-speed imaging experiments in fluids. This work also discusses ultra-high-speed imaging issue, stroboscopic imaging, triggering and illumination matters, scaling issue, and the combination of conventional experiments in fluid with high-speed imaging techniques, including leaping shampoo phenomenon, bubbles, snapping shrimp, droplet pinch-off, bubble pinch-off, shockwave, and root canal. The work is concluded with a high-speed imaging parameter chart, which takes length scale (spatial scale), camera speed in frame per second (temporal scale), and the velocity of moving objects as the main parameters of the chart, as shown in Figure 1.21.

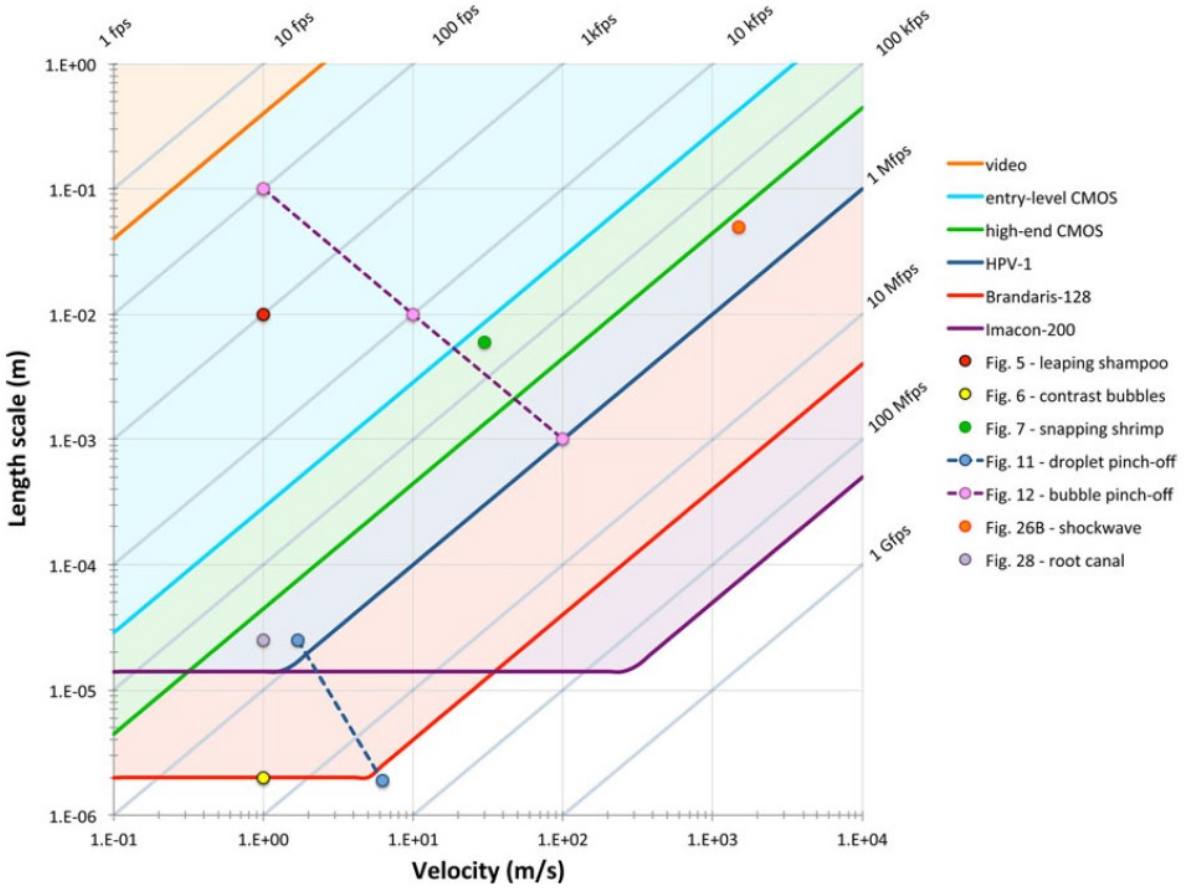

Figure 1.21 High-speed imaging parameter chart by Versluis [55]

A lot of works were done to visualize phenomena of fluid dynamics, such as a work done by Hrubes [56] that visualizing projectiles motion underwater, whose speed exceeds the speed of sound in water, to understand the launch and flight of underwater supercavitating projectiles. Another work was done by Klein-Douwel et al. [57] on the spray formation of diesel fuel injection by a real heavy-duty multi-hole common rail injector under high injection pressure of 150 MPa and high ambient pressure of 2.9 MPa using digital high-speed shadowgraph to capture a sequence of sharp spray images and to understand macroscopic spray geometry characteristics, i.e. spray length and cone angle. Another advance work by Sick et al. [58] summarizes high-speed diagnostics application on direct-injection spark-ignition (DISI) gasoline engines. Optical techniques are described with their application examples, such as particle image velocimetry to measure in-cylinder velocity, Mie scattering to follow the spray evolution, laser- induced fluorescence to record quantitative fuel distributions, refractive index matching to quantify fuel impingement on surfaces, combining velocity and fuel measurements to study ignition reliability, chemiluminescence techniques to understand the evolution of the spark plasma and the growing flame kernel, chemiluminescence and black body radiation imaging to understand the formation and oxidation of soot. In other words, these techniques can reveal the phenomena of intake flow, fuel injection, ignition, combustion, and soot formation. Crua et al. [59] utilize the high-speed microscopic imaging for experiment on the initial stage of diesel spray formation and primary

breakup. The experiment was conducted at atmospheric condition and pressurized ambient pressures up to 8 MPa, and injection pressures up to 160 MPa. A spatial resolution of 0.6 μm per pixel, and a captured region of 768×614 μm were set for the experiment. It allows the observation of shearing instabilities and stagnation point on the tip of diesel jets. As a result, an oblate spheroidal cap was observed as shown in Figure 1.22, which confirms that vaporized fuel remains trapped in the injector holes after the end of the injection process. It also confirms the degradation of residual fuel due to the deposits formation in the diesel injector nozzle-holes. A work by Eagle et al. [60] investigates transient diesel spray behavior during high pressure injection of a multi-hole fuel injector by high speed imaging. The fuel injector nozzle has four holes with diameters of 90, 110, 130, and 150 μm. The fuel was injected with pressures of 1000, 1500, and 2000 bar, into a chamber with room temperature of 298 K, nitrogen environment at densities of 17.5, 24.2, and 32.7 kg/m^3, and captured with backlight high-speed imaging at 100,000 frames per second. As a result, fuel spray-tip tracking algorithm was developed and it can quantify the angular location of the maximum penetration distance.

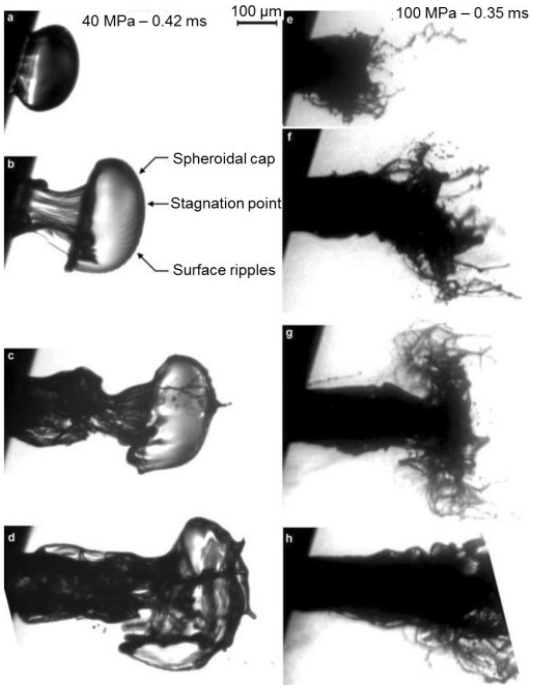

Figure 1.22 High speed images showing effect of injection pressure on the initial stage of fuel injection at atmospheric conditions (Crua et al.) [59]

Application of high-speed imaging technique to visualize cavitation in a nozzle of fuel injector is rarely found due to the difficulty of visualizing a very high speed object (cavitation) in a very small space (nozzle). Since the high-speed camera resolution is very low for very high camera speed (frame per second), the quality of the captured images is very low. In some previous studies, scaled-up transparent nozzle was intentionally used, one of which to decrease the difficulty of visualization due to the spatial matter and thus increase the quality of the captured images. Figure 1.23 shows an example of a high-speed image sequence of

cavitation cloud shedding in a large scale symmetric cylindrical nozzle, captured by Stanley et al. [21]. The cavitation cloud shedding occurs within 0.4 ms. The high-speed images were captured by Phantom V7.3. The sampling speed of camera is 20,052 fps in frame rate, so that the time between images is about 0.1 ms. The camera was set in order to capture the nozzle inlet region with 8.25 mm in nozzle diameter.

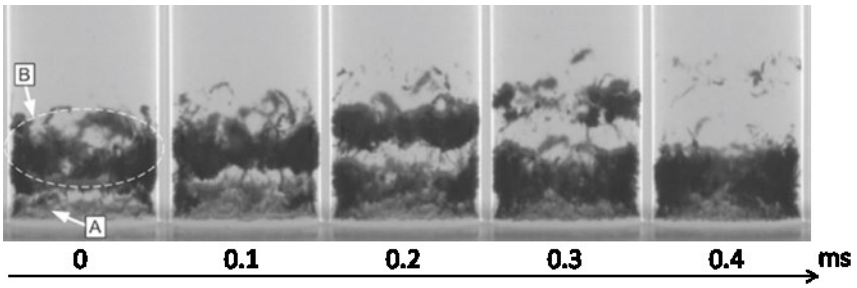

Figure 1.23 High-speed images of cavitation cloud shedding in nozzle (Stanley et al.) [21]

1.6.3 Particle Image Velocimetry (PIV)

Particle image velocimetry (PIV) is one of the methods to measure a flow pattern of any fluids. This method usually used in many fields to obtain instantaneous velocity in fluids. As stated by Prasad in his review article on Particle Image Velocimetry, the PIV represents a quantitative extension of a qualitative flow-visualization technique which has been practiced for several decades. By introducing tracer particles into a fluid, it is assumed that the tracer particles will follow the flow dynamics and thus will represent the overall flow pattern of the fluid. The area of interest, where the analysis is conducted, should be illuminated so that particle motion is visible. The particle motion is analyzed, usually by cross correlation method, to get the velocity vector and magnitude. Typical PIV apparatus consists of a digital camera (usually a high-speed camera), a light source such as stroboscope lamp, metal halide lamp, or laser, seeding particles, and PIV software for analysis and post-processing. In the case of laser illumination, it is usually done to get a two-dimensional image by utilizing a cylindrical lens to convert a laser beam to a laser sheet. Figure 1.24 shows the common basic requirements for a PIV system. [61]

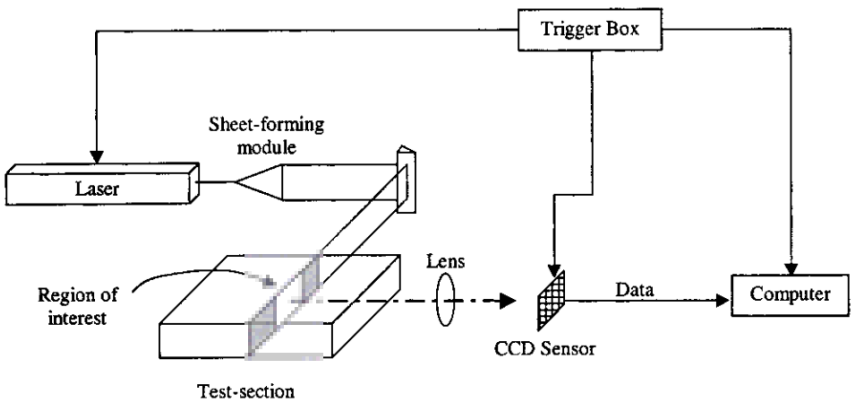

Figure 1.24 Basic schematic of a PIV system (Prasad) [61]

The PIV technique has been used and improved at the same time that the development of this technique was reported several times in several years. [61]–[68] The development is progressive because of the other development of PIV components, such as high-speed camera, CCD sensor, optical lens, laser, tracer particles, etc. Presently, the standard system sold by commercial companies consists of a single-camera, planar light sheet with a double-pulsed Nd:Yag laser, cross-correlation PIV method, and a 2,000 × 2,000 pixels cross-correlation PIV camera. In turbulence research, a simple 2D PIV is considered as a very important component for revealing fundamental aspects of turbulence structure. [66] As reported in detail by Jahanmiri [67], PIV technique has reached many applications in many areas of research, among others: boundary layer flows, supersonic flows, transonic flows, surface-ship flow, propulsion hydrodynamics, underwater ship flows, and two-phase bubble flows.

1.6.4 Stereoscopic PIV

Stereoscopic particle image velocimetry (PIV) is a method of field velocity measurement by applying two cameras. The cameras are used to record a simultaneous area of interest, where the analysis is conducted, from different angle. Stereoscopic PIV provides the third velocity component, i.e. the z-axis velocity component by the correction of the in-plane velocity measurement due to the perspective effects [68]. Figure 1.25 shows commonly used stereoscopic systems, i.e. translation system, also known as lateral displacement, and rotational system, also known as angular displacement. The main difference between these two systems is the position of the camera and the lens, that the lateral system places the camera and lens parallel to the object plane, while the rotational system places the camera and lens rotationally so that the lens plane and the image plane intersect at the object plane [65].

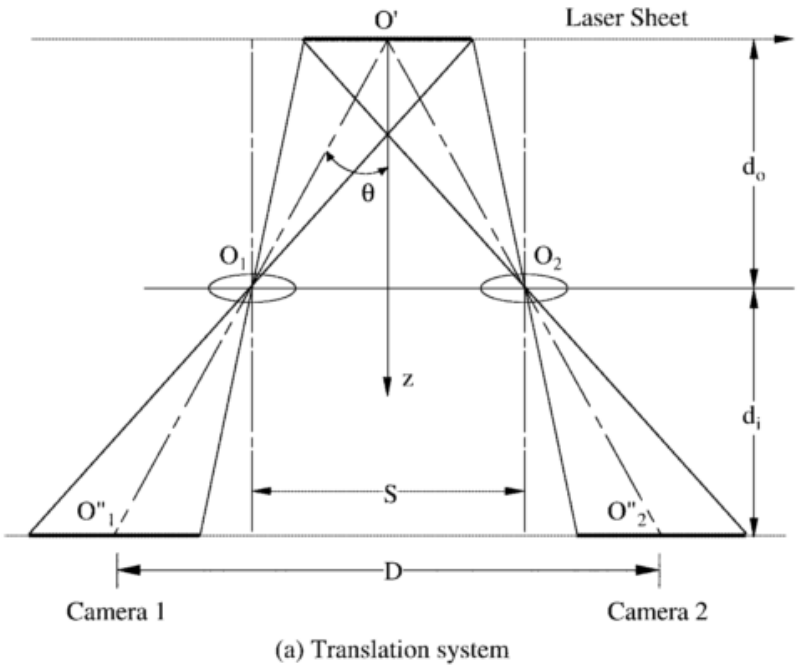

Figure 1.25 Two basic configuration for stereoscopic PIV systems (Prasad) [65]

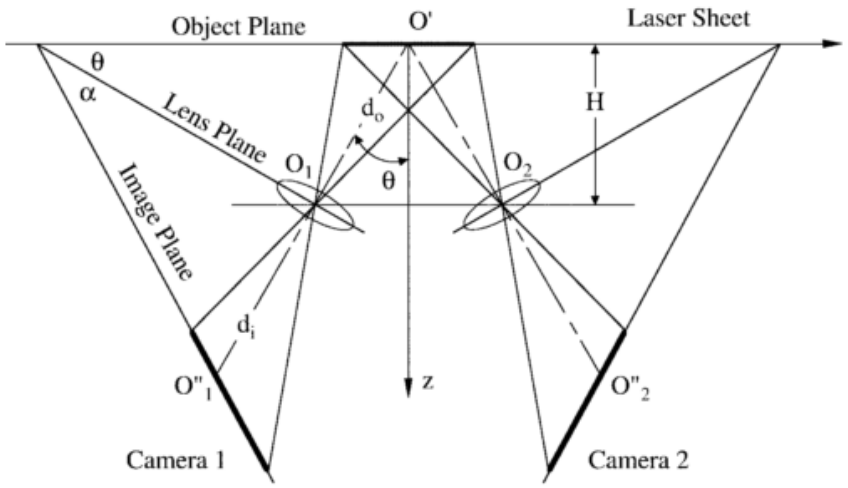

(b) Angular displacement system

Figure 1.25 Two basic configuration for stereoscopic PIV systems (Prasad) [65]

The extension of stereoscopic PIV has reached some fundamental points, such as, hybrid stereoscopic PIV which combines the advantages of the rotational system and translation system. The evaluation of this method was done by an experiment using nozzle with 25 mm of diameter and with 33 m/s of the injected jet. The result shows a successful optimization of the hybrid method, as shown in Figure 1.26. [69] Another extension of stereoscopic PIV is a multi-plane stereoscopic PIV as introduced by Liberzon et al., whose technique main principle lies in the combination of defocus, stereoscopic, and multi-plane illumination concepts. The basic cross-correlation PIV algorithm was used to analyze three pairs of separated images. The results show an ability to achieve a three-dimensional measurement which provides new insight into turbulence research. [70] Another work to extend stereoscopic PIV was done by Lindken et al. by stereoscopic micro PIV (μPIV). The work was done by measurement of the flow in the mixing region of a microfluidic T-mixer at Re = 120 (laminar flow). The error in the measurement is below 7.0%. The accuracy cannot be reached as in stereoscopic PIV at macro scale since stereoscopic μPIV accuracy is limited by the moderate angle between the viewing directions and the large depth-of-correlation compared to gradients expected in microscopic flows. [71]

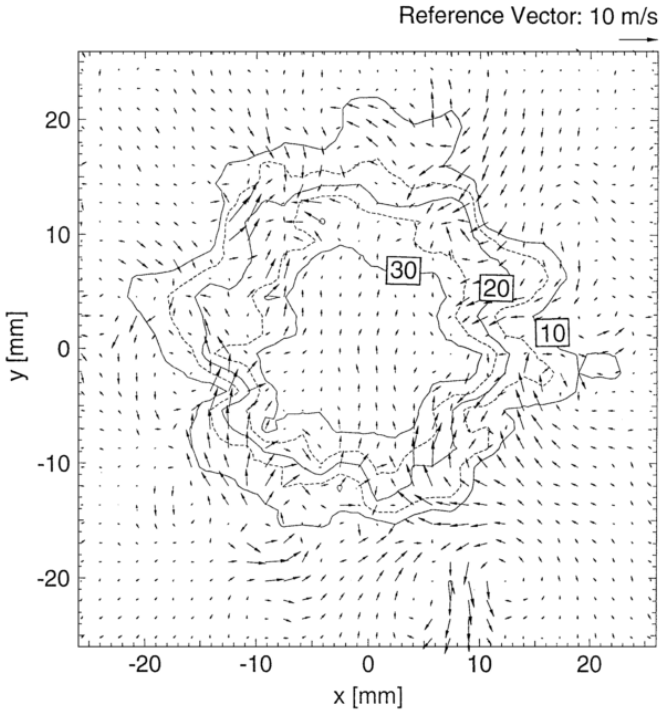

Figure 1.26 Three-dimensional representation of the instantaneous velocity field of a 33 m/s jet flow by hybrid stereoscopic PIV (Gaydon et al.) [69]

1.7 Objectives

According to the background and the previous studies in this research field, there are unsolved problems and gaps between studies which make the mechanism of nozzle internal flow effect on primary breakup of liquid jet remains unclear. Thus this study is presented to fill the gap between studies of cavitation in a nozzle with simple symmetric upstream geometry and that with real complex geometry. In this study, as the first step we focus on an asymmetric inflow to the nozzle, and then treat a complex upstream inflow. To quantitatively measure, evaluate, and predict cavitation, two-dimensional (2D) nozzles are used as the first step, and then use three-dimensional (3D) nozzles to examine 3D effects including string cavitation. By utilizing two-dimensional nozzle, we are able to measure the cavitation profile and make quantitative analysis. This quantitative data can be used to evaluate some dimensionless numbers which are useful for the cavitation prediction for nozzles with various geometries. The work then should be expanded to understand string cavitation in cylindrical nozzle. Since the previous studies of string cavitation could not clearly explain its mechanism, in this study string cavitation is investigated using nozzles with an asymmetric inflow in simplified geometry with various needle lifts. These works, however, do not include the effects of complex geometry of mini-sac nozzle, which is commonly used in the diesel engine. Thus this study covers the unknown effects of mini-sac nozzle geometry factors by examining each of important geometry factors of mini-sac nozzle, i.e. needle angle, needle lift, nozzle angle, length between needle seat and nozzle inlet edge, sac depth, and sac radius. This work should be carried out in two-dimensional nozzle in order to measure the cavitation and

internal flow characteristics, and then an advance work should be conducted by using nozzle with real geometry. By completing these investigations, the results would definitely contribute to the next step of research on cavitation in the nozzle of future injector.

The general objective of this research is to reveal several unknown phenomenon of cavitation in the nozzle of fuel injector. The detailed objectives are summarized consecutively as follow:

1. To quantitatively evaluate cavitation in 2D nozzles with an asymmetric inflow and the liquid jet, and propose a strategy to predict cavitation and the jet.
2. To understand string cavitation formation in nozzles with simple geometry.
3. To reveal the effects of each mini-sac nozzle geometry factors on cavitation and the injected liquid jet by analyzing internal flow in nozzle-hole and the upstream (sac), and its effects to cavitation.
4. To understand string cavitation in real 3D geometry of mini-sac nozzle, its effects on the injected liquid jet, as well as the effects of needle lift on them.

1.8 Dissertation Structure

The dissertation is written in six chapters and the explanation of each chapter is written below:

1. Chapter 1 explains the background and motivation of this research, which lead all researchers in this field to pay their efforts to reveal an unknown phenomenon of cavitation, particularly in the nozzle of a fuel injector. Following the background, basic explanations and previous studies of what cavitation is, as well as diesel fuel injector are written to let the readers understand the physical phenomenon of cavitation and why it occurs in the diesel fuel injectors as well as its importance on diesel engine performance. In this chapter, it also consists of literature reviews of previous studies on cavitation in the diesel fuel injector, that a lot of information on previous works done by other researchers are written in order to explain about what have been done and what have not, thus the readers can expect what should be done in this dissertation as the contribution in the research of cavitation in a nozzle of a fuel injector. From these explanations, I mention the research objectives which should be done in my doctoral program, as well as this dissertation structure to close this chapter.
2. Chapter 2 contains work on cavitation in two-dimensional (2D) asymmetric nozzle-hole. This chapter mainly discusses the effect of asymmetric inflow on cavitation in a nozzle and the resulting jet which represents the valve-covered orifice (VCO) nozzle. The work has been done by varying the needle lift and nozzle-hole length, and also comparing the results with symmetric nozzle result.
3. Chapter 3 explains about the cavitation in a cylindrical single-hole nozzle. The geometry of the nozzle itself is a simplified one which represents the VCO nozzle. Main parameters which are varied in this study are needle lift and upstream-volume width. These two parameters determine the nozzle upstream geometry which plays a very important role in

string cavitation formation. Therefore, the effects of nozzle upstream geometry on cavitation formation and the jets are investigated and mainly discussed in this chapter.

4. Chapter 4 discusses cavitation in two-dimensional (2D) mini-sac nozzle. Since mini-sac nozzle has more complicated geometry than VCO nozzle, the effects of every geometry parameters are investigated. In this study, the effects of needle and nozzle geometries, i.e. needle lift, needle angle, and nozzle angle were investigated. Particle image velocimetry (PIV) analysis was also conducted in this study to show the flow behavior and characteristic in nozzle sac and nozzle hole. This chapter also contains the investigation on the effect of sac geometries, i.e. length between the needle-seat corner and nozzle-hole edge, sac radius, and sac height are discussed to understand their effects on cavitation and the injected liquid. Particle image velocimetry (PIV) analysis was also conducted in this study to show the flow behavior and characteristic in nozzle sac and nozzle hole.
5. Chapter 5 tells us about the cavitation in the real geometry of mini-sac nozzle and the injected jet. There are several works have been done by other researchers to investigate cavitation and the spray in the real-size optical mini-sac nozzle. However, since the limitation of optical access and image quality due to the tiny size of the nozzle, the cavitation and nozzle internal flow behavior in mini-sac nozzle are remained unknown. In this chapter, we can see a work done by using scale-up (large size) mini-sac nozzle whose results shows us a clear image of cavitation in the mini-sac nozzle as well as the liquid jet.
6. Chapter 6 concludes the overall achievements obtained in this research. This chapter also remarks all of the important discussions which appear from the first chapter of the dissertation.

Chapter 2
Cavitation in Two-Dimensional Nozzle with Asymmetric Inflow

2.1 Introduction

In this chapter, the effects of asymmetric inflow on cavitation and liquid jet are discussed. The work is mainly focused on asymmetric inflow at the inlet since it appears just above the cavitating nozzle and is known to have a great impact on the cavitation and the resulting jet. Hence, visualization of cavitation in various 2D single-hole nozzles with an asymmetric inflow was conducted. Nozzles with different lengths are also tested to understand the nozzle length effect on cavitation and the jets. Since asymmetric inflow at the inlet is strongly influenced by needle lift, visualizations of cavitation in nozzles with various needle lifts were conducted. Cavitation in asymmetric nozzles and their liquid jets are captured using a high-speed camera. In this chapter, utilization of modified cavitation number which is based on local pressure at vena contracta is introduced since it can quantitatively predict the cavitation development for various symmetric nozzles. Finally, comparison of the structure of cavitation in asymmetric nozzles with that of symmetric nozzles was done to get a new understanding of cavitation in multi-hole injectors.

2.2 Experimental Setup

Figure 2.1 shows the schematic picture of the experimental apparatus used in this study. Filtered tap water at room temperature in a tank was injected at constant flow rates through a valve, a flowmeter, and a transparent nozzle into atmospheric ambient air. Mean liquid velocity V in the nozzle was varied to observe cavitation inception, super cavitation, and hydraulic flip. Cavitation and jet images were taken using a high-speed camera (Photron, FASTCAM SA5, 752×320 pixels, and 4μs in shutter speed) with a backlighting assist of a metal-halide lamp (Kyowa Co. Ltd., MID-25FC). A flow meter was used to measure the liquid flow rate flowing through the nozzle.

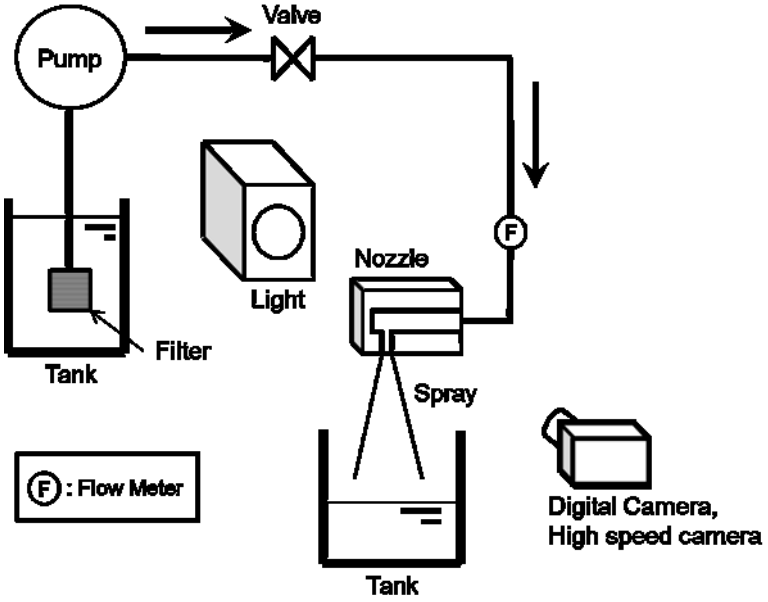

Figure 2.1 Experimental apparatus of nozzle with Asymmetric Inflow

Figure 2.2 shows the drawings of the nozzles. Two-dimensional nozzles of thickness T = 1.0 mm were used to clearly visualize the cavitation in the nozzles and to quantitatively measure cavitation length and thickness. Two symmetric nozzles with upstream width W_U = 32 mm and with different nozzle lengths L were used, short nozzle of L/W = 1.5 and long nozzle of L/W = 4, where W is the nozzle width and is 4.0 mm. Four asymmetric nozzles of L/W = 1.5 and 4 with different needle lifts Z were tested, i.e. Z/W = 1 as the low needle lift and Z/W = 4 as the high needle lift. The distance from nozzle left wall to upstream left-end wall W_{UL} is 16 mm. Dimensions of the nozzles are summarized in Table 2.1. A symmetric nozzle was used to compare the result with the asymmetric nozzle so that the effect of lateral inflow could be examined clearly. The applicability of the modified cavitation number to the prediction of cavitation in various VCO nozzles is examined.

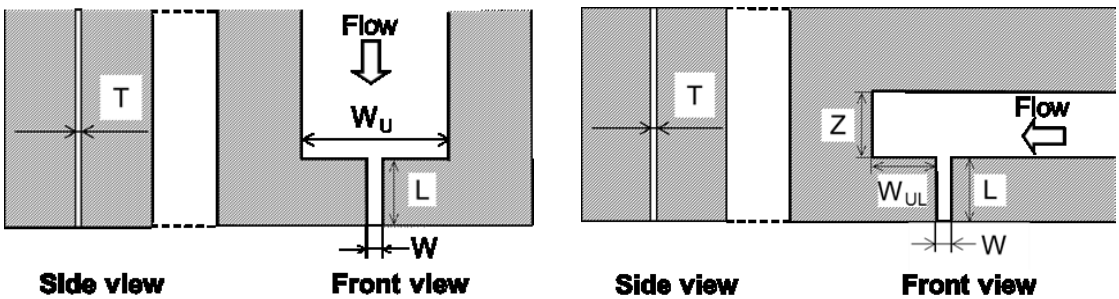

(a) Symmetric nozzles (b) Asymmetric nozzles

Figure 2.2 Symmetric and Asymmetric nozzles

Table 2.1 Dimensions of the test nozzles (2D VCO nozzles)

Nozzle	L [mm]	W [mm]	Z [mm]	L/W	Z/W
symmetric	6.0	3.9	-	≈ 1.5	-
asymmetric	6.0	4.3	4.0	≈ 1.5	≈ 1
asymmetric	6.0	4.3	16.0	≈ 1.5	≈ 4
symmetric	16.0	3.9	-	≈ 4	-
asymmetric	16.0	4.1	4.0	≈ 4	≈ 1
asymmetric	16.0	4.1	16.0	≈ 4	≈ 4

2.3 Results and Discussion

2.3.1 Cavitation and Jet (L/W = 1.5)

Images of cavitation for L/W = 1.5 and those of cavitation and liquid jets for L/W = 1.5 with various mean liquid velocities are shown in Figure 2.3 and Figure 2.4, respectively. Figure 2.3 (a) and Figure 2.4 (a) show the results of the symmetric nozzle, (b) the asymmetric nozzle for Z/W = 4, and (c) the asymmetric nozzle for Z/W = 1. Cavitation, which is indicated as the dark area between the left and right walls due to the refraction of the light that the gas-liquid interface is not parallel to the nozzle front wall in backlighting visualization, occurs due to the pressure drop in the recirculation flow area. A smooth interface of a gas film appears as transparent, which clearly indicates the large film formation instead of bubble cloud formation. In all of the short nozzles, developing cavitation and super cavitation are not observed and hydraulic flip occurs at very low V, which is different from that in the long nozzles shown later in this chapter.

As shown in Figure 2.3 (a) and Figure 2.4 (a), cavitation does not take place in the symmetric nozzle at very low V ($V \leq 5.1$ m/s), where the liquid jet deforms due to the vortex shed near the nozzle exit. An increase in V results in a partial hydraulic flip (PHF), and hydraulic flip occurs at either the right or left wall [72]. Since the hydraulic flip layer is slanted at the exit of the nozzle due to the short nozzle length, the jet is also tilted. Further increase in V ($V \geq 25.3$ m/s) leads to total hydraulic flip (THF), where hydraulic flip takes place at both right and left walls [72] and results in straight downward main flow and injected jet with little atomization.

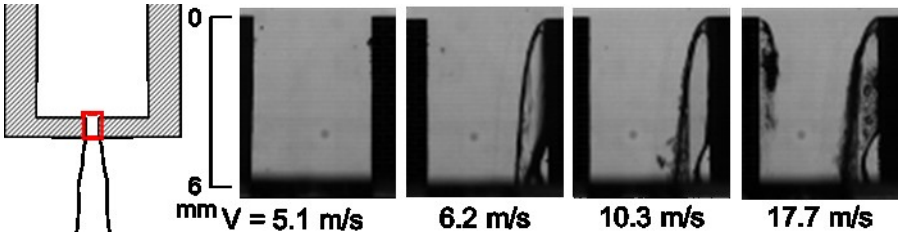

(a) Symmetric nozzle

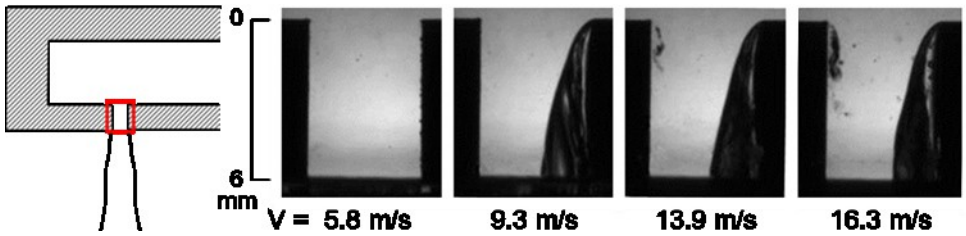

(b) Asymmetric nozzle (Z/W = 4)

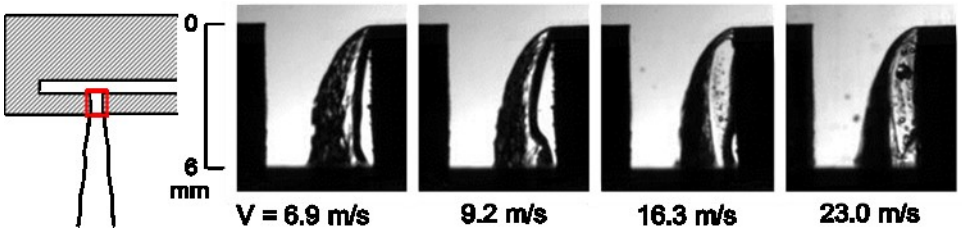

(c) Asymmetric nozzle (Z/W = 1)

Figure 2.3 Images of cavitation in the short nozzles (L/W = 1.5)

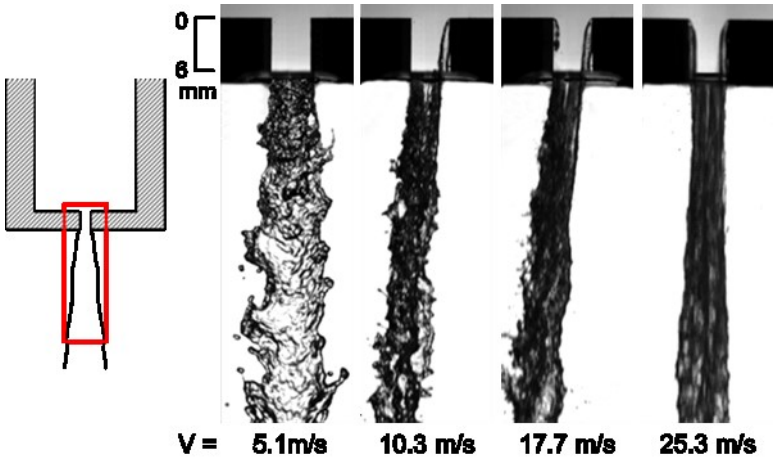

(a) Symmetric nozzle

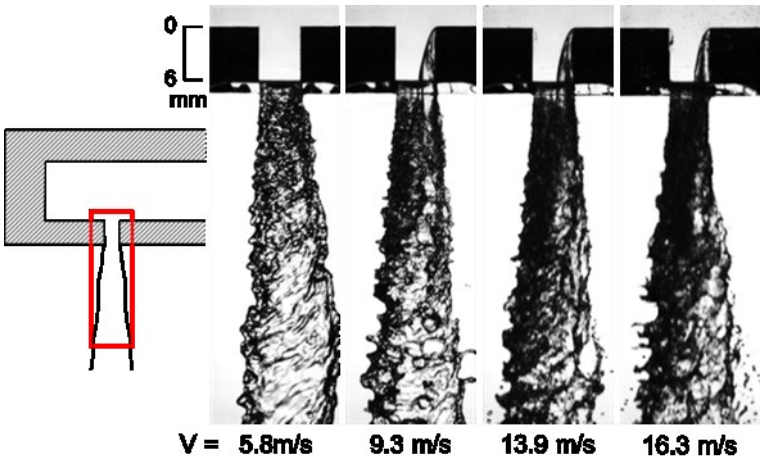

(b) Asymmetric nozzle (Z/W = 4)

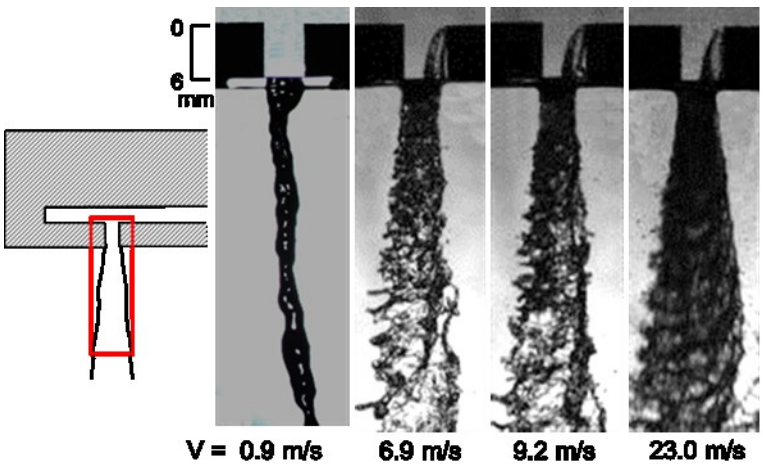

(c) Asymmetric nozzle (Z/W = 1)

Figure 2.4 Images of cavitation in the short nozzles and jets (L/W = 1.5)

As shown in Figure 2.3 (b), (c) and Figure 2.4 (b,) (c), PHF and smooth jets are not formed even at high mean velocity V (V = 16.3 m/s at Z/W = 4 and V = 23.0 m/s at Z/W = 1).

At non-cavitation, the jets are slanted slightly toward the upstream (right) side due to the separated boundary layer formed along the right side of the nozzle. A slight increase in V forms imperfect hydraulic flip (IHF) [72], where the injection angle is larger than those at PHF in the symmetric nozzle.

Figure 2.5 illustrates the definitions of cavitation length L_C, left side of jet angle θ_L and right side of jet angle θ_R. In this study, the following results show the mean values obtained using ten images. It should be noted that θ_L and θ_R at PHF in the symmetric nozzle are based only on images where PHF occurs at the right side of the nozzle. Figure 2.6 shows measured cavitation length L_C normalized by the nozzle length L. Figure 2.7 (a), (b) and (c) show θ_L, θ_R and total jet angle (θ_L + θ_R), respectively. These figures show different results for the cavitation length and jet angle in the symmetric nozzle, the asymmetric nozzle with Z/W = 1 and the asymmetric nozzle with Z/W = 4.

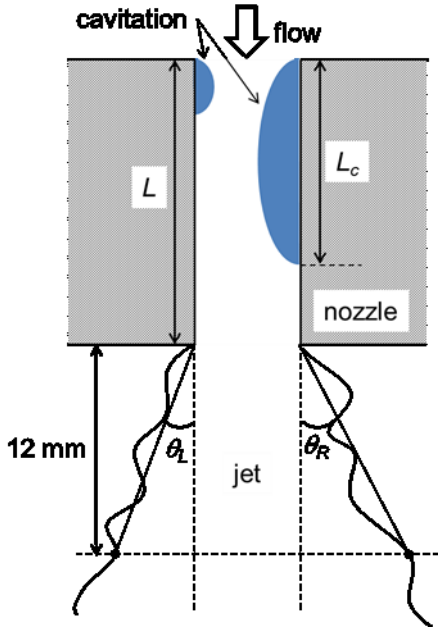

Figure 2.5 Definitions of L_C, θ_R, and θ_L

Figure 2.6 clearly shows that in the short nozzle of L/W = 1.5 hydraulic flip is formed at V = 9.3 m/s in the asymmetric nozzle with large needle lift (Z/W = 4), while it occurs at a much smaller V of 1.2 m/s with a smaller lift (Z/W = 1). The transition to IHF at the very small V for Z/W = 1 is caused by a thicker flow separation at the inlet corner (Figure 2.3 (c)) induced by the large lateral velocity in the upstream of the nozzle. The reason for THF formation at higher V (V ≥ 25.3 m/s) in the symmetric nozzle is that flow separations at both right and left corners are thick, which reduces the core flow area.

As shown in Figure 2.7, θ_R suddenly decreases at IHF, while θ_L is increased with V in the asymmetric nozzles. As a result, the asymmetric nozzle offers us a wide range of velocity condition in which the injection angle is stable yet increases with V. When the needle lift is small (Z/W = 1), the asymmetric inflow plays an important role especially in the increase of the injection angle, this is of import for future use in atomizers. In the symmetric short nozzle,

hydraulic flip does not occur at low velocity of V < 6.2 m/s. In such case, flow separation occurs at the nozzle inlet and vortices are shed from the reattachment point close to the exit due to the short nozzle length, which induces jet deformation and large jet angle even without cavitation.

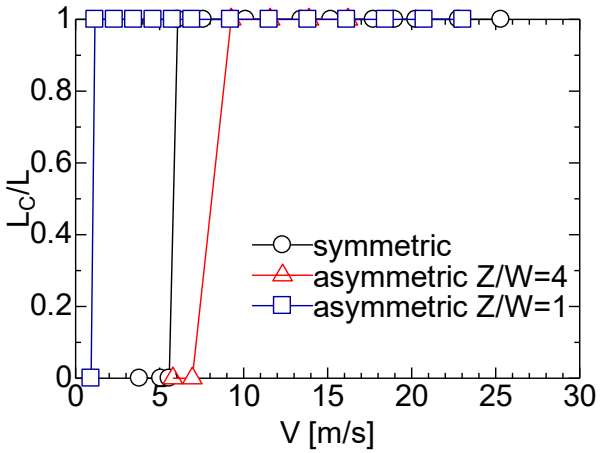

Figure 2.6 Cavitation length vs. mean flow velocity (L/W = 1.5)

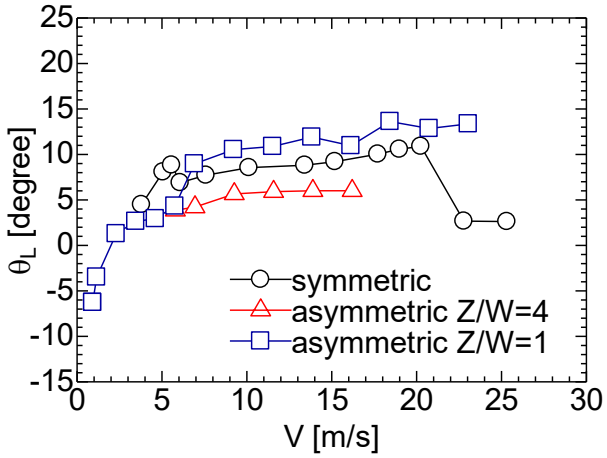

(a) Left jet angle

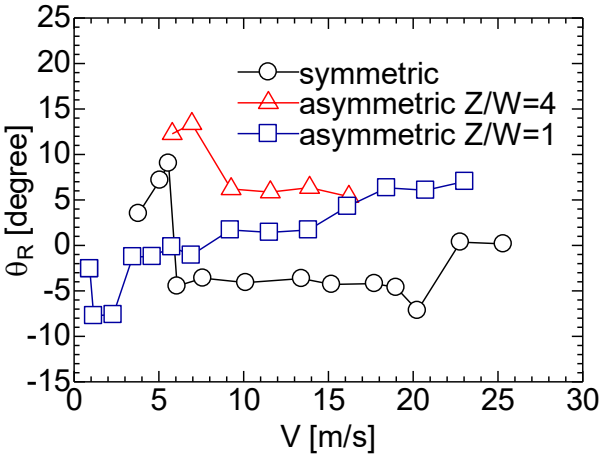

(b) Right jet angle

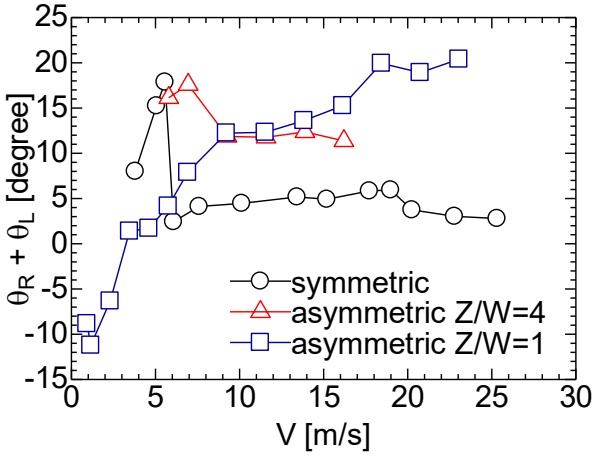

(c) Total jet angle

Figure 2.7 Jet angle vs. mean flow velocity (L/W = 1.5)

2.3.2 Cavitation and Jet (L/W = 4)

Figure 2.8 (a), (b), and (c) show the images of cavitation for the symmetric nozzle of L/W = 4, the asymmetric nozzle of Z/W = 4, and that of Z/W = 1, respectively. Figure 2.9 shows the images of cavitation together with liquid jets. As shown in Figure 2.8 (a) and Figure 2.9 (a), cavitation in the symmetric nozzle reproduces the regime transition reported in previous reports [17], [26], that is, cavitation inception, developing cavitation, super cavitation and hydraulic flip, and in super cavitation the jet atomized drastically. As shown in Figure 2.8 (b), (c) and Figure 2.9 (b), (c), an asymmetric inflow clearly induces asymmetric cavitation in the nozzle, which results in asymmetric jet behavior, i.e., the right side of the jet moves downward at a lower velocity than the left side, and the jet deforms at the right surface. In the asymmetric long nozzles of L/W = 4, IHF occurs at high V and atomization of the jet is suppressed.

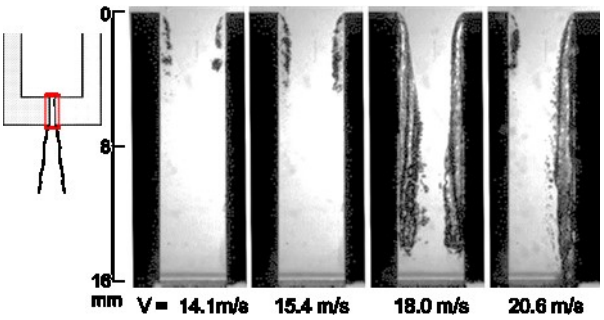

(a) Symmetric nozzle

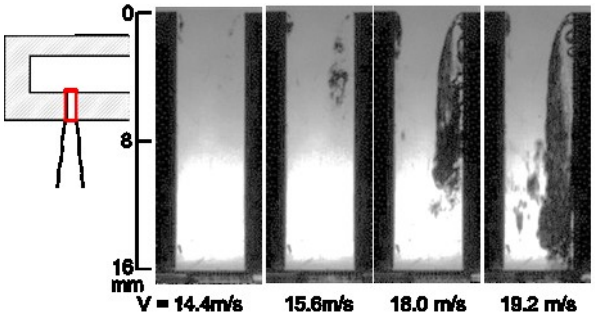

(b) Asymmetric nozzle (Z/W = 4)

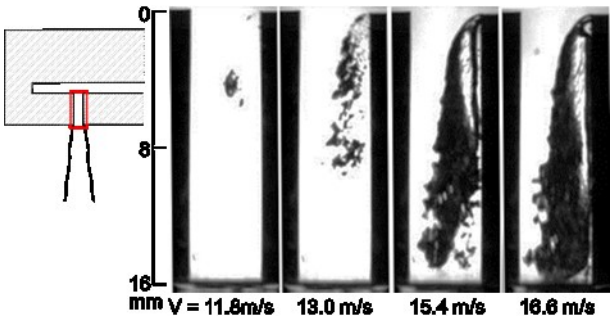

(c) Asymmetric nozzle (Z/W = 1)

Figure 2.8 Images of cavitation in the short nozzles (L/W = 4)

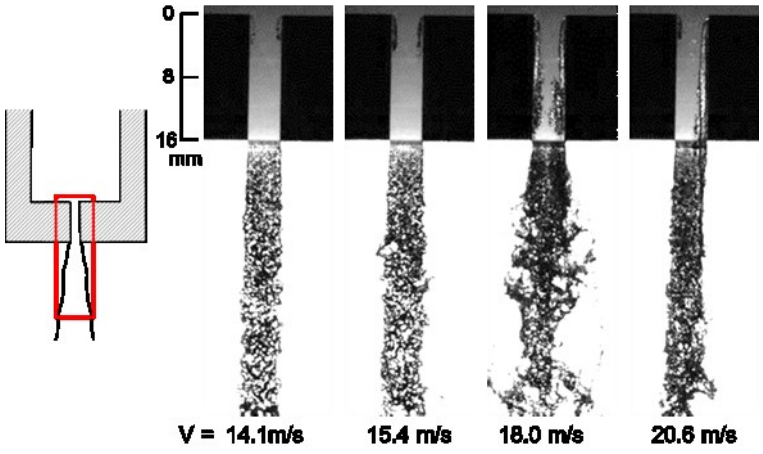

(a) Symmetric nozzle

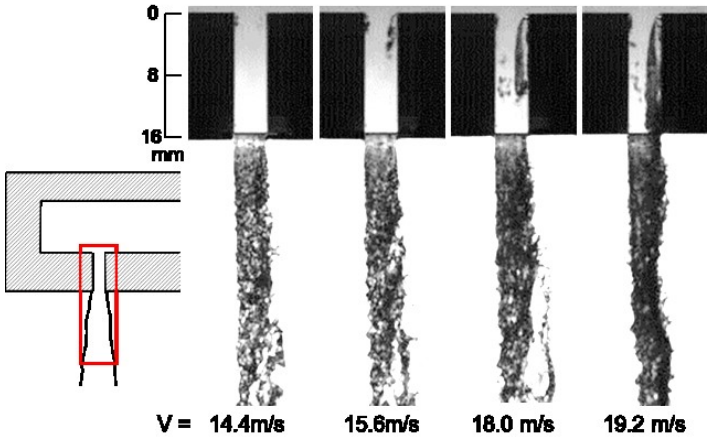

(b) Asymmetric nozzle (Z/W = 4)

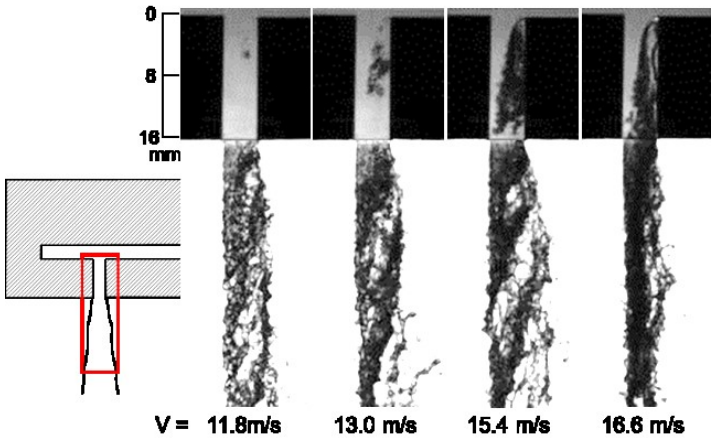

(c) Asymmetric nozzle (Z/W = 1)

Figure 2.9 Images of cavitation in the long nozzles and jets (L/W = 4)

Figure 2.10, Figure 2.11 (a), Figure 2.11 (b) and Figure 2.11 (c) show the measured L_C/L, θ_R, θ_L and $(\theta_R + \theta_L)$, respectively. The trends for L/W = 4 are similar to those for L/W =

1.5, *i.e.*, when needle lift is small (Z/W = 1), cavitation becomes thick and cavitation and hydraulic flip occur at small V.

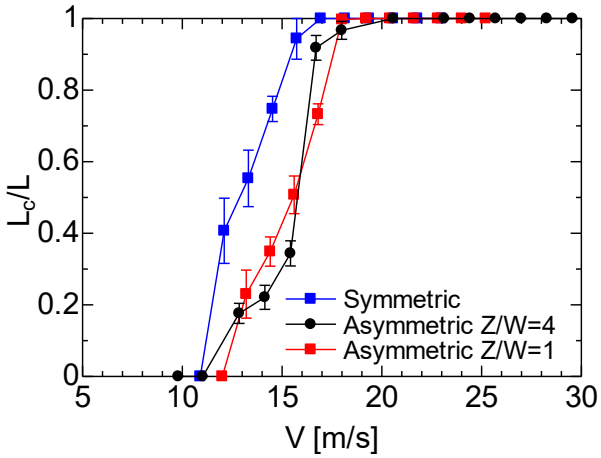

Figure 2.10 Cavitation length vs. mean flow velocity (L/W = 4)

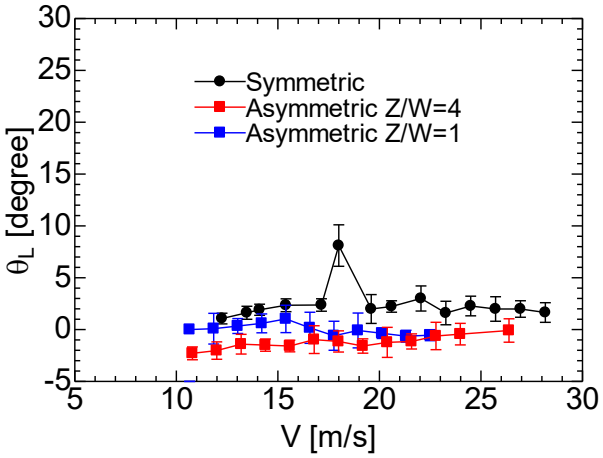

(a) Left jet angle

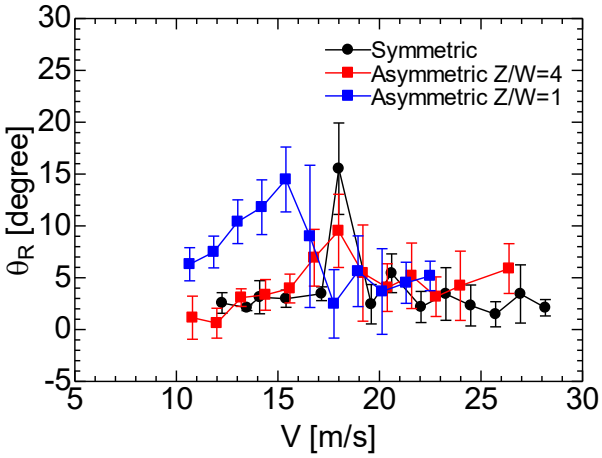

(b) Right jet angle

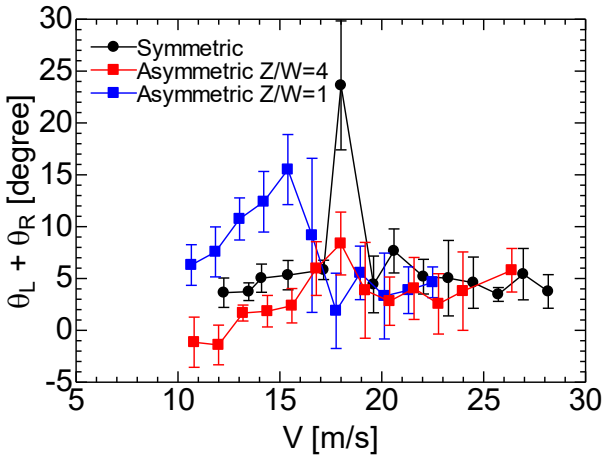

(c) Total jet angle

Figure 2.11 Jet angle vs. mean flow velocity (L/W = 4)

Comparison between the symmetric and asymmetric nozzles indicates that (1) a symmetric nozzle of L/W = 4 produces a very wide injection angle only at super cavitation, which is useful for a constant fuel injection rate, (2) an asymmetric nozzle of L/W = 4 gives an almost constant injection angle, which is preferable for atomizers used at unsteady V and various V.

In Figure 2.12, the profiles of cavitation are plotted for the symmetric nozzle of L/W = 4, the asymmetric nozzle of Z/W = 4, and that of Z/W = 1, where x is the horizontal position from the right inlet edge and y is the vertical position from the nozzle inlet. The cavitation profile, at super cavitation condition, describes the recirculation zone. The results show a thick cavitation at low needle lift of Z/W = 1 due to the large lateral velocity in the upstream. Thick cavitation corresponds to low local static pressure at vena contracta due to the large velocity at the core. As shown in Figure 2.11 (b), θ_R is large at super cavitation condition (V = 15.4 m/s) for Z/W = 1, which is induced by the thick cavitation.

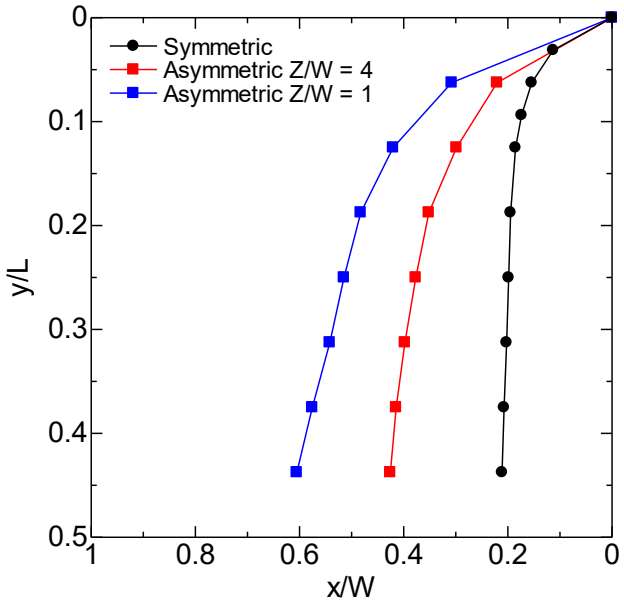

Figure 2.12 Cavitation profile

The cavitation number σ with a focus on back pressure P_b is defined by Eq. (2.1) [24]:

$$\sigma = \frac{P_b - P_v}{\frac{1}{2}\rho V^2} \tag{2.1}$$

where P_v is the vapor saturation pressure of liquid and ρ is liquid density. In this study, Pv is set to be 3.2 kPa for water at room temperature (25°C). It was confirmed that only the modified cavitation number σ_C defined by Eq. (2.2) based on local pressure at vena contracta, can predict cavitation length quantitatively for various symmetric nozzle. [26], [73]

$$\sigma_C = \frac{\frac{1}{2}\rho {V_{core}}^2 + P_{core} - P_v}{\frac{1}{2}\rho {V_{core}}^2} = {C_C}^2 \left[\frac{P_b - P_v}{\frac{1}{2}\rho V^2} + \frac{\lambda L}{D_H} + 1 \right] \tag{2.2}$$

where C_C is contraction coefficient defined by Eq. (2.3):

$$C_C = \frac{W_{core}}{W} = \frac{V}{V_{core}} \tag{2.3}$$

P_{core} is pressure at vena contracta defined by Eq. (2.4):

$$P_{core} = P_b + \frac{1}{2}\rho\left(V^2 - {V_{core}}^2\right) + \frac{\lambda L \rho V^2}{2D_H} \tag{2.4}$$

and D_H is hydraulic diameter of nozzle. The friction coefficient λ for the turbulence flow with $4000 - 10^5$ in the Reynolds Number Re is given by Eq. (2.5):

$$\lambda = \beta \frac{0.3164}{\mathrm{Re}^{0.25}} \tag{2.5}$$

where β is set to be 1.15 for rectangular nozzles with aspect ratio W/T of 4 and Reynolds Number Re is obtained from Eq. (2.6):

$$\mathrm{Re} = \frac{D_H V}{\upsilon} \tag{2.6}$$

where ν is the kinematic viscosity of the liquid, set to be 0.89×10^{-6} m^2/s in this study. Figure 2.13 illustrates the definitions of P_{core}, V_{core}, and other variables related to the modified cavitation number σ_C.

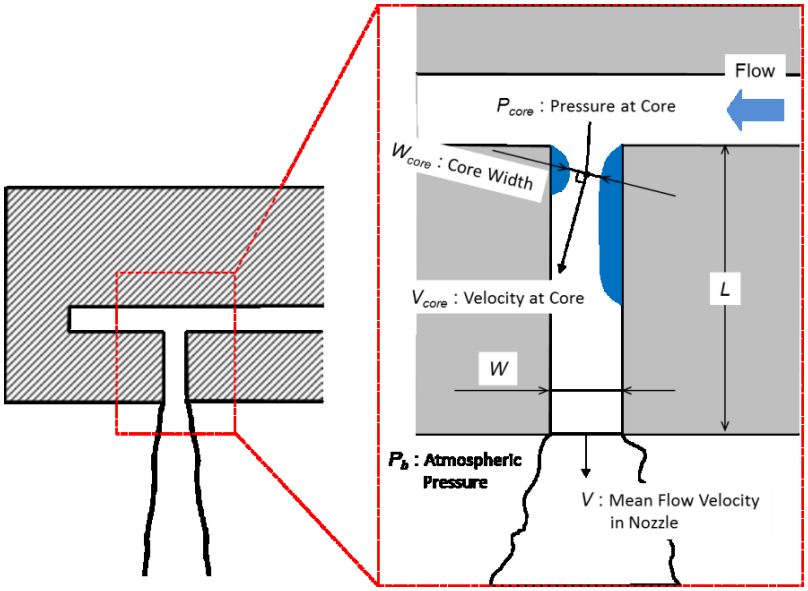

Figure 2.13 Definitions of P_{core}, V_{core}, and other variables to calculate cavitation number

As shown in Figure 2.14 (a), it is clear that cavitation length L_C for different nozzles cannot be uniquely predicted. On the other hand, as shown in Figure 2.14 (b) L_C for three different nozzles can be estimated by σ_C, i.e., cavitation inception at $\sigma_C = 1$, super cavitation at $\sigma_C = 0.8$ and hydraulic flip at $\sigma_C = 0.7$.

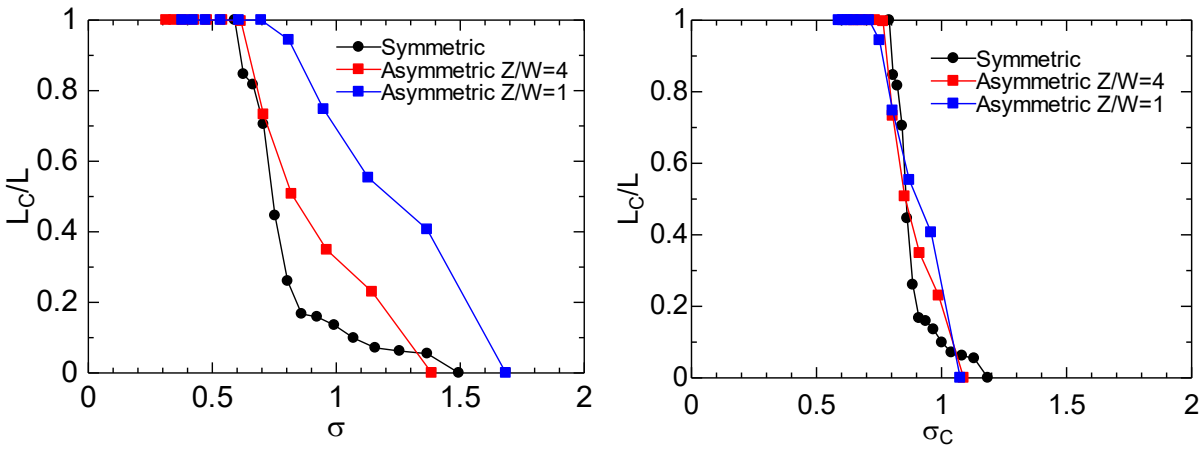

(a) Conventional Cavitation Number (b) Modified Cavitation Number

Figure 2.14 Cavitation number and modified cavitation number vs. cavitation length (L/W = 4)

As shown in Figure 2.11 (b) right jet angle θ_R vs. mean flow velocity (L/W = 4), in low needle lift of Z/W = 1, liquid jet angle θ_R is wide at developing and super cavitation regimes. Figure 2.15 shows a high-speed image at super cavitation (V = 13.0 m/s). At time t = 0 μs a cavitation cloud shed from the tail of the large cavitation zone moves downstream toward the exit of the nozzle. After the trail of cloud flows out of the nozzle, an anti-clockwise vortex induces a large liquid jet deformation as shown in the sequence below

(Figure 2.15), which is the reason of large θ_R. Figure 2.16 (b) shows the time history of the vertical distance L_{cloud} from the inlet to the tail of the cavitation cloud and that of θ_R, illustrated in Figure 2.16 (a). From the plotted graph, it is clear that the cavitation cloud leads to the large increase in jet angle θ_R with a certain time delay. In this case, the frequencies of cavitation cloud shedding and liquid jet deformation are approximately 500 Hz.

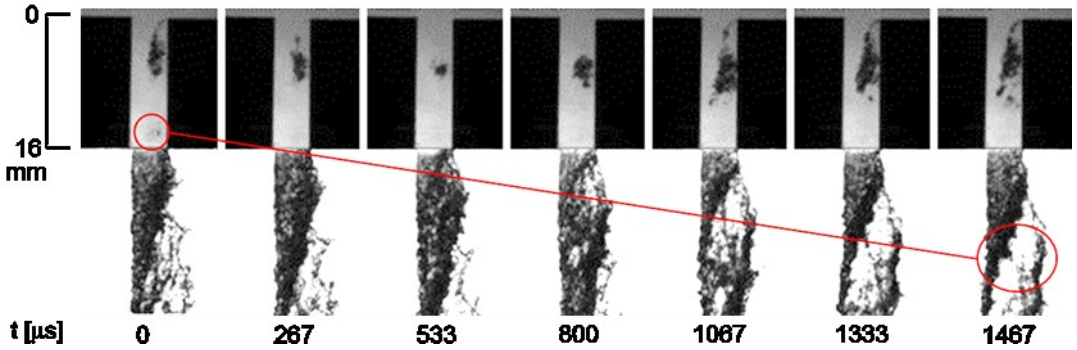

Figure 2.15 Effect of cavitation cloud on jet deformation (L/W = 4, Z/W = 1, V = 13.0 m/s)

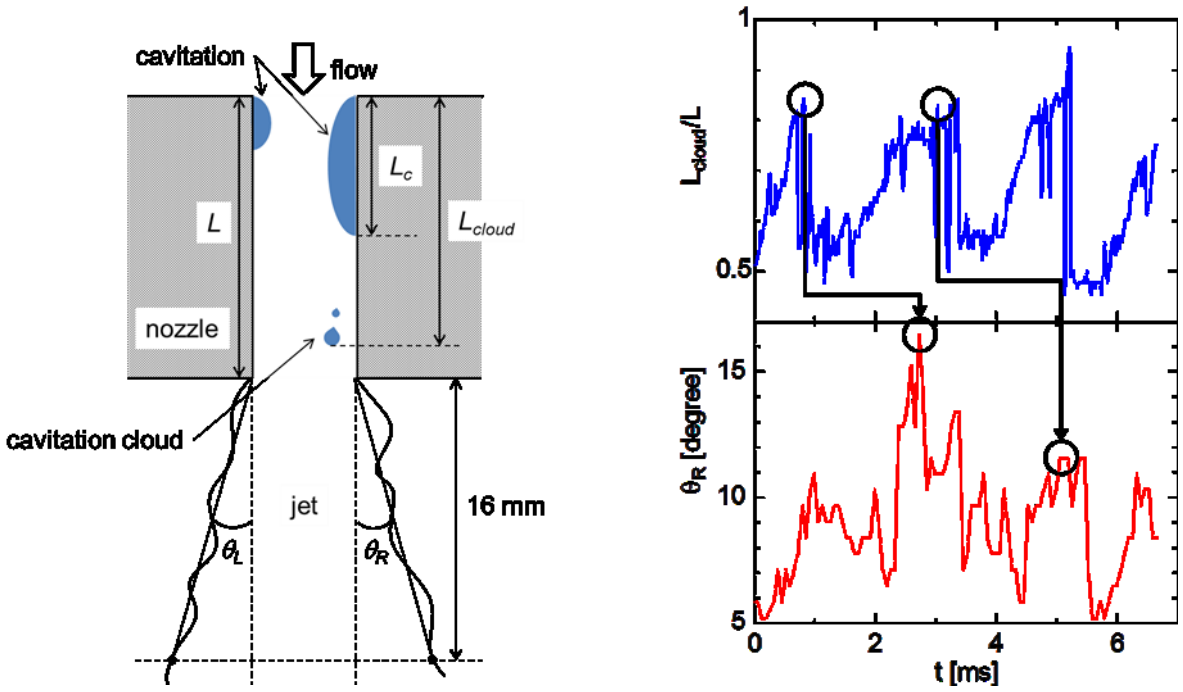

(a) Definition of L_{cloud} (b) L_{cloud} and θ_R

Figure 2.16 Relation between cavitation cloud and liquid jet angle (L/W = 4, Z/W = 1, V = 13.0 m/s)

Figure 2.17 shows a high speed image sequence for the asymmetric nozzle at super cavitation (L/W = 4, Z/W = 4, V = 18.0 m/s). The image sequence indicates the velocity difference between the interface moving velocities at the right and left sides of the injected liquid jets. The cavitating side (right side) has a lower velocity than the non-cavitating side (left side). The result explains the reason of the formation of slanted jet structure and suggests the asymmetric velocity distribution of fuel spray in a combustion chamber.

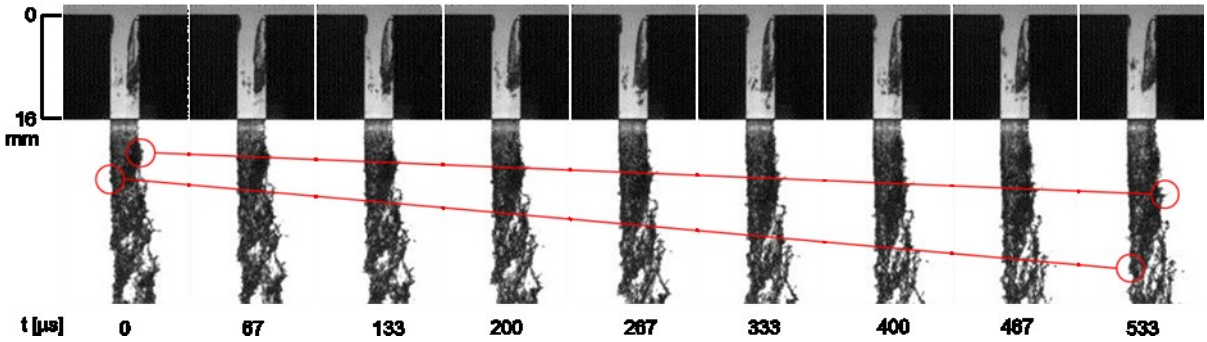

Figure 2.17 Velocity difference between cavitating side jet and non-cavitating side jet (L/W = 4, Z/W = 4, V = 18.0 m/s)

2.3.3 Effects of Nozzle Length on Cavitation and Jet

Figure 2.18-Figure 2.21 show the effects of the normalized nozzle length L/W on normalized cavitation length L_C/L as well as total jet angle ($\theta_R + \theta_L$). Figure 2.18 and Figure 2.19 are the results for Z/W = 4, and Figure 2.20 and Figure 2.21 are those for Z/W = 1. As shown in Figure 2.18 and Figure 2.20, for L/W = 1.5, cavitation and IHF occur at small V. As shown in Figure 2.19 and Figure 2.21, the total jet angle is large in the short nozzle of L/W = 1.5.

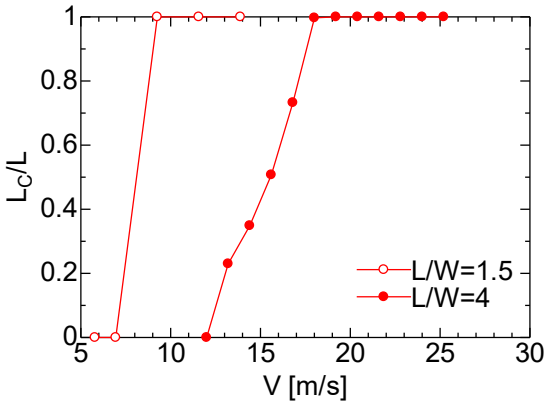

Figure 2.18 Cavitation length vs. mean flow velocity (Asymmetric, Z/W = 4)

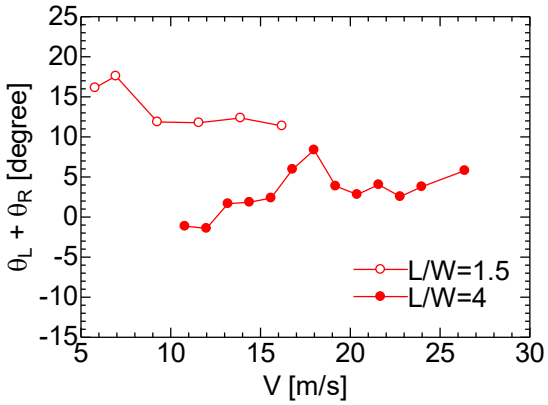

Figure 2.19 Total jet angles vs. mean flow velocity (Asymmetric, Z/W = 4)

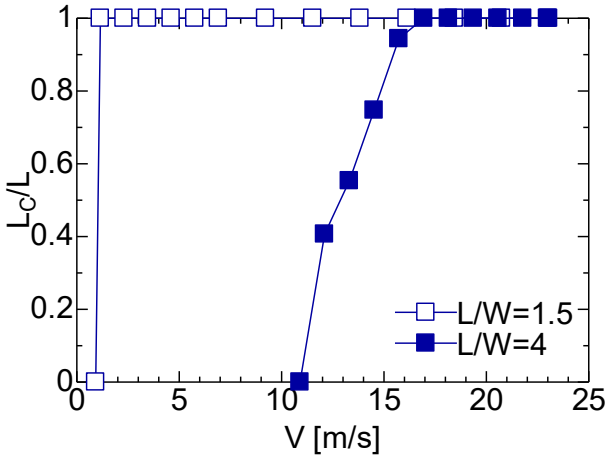

Figure 2.20 Cavitation length vs. mean flow velocity (Asymmetric, Z/W = 1)

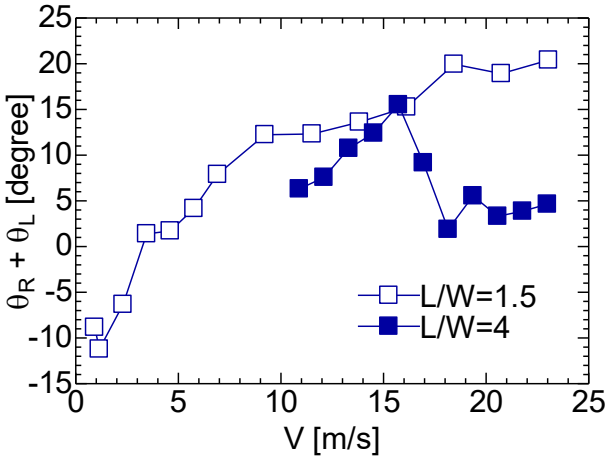

Figure 2.21 Total jet angles vs. mean flow velocity (Asymmetric, Z/W = 1)

The results give us the following guideline for various atomizers. (1) Symmetric and asymmetric nozzles of L/W = 4 produce a large injection angle at super cavitation, which improves air-fuel mixture in diesel engines. (2) Asymmetric short nozzle of L/W = 1.5 with Z/W = 1 produces a large and stable injection angle even at very low V, which is preferred as a low-pressure injector for gasoline engines.

2.4 Summary

Cavitation in symmetric and asymmetric nozzles was observed to examine the effects of asymmetric and lateral inflow on cavitation behavior and liquid jet atomization. The effects of the nozzle length and needle lift on cavitation and jet were also investigated. High-speed imaging was conducted to allow us to investigate cavitation cloud shedding and the jet deformation process. As a result, the following results were obtained.

(1) Cavitation occurs asymmetrically with an asymmetric inflow especially when needle lift is small. A higher needle lift results in smaller lateral inflow and, therefore, thinner cavitation which results in shorter cavitation and smaller liquid jet angle.

(2) An asymmetric cavitation induces asymmetric liquid jet and spray due to asymmetric cavitating nozzle flow. In addition, velocity distribution of the injected liquid jets is not uniform, that is, the cavitating side of the jet has slower velocity than the non-cavitating side, which may induce non-uniform velocity distribution of injected spray.
(3) Liquid jet deformation is enhanced by an asymmetric inflow when the needle lift is small because cavitation cloud often occurs at this needle lift condition. In the high-speed imaging results, it was confirmed that when a cavitation cloud was shed from the nozzle it had a large impact on liquid jet deformation.
(4) Cavitation and hydraulic flip in the short nozzles occur at very low velocity due to a separated boundary layer without a reattachment to the nozzle wall. Furthermore, the jet angle from a short nozzle is large.
(5) Modified cavitation number which is based on local liquid properties can be utilized to predict the onset of cavitation in a nozzle. Knowing the contraction coefficient, which is a unique number for specific nozzle, the modified cavitation number can be calculated.

Chapter 3
Cavitation in Cylindrical Nozzle with Asymmetric Inflow

3.1 Introduction

There has been a debate for many years that why the direction of the swirling drain flow appearing at the moment when remaining water in a bathtub becomes shallow is sometimes clockwise and counterclockwise in the Northern Hemisphere. We can easily calculate and confirm that the Coriolis force acting on the small drain flow is very small. From this matter, we have to focus on the fact that the drain flow becomes the swirling flow under the shallow water condition. The swirling flow can be caused by the fact that the upstream inflow with a large lateral momentum at the shallow water does not suddenly convert into the axial flow along the drain pipe with large axial momentum but prefers the swirling flow. One of the possible mechanisms of the string cavitation formation in a nozzle may be the same as the bathtub swirling flow.

In this study, cavitation in a cylindrical nozzle orifice of various transparent injectors is visualized with an asymmetric transverse inflow through a simple rectangular upstream channel, which is different from the symmetric single-hole nozzle with no string cavitation and is similar to the Valve-Covered Orifice (VCO) nozzle. Scaled-up acrylic nozzles with 4 mm in hole diameter D are used to clearly capture the cavitation. A high-speed camera is used to capture string cavitation formation and development as well as the unsteady liquid jet behavior. The effects of mean flow velocity V in the nozzle hole, the gap Z between the needle valve and its seat, and the upstream channel width W_U, which will be called as upper-volume width, on string cavitation are examined. The upper volume width is examined to investigate the effect of nozzle hole number, that in a multi-hole fuel injector, the larger the nozzle-hole number, the narrower upstream-volume width will be resulted, and vice versa, as illustrated in Figure 3.1. Numerical simulation of turbulent non-cavitating flow in the injector using OpenFOAM is conducted to examine the velocity and pressure distributions in the injector and upstream region.

A dimensionless number such as cavitation number and Reynolds number is not included in this study because we are not able to vary the cavitation number independent of the mean flow velocity since only one fluid, i.e. water, and one ambient pressure, i.e. atmospheric pressure, are used in the experiment. While the Reynolds number is not used because of the difficulty to define the characteristic length of the flow since there are two flow characteristics in the nozzle, i.e. separation flow and swirling flow. Therefore, in this study, any dimensionless number is not used but mean flow velocity.

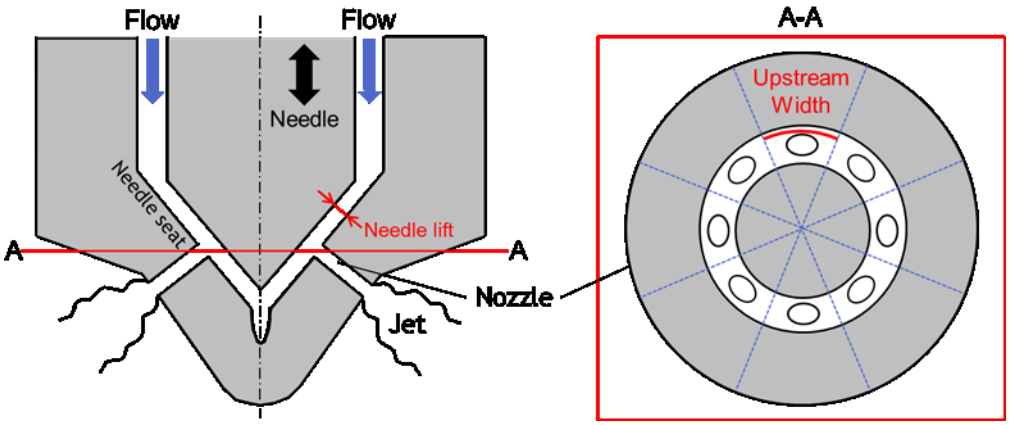

Figure 3.1 Valve-Covered Orifice (VCO) Nozzle

3.2 Experimental Setup

Figure 3.2 shows the schematic of the experimental apparatus. Filtered tap water at 300 K in a tank was injected at constant flow rates through a valve, a flowmeter, and a transparent nozzle into ambient air. The valve was adjusted to control the liquid flow rate, which was measured using a flow meter. Knowing the liquid flow rate and nozzle hole cross-sectional area, the mean flow velocity V flowing through the nozzle hole was calculated. A pressure gauge was installed at the upstream of the nozzle hole to measure injection pressure. Still and high-speed images of cavitation and jets were taken using a high-speed camera (Phantom V211) with 50 fps for random sampling imaging, and 2000, 6000, 10000 or 20000 fps for high-speed imaging. A metal-halide lamp (Kyowa Co. Ltd., MID-25FC) was used as the backlight source. A diffuser sheet was placed between the nozzle and backlight source to uniformly distribute the backlight into the camera sensor.

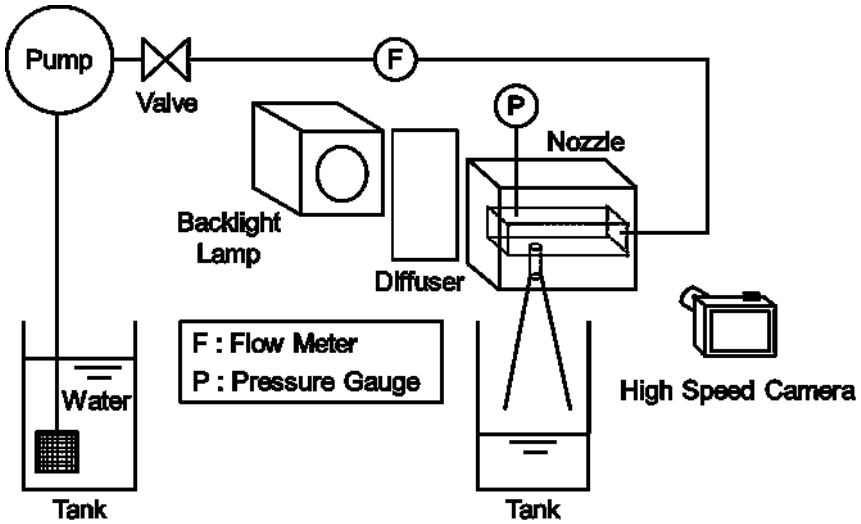

Figure 3.2 Schematic of experimental setup

In this experiment, a transparent nozzle made from acrylic was used, whose geometry is simplified and represent a sac type single hole nozzle and a Valve-Covered-Orifice (VCO)

nozzle. While the real injector used in a diesel engine is a multi-hole nozzle, in this experiment a single-hole nozzle was used to avoid dissimilarity which would exist if we use a multi-hole nozzle and thus a large deviation of data can be reduced. Figure 3.3 (a) and (b) show the schematics of the sac type single-hole nozzle and the VCO nozzle, respectively. Liquid fuel flows into a single-hole nozzle with a symmetric inflow and into a VCO nozzle with an asymmetric transverse inflow fed through the gap Z between the needle valve and the seat. Liquid fuel flows into a nozzle hole asymmetrically in any multi-hole nozzle, which may play an important role in cavitating flow and the resulting spray. Acrylic model injectors of 4 mm in diameter D and 16 mm in length L (length-to-diameter ratio L/D is 4) were made as shown in Figure 3.3 (c) and (d) to examine the effects of the asymmetric inflow on cavitation as well as the discharged liquid jets. The gap Z was varied (Z = 2, 4, 8, 12, 16, 20, 24, 28 and 32 mm, i.e., needle lift ratio Z/D = 0.5, 1, 2, 3, 4, 5, 6, 7 and 8) to investigate the effects of needle lift on string cavitation and the jet. Injectors with two upper-volume widths W_U were tested, i.e., wide upper-volume (W_U = 30 mm, W_U/D = 7.5) and narrow upper-volume (W_U = 15 mm, W_U/D = 3.75), which examine the effects of the number of nozzle holes for a multi-hole injector.

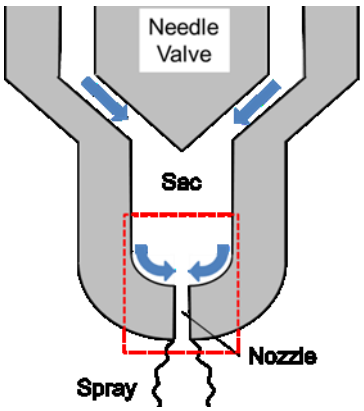

(a) Single hole nozzle

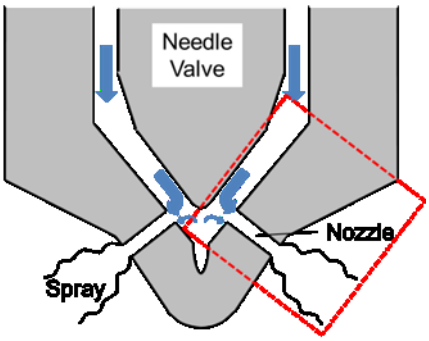

(b) Valve-Covered-Orifice (VCO) nozzle

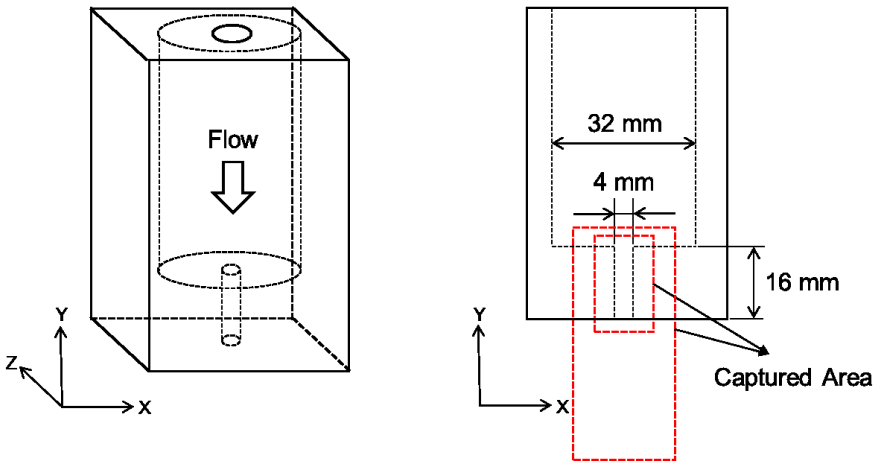

(c) Symmetric single hole-nozzle

Figure 3.3 Schematic of the test nozzles

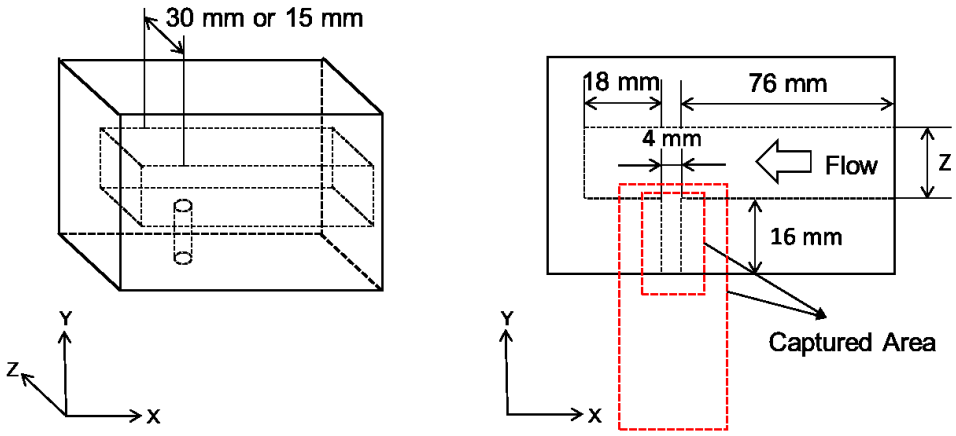

(d) Asymmetric VCO nozzle

Figure 3.3 Schematic of the test nozzles

3.3 Numerical Simulation Setup

An open-source CFD software, OpenFOAM version 2.1.1, was used for the calculation of the flow in the nozzle hole and the upstream channel. Cavitation was not taken into account in the simulation to simply examine the pressure drop induced by the swirling flow in the upstream channel and the nozzle hole. The schematic of a computational grid is shown in Figure 3.4. The grid represents the injector of W_U/D = 7.5 and Z/D = 4. Another simulation with Z/D = 2 was also conducted to examine the effects of needle lift Z/D. Continuous outflow condition was set at the exit of the nozzle. The nozzle outlet velocity V was set to 17.0 m/s. The nozzle hole length was set to be 60 mm, which is much longer than that of the experimental nozzle hole, 16 mm, to reduce the effect of the unknown outlet boundary condition, swirling or non-swirling flow. The standard k-ε turbulence model was used in the calculation together with the wall function near the wall. Once a swirling flow is formed, the flow distribution at the inlet of the upstream channel may become non-uniform. Hence, the flows in the longer upstream channel of 120 mm were simulated, and the uniform inlet velocity of V_{in} = 0.445 m/s for Z/D = 2 and V_{in} = 0.223 m/s for Z/D = 4 at the inlet (A-A cross-section) of the upstream channel with a tiny constant velocity gradient of $\partial u/\partial y = 4.2 \times 10^{-5}$ s^{-1}, i.e. $V_{in} \pm 6.3\times10^{-7}$ m/s near the front and back walls as a possible trigger of the asymmetric swirling flow was set. Note that by changing the velocity gradient $\partial u/\partial y$ to 8.4×10^{-5} s^{-1}, the obtained results are almost the same as those with $\partial u/\partial y = 4.2\times10^{-5}$ s^{-1}.

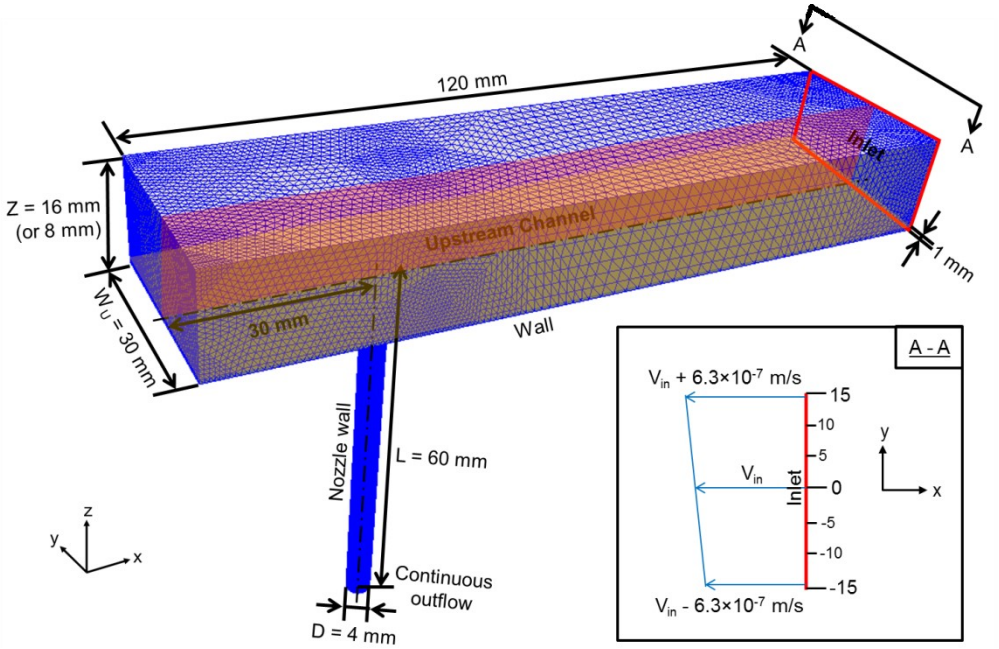

Figure 3.4 Computational grid ($W_U/D = 7.5$ and $Z/D = 4$)

3.4 Results and Discussion

3.4.1 Visualization Results

Figure 3.5 shows the images of cavitation in a symmetric nozzle and its liquid jet. The dark areas near the nozzle-hole side walls are due to total reflection since the refractive index of water is lower than that of acrylic. There is no cavitation for $V < 10.4$ m/s and the liquid jet is wavy. Cavitation, which can be classified as recirculation-flow-induced cavitation (RIC), starts to appear near the nozzle hole entrance at $V = 10.4$ m/s and the liquid jet is still wavy but with a slightly wider angle than that of the non-cavitation slower jet due to the slightly larger interaction between the wavy liquid jet and surrounding gas. When V is increased up to 12.7 m/s, cavitation exceeds the middle of the nozzle hole, and the liquid jet deforms largely with some ligaments and droplets. The cavitation length almost reaches the nozzle exit at $V = 13.1$ m/s and the liquid jet deforms drastically. This phenomenon, so-called super cavitation, is well known as the most preferred cavitation to enhance liquid atomization [17], [19], [24] but the most unfavorable cavitation because it induces erosion [74]. When $V \geq 13.5$ m/s, cavitation switches to hydraulic flip which suppresses the liquid jet deformation into a very narrow smooth jet with a glassy structure, which is not preferred in engine combustion. These results reproduce the regime transition reported in previous reports [17], [24], that is, cavitation inception, developing cavitation, super cavitation and hydraulic flip.

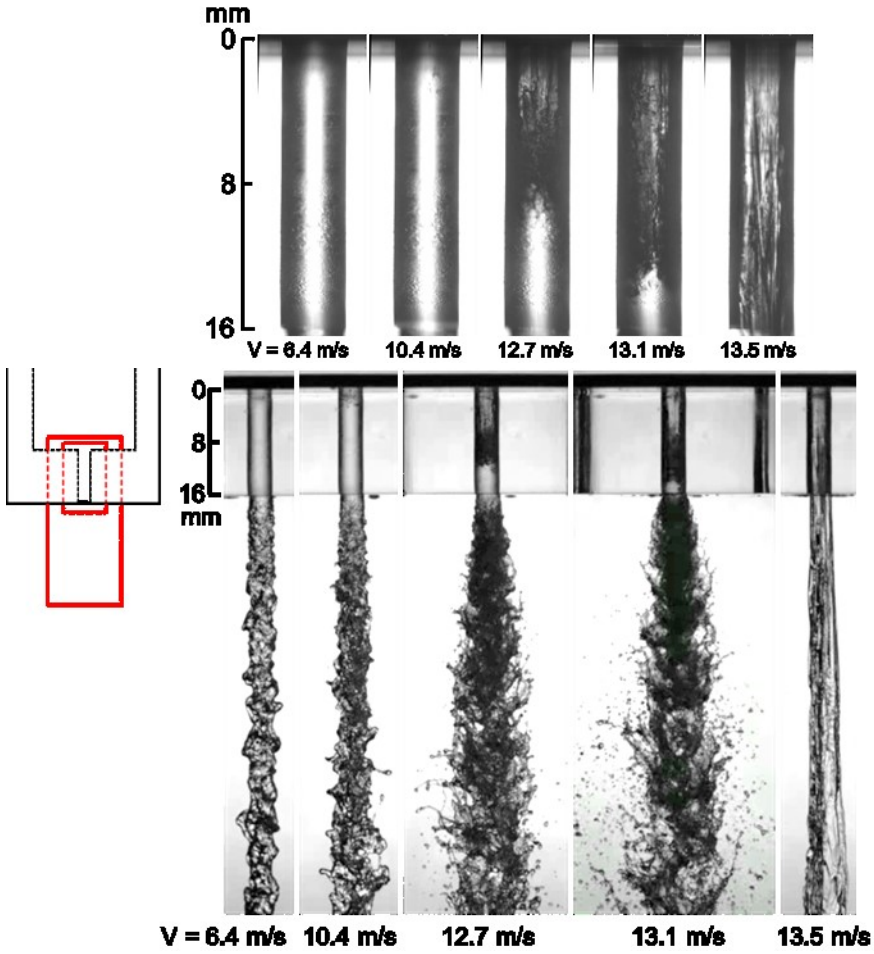

Figure 3.5 Cavitation in the symmetric nozzle and jets

Figure 3.6-Figure 3.8 show the images of cavitation in the asymmetric nozzles at wide upper-volume ($W_U/D = 7.5$) and their liquid jets. All the cases for $W_U/D = 7.5$ were classified into the following two categories, i.e. high needle lift ($Z/D \geq 4$) and low needle lift ($Z/D < 4$), based on the string cavitation formation which is explained later. Figure 3.6 shows cavitation and the jet at high needle lift of $Z/D = 8$ where string cavitation is never observed, while Figure 3.8 shows those at low needle lift of $Z/D = 0.5$, with string cavitation. Figure 3.7 shows those at the transition between high and low needle lift of $Z/D = 3$, where string cavitation sometimes appears and it was classified into low needle lift with occasional string cavitation.

As shown in Figure 3.6, no cavitation appears in the nozzle hole at low mean flow velocity of $V < 10.4$ m/s. RIC starts to appear at the nozzle hole inlet at $V = 10.4$ m/s. With a slight increase in V, cavitation extends to near the nozzle exit ($12.7 \text{ m/s} \leq V < 13.5$ m/s), i.e. super cavitation, and induces a widely atomized jet and spray. An increase in V which exceeds 14.3 m/s results in hydraulic flip with no reattachment to the nozzle hole wall so that the separated flow flows straight through the nozzle exit. As we can see in Figure 3.6, cavitation regime transition is similar with that in the symmetric nozzle shown in Figure 3.5. However, the cavitation along the right wall is slightly longer than that along the left wall due

to the inflow from right upstream. As a result, the liquid jet also deforms slightly asymmetrically, that is, the right side of the liquid jet always shows a wider angle than the left one, especially at super cavitation condition (V = 13.5 m/s). When the cavitation turns to hydraulic flip (V = 14.3 m/s), a smooth jet with a glassy structure is formed on the right side which means the hydraulic flip perfectly occurs only on the right side of the nozzle hole while the other side is imperfect hydraulic flip which results in a dense liquid jet.

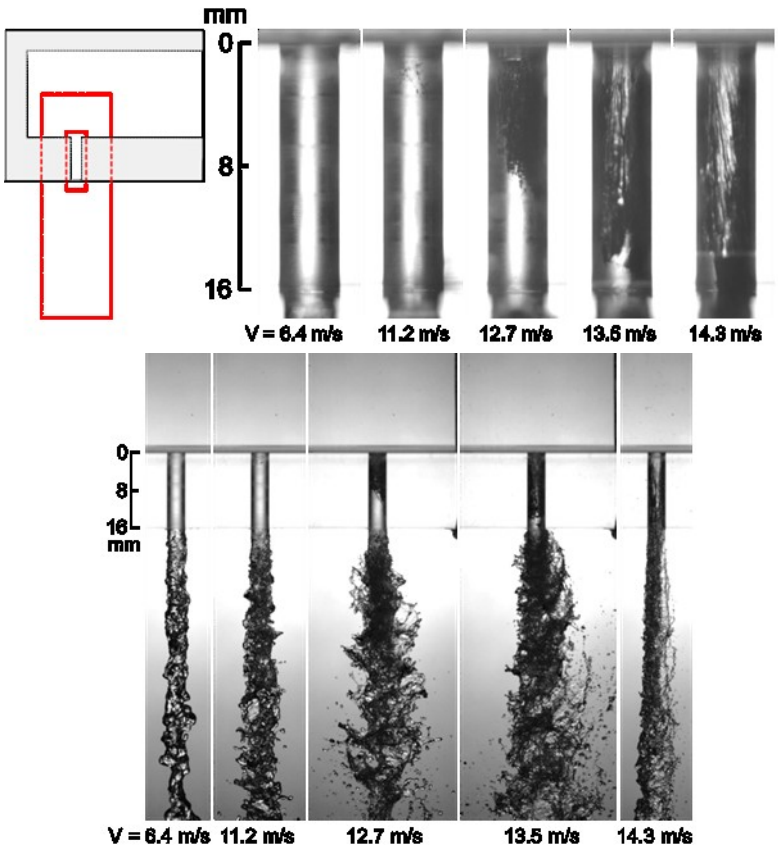

Figure 3.6 Cavitation and jets at wide upper-volume (W_U/D = 7.5) and high needle lift (Z/D = 8)

Photos of cavitation and the jet for the asymmetric nozzle of Z/D = 3 at the transition between high and low needle lifts are shown in Figure 3.7. At V = 3.2 m/s, there is no cavitation inside the nozzle hole and the liquid jet is wavy with some ligaments. A slightly twisted thick string cavitation, which can be classified as helical-flow-induced cavitation (HIC), sometimes appears along the axis of the nozzle hole from the needle wall to the nozzle exit and sometimes does not at V ≥ 4.0 m/s. The high velocity of V > 11.9 m/s results in a frequent string cavitation and RIC occur sometimes simultaneously where the string cavitation occurs along the nozzle hole with a slight tilt from the left inlet to right exit and the short RIC occurs near the right side of the nozzle hole inlet. The combination of the RIC and the tilted string cavitation induces the agitated weak hollow cone liquid skirt which tears near the nozzle on the right side of the film and results in larger spray angle for the right side while a dense spray indicated with a darker color is observed on the left side.

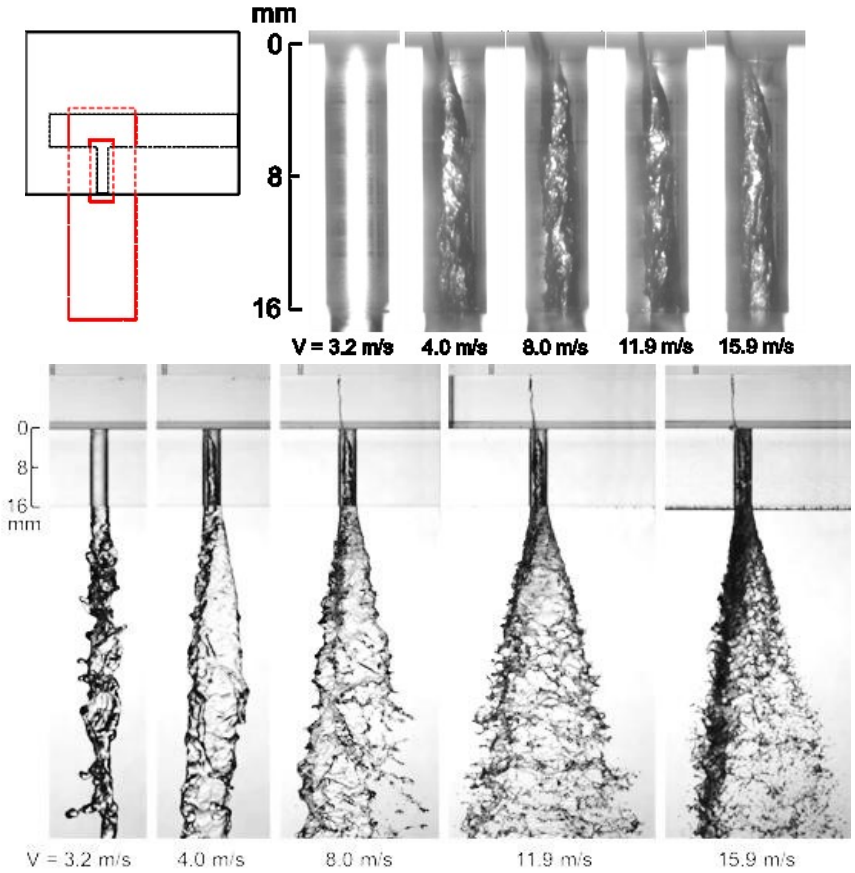

Figure 3.7 Occasional string cavitation and jets at wide upper-volume ($W_U/D = 7.5$) and medium needle lift ($Z/D = 3$)

Cavitation and the jets in the asymmetric nozzle with low needle lift of $Z/D = 0.5$ are shown in Figure 3.8. For $V \leq 0.8$ m/s cavitation does not appear and a twisted liquid jet is formed. String cavitation and a hollow cone liquid skirt are always observed at higher velocity V. The low needle lift, which results in high transverse inflow momentum, enhances string cavitation, i.e., it appears at very low mean flow velocity V of 1.6 m/s. The hollow cone spray induced by the string cavitation at low needle lift tends to spread wider than that at high lift without string cavitation because of a large centrifugal force acting of the liquid skirt. Note that the string cavitation below the needle valve wall in the upstream channel is almost always slightly slanted from the left top to the right exit due to the asymmetric transverse inflow from the right upstream channel, which results in a slightly tilted hollow cone liquid skirt. At V = 3.2 m/s, the spray breakup occurs at far downstream, i.e. about 2.5L distance from nozzle exit, while at higher V of 4.8 m/s the spray breakup occurs closer, i.e. about 2L distance from nozzle exit.

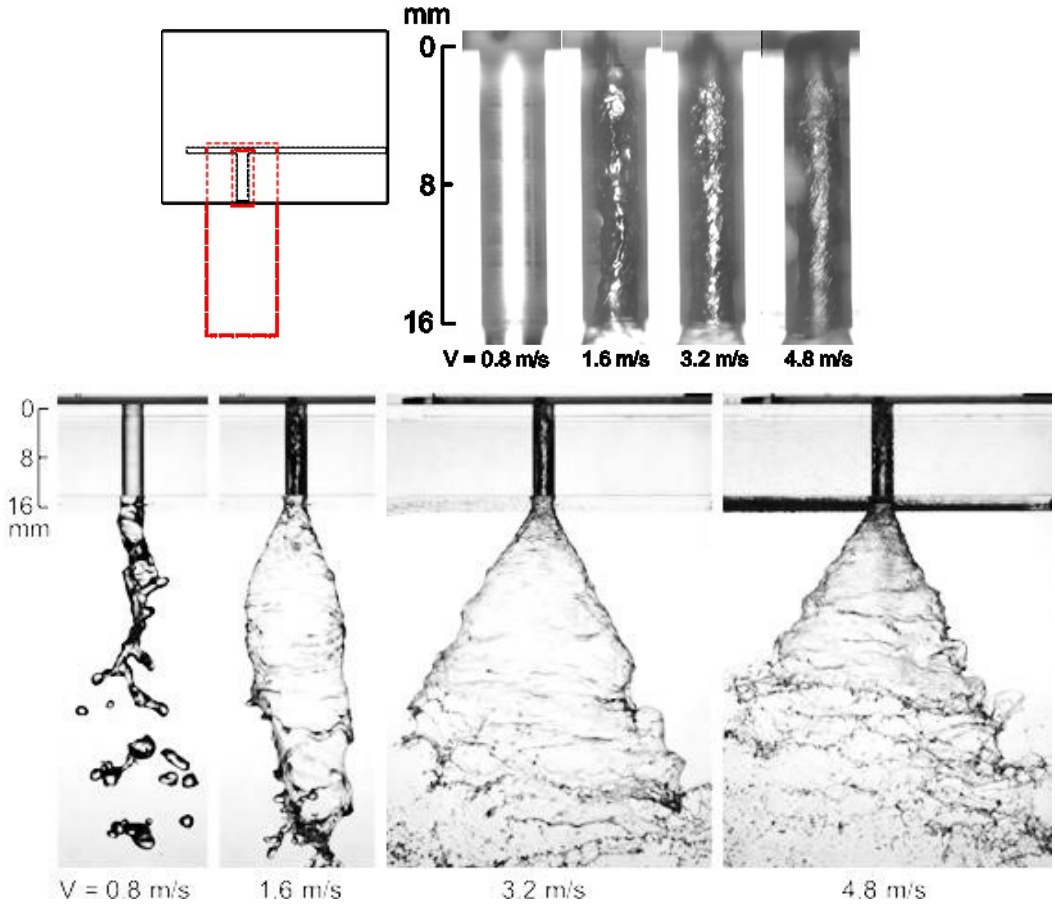

Figure 3.8 Cavitation and jets at wide upper-volume (W_U/D = 7.5) and low needle lift (Z/D = 0.5)

Images of cavitation and the jets at the narrow upper-volume of W_U/D = 3.75 and needle lift ratios Z/D = 4 and 0.5 are shown in Figure 3.9 and Figure 3.10, respectively. As shown in Figure 3.9, cavitation and jet behaviors at Z/D = 4 are similar with those in the nozzle at wide upper-volume of W_U/D = 7.5 and high lift of Z/D = 8. It should be noted that the length of cavitation along the right wall is more clearly longer than that along the left wall due to the larger lateral momentum of the right inflow caused by the constraint from the front and back walls. As a result, the liquid jet deforms asymmetrically with a wider angle on the right side of the jet, especially when super cavitation occurs at V = 13.5 m/s.

As shown in Figure 3.10, at narrow upper-volume of W_U/D = 3.75 and low needle lift of Z/D = 0.5 the trends of cavitation and the jet are similar to those observed at wide upper-volume of W_U/D = 7.5 and low needle lift of Z/D = 0.5, i.e. a slanted string cavitation appears at very low V. However, the resulting jet angle at narrow upper-volume of W_U/D = 3.75 is much smaller than that at W_U/D = 7.5, as shown in Figure 3.10 at V = 8.8 m/s and 11.1 m/s. The result implies the weak helical flow in the upstream channel and the nozzle hole for narrow upper-volume which results in a dense spray at high-velocity condition.

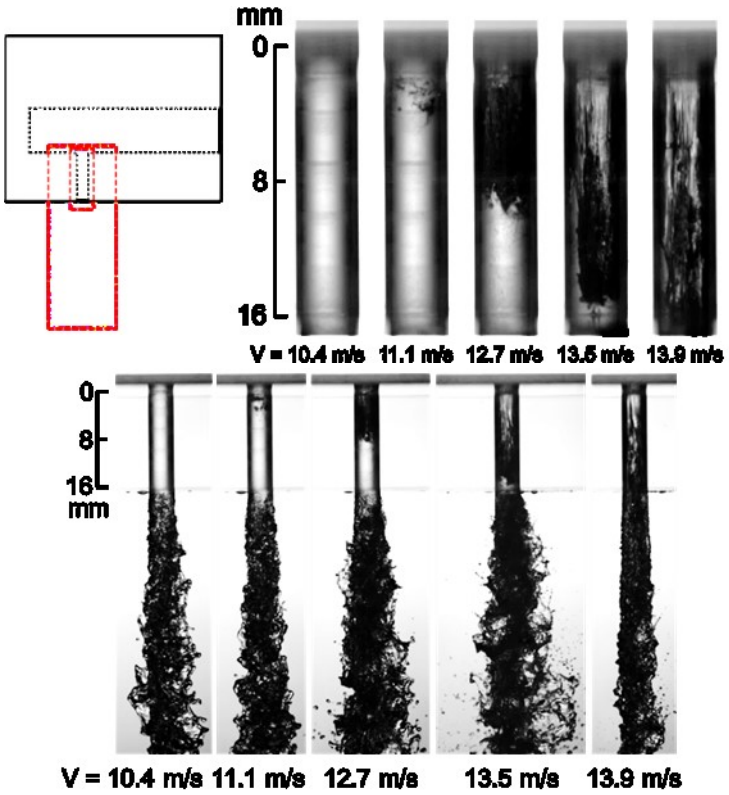

Figure 3.9 Cavitation and jets at narrow upper-volume ($W_U/D = 3.75$) and high needle lift ($Z/D = 4$)

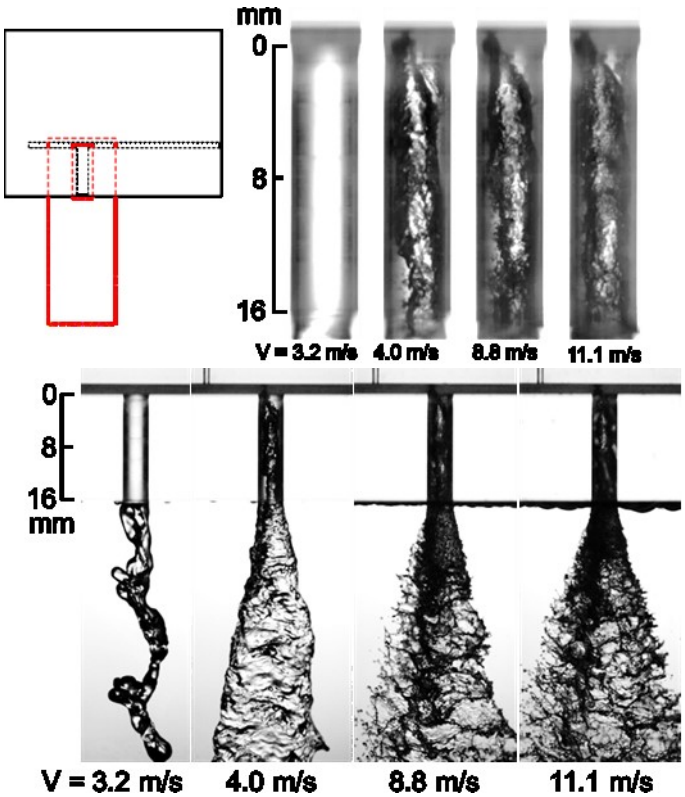

Figure 3.10 Cavitation and jets at narrow upper-volume ($W_U/D = 3.75$) and low needle lift ($Z/D = 0.5$)

3.4.2 Cavitation Regime Maps

After all the observation, the string cavitation regime maps were presented, where it is classified as string cavitation even if it appears only for a very short time. Figure 3.11 (a) and (b) show the string cavitation regime maps with wide upper-volume of W_U/D = 7.5 and narrow upper-volume of W_U/D = 3.75, respectively. By using the string cavitation regime maps for given upper-volume width, the cavitation regime can be predicted based on mean flow velocity V in the nozzle hole and needle lift ratio Z/D under the atmospheric pressure condition. As mentioned above, it was defined into two categories, i.e. high needle lift with no string cavitation and low needle lift with possible string cavitation. It should be noted that at high needle lift string cavitation will never be observed even at very large V with a very large lateral momentum while at low needle lift string cavitation appears even at very low V. The difference clearly indicates that low needle lift enhances the helical flow and formation of string cavitation. By comparing the two maps, we can find that in the case of wide upper-volume of W_U/D = 7.5 the boundary between the two categories lies between Z/D = 3 and 4, while in the case of half upper-volume of W_U/D = 3.75 the category boundary lies at almost half lift, i.e., between Z/D = 1 and 2. It should also be pointed out that the minimum velocity of the onset of string cavitation is proportional to the needle lift ratio Z/D, in other words, is in inverse proportion to lateral inflow momentum in the upstream channel. These results indicate that string cavitation is strongly governed by lateral momentum in the upstream channel. Note that there is a transition region between high and low lifts, where string cavitation sometimes appears and sometimes not, which makes it difficult to control fuel spray characteristics.

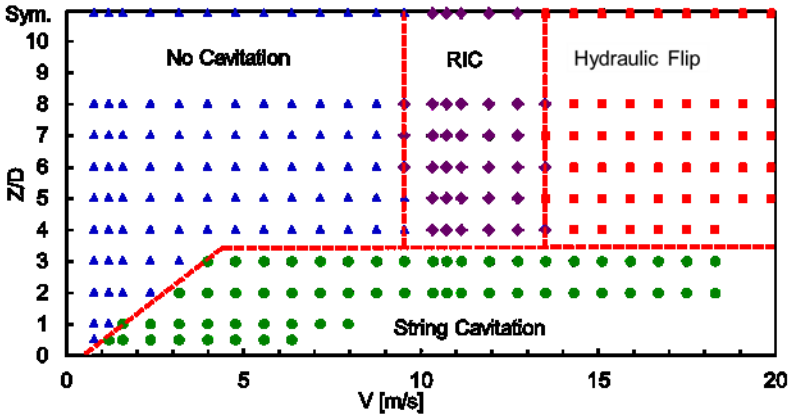

(a) Wide upper-volume W_U/D = 7.5

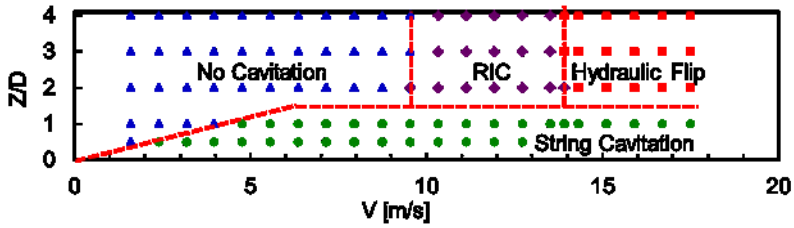

(b) Narrow upper-volume W_U/D = 3.75

Figure 3.11 Cavitation regime maps

3.4.3 Image Analysis

Figure 3.12 illustrates the definition of liquid jet angle. The liquid jet angle was measured at 8D (= 32 mm) downstream of the nozzle exit. This distance was selected since the liquid deformation induced by the nozzle flow does not clearly occur at the shorter distance and the liquid jet is too much affected by ambient air at far downstream. The measurement was carried out for both left and right jet angles θ_L and θ_R while the total jet angle θ is the sum of the left and right angles.

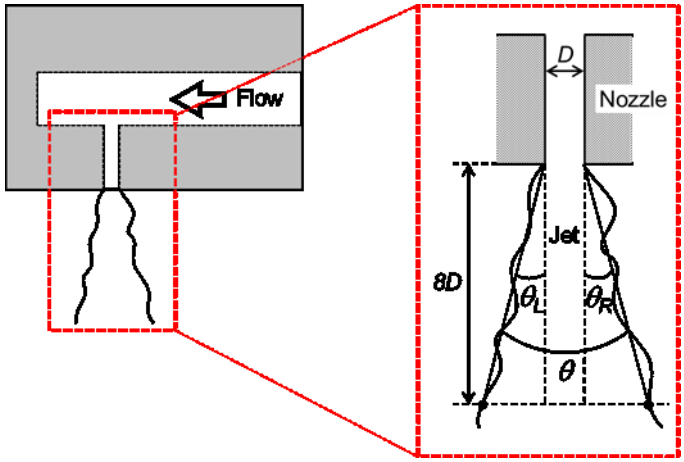

Figure 3.12 Definition of liquid jet angle

Figure 3.13 (a), (b) and (c) show the θ_L and θ_R for low Z/D of Z/D $\leq$ 3, those for high Z/D of Z/D = 5 and 8, and total jet angle θ for all Z/D in the case of wide upper-volume of W_U/D = 7.5. The left jet angle θ_L is slightly wider than the right jet angle θ_R for very low lift ratios Z/D $\leq$ 2 due to the slanted string cavitation, while for Z/D = 3 θ_R is slightly wider than θ_L as explained above. As shown in Figure 3.13 (a), for low needle lift (Z/D $\leq$ 3) of string cavitation category the jet angles θ_L and θ_R increase with flow velocity V due to the large centrifugal force. On the other hand, as shown in Figure 3.13 (b), for high needle lift of Z/D $\geq$ 4 without helical flow in the nozzle hole the jet angles θ_L and θ_R significantly increase at super cavitation especially for θ_R, and suddenly drop at hydraulic flip. Total jet angle θ is shown in Figure 3.13 (c). It increases with decreasing needle lift Z/D and it is clearly very large at low lift category due to the formation of hollow cone liquid skirt.

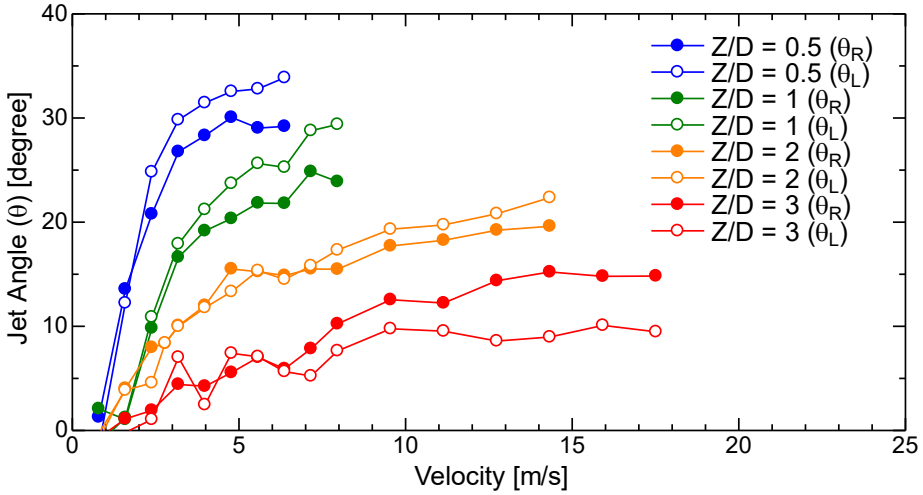

(a) Low needle lift (Z/D ≤ 3)

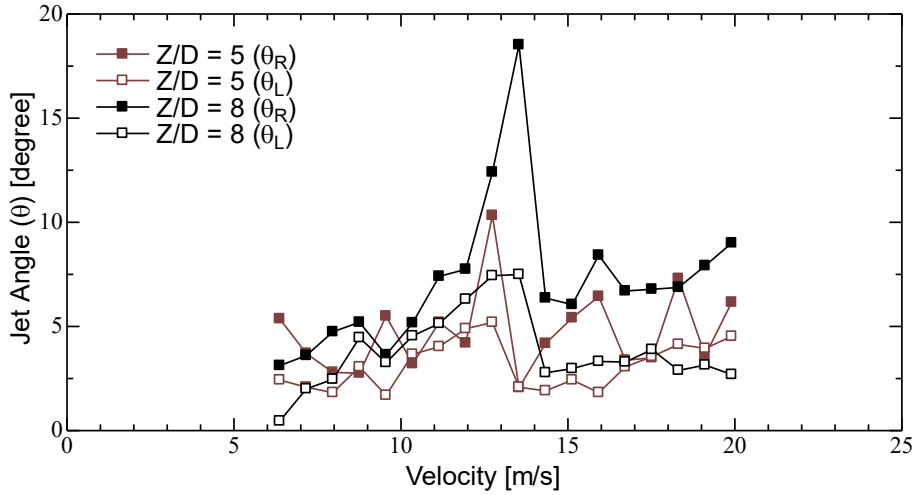

(b) High needle lift (Z/D = 5, 8)

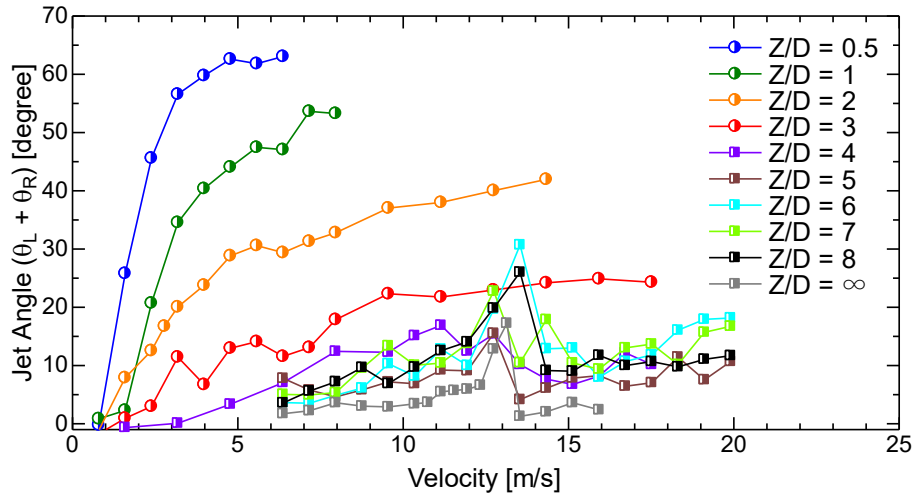

(c) Total jet angle

Figure 3.13 Jet angle at wide upper-volume (W_U/D = 7.5)

When cavitation forms, discharge coefficient decreases and reaches its minimum value when the cavitation is fully developed. Figure 3.14 shows the measured discharge coefficient C_d defined by Eq. (3.1):

$$C_d = \sqrt{\frac{\rho V^2}{2\Delta P}} \tag{3.1}$$

where ρ is the liquid density, and ΔP is the injection pressure difference. The discharge coefficient C_d does not so much depend on mean velocity V in the nozzle hole but drops slightly by RIC and drops largely by hydraulic flip. For low lift of Z/D ≤ 3, C_d does not depend on V. It takes an extremely small value and decreases with decreasing lift Z/D.

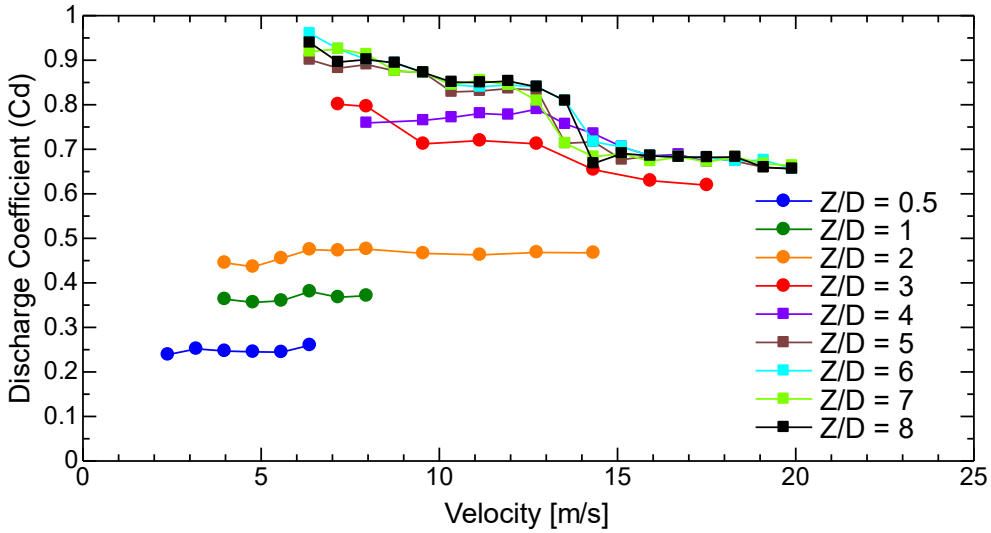

Figure 3.14 Mean flow velocity V versus discharge coefficient C_d at wide upper-volume ($W_U/D = 7.5$)

String cavitation diameter ratio D_{SC}^* is defined by Eq.(3.2):

$$D_{SC}^* = \frac{D_{SC}}{D} \tag{3.2}$$

where D_{SC} is the string cavitation diameter measured at 5/8L, i.e., 10 mm, from the nozzle hole inlet where the diameter is almost steady and constant along the nozzle hole axis, as illustrated in Figure 3.15. Note that the string cavitation diameter was measured from the backlight image, which is the interpretation of integrated string cavitation width along the whole depth of the nozzle hole. String cavitation is assumed as a cylinder shape since the real shape of its peripheral surface cannot be seen by the backlight imaging.

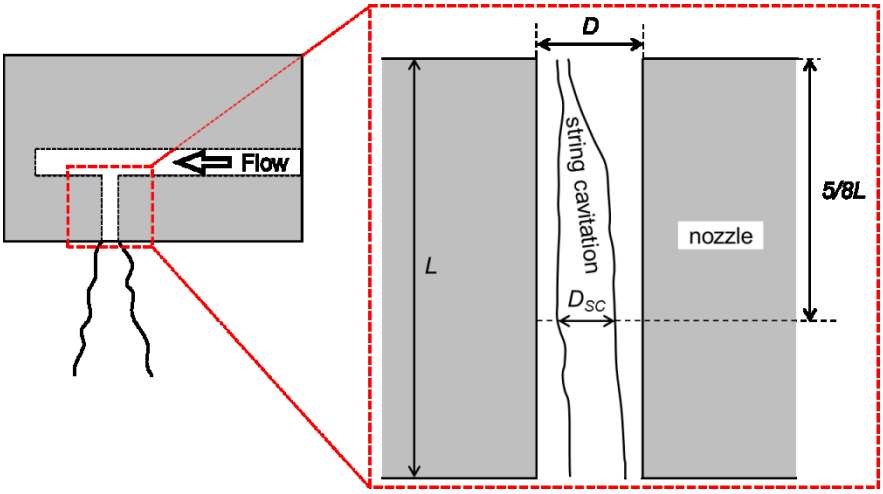

Figure 3.15 Definition of string cavitation diameter

Figure 3.16 illustrates the light refraction, which is used to correct measured string cavitation diameter. When measuring the string cavitation diameter, we have to note that the string cavitation image captured by the camera sensor is a result of light refraction in the nozzle due to the refractive index difference between the water in the nozzle and the acrylic nozzle. From Snell's law as defined in Eq. (3.3):

$$\frac{\sin\theta_1}{\sin\theta_2} = \frac{n_2}{n_1} \tag{3.3}$$

the refraction effect can be calculated and thus the corrected string cavitation diameter can be obtained. Note that the string cavitation is assumed to be cylindrical and located in the center of the nozzle. θ_1 is the angle of the incoming light to the normal line N of the cylindrical surface. The refractive index of acrylic n_1 is 1.49 and that of water n_2 is 1.33. θ_2 is the refracted angle of the incoming light when entering the nozzle filled with water. From Eq. (3.3), the refracted angle θ_2 can be calculated by Eq. (3.4):

$$\theta_2 = \arcsin\left(\frac{n_1 \sin\theta_1}{n_2}\right) \tag{3.4}$$

By knowing θ_2 we can draw a refracted light line and obtain the angle θ_r between two radius lines and the angle θ_x between the radius line and X-axis. The refracted light to the camera, which shows the interface of string cavitation, is depicted by D_{SC}' and can be obtained by Eq. (3.5):

$$D_{SC}' = 2r \times \sin\theta_3 \tag{3.5}$$

Knowing the D_{SC}', θ_2, θ_x, and the nozzle radius r, the corrected string cavitation diameter D_{SC} can be obtained by Eq. (3.6):

$$D_{SC} = 2r \times \frac{\sin\theta_1}{\sin(180 - \theta_2 - \theta_x)} \tag{3.6}$$

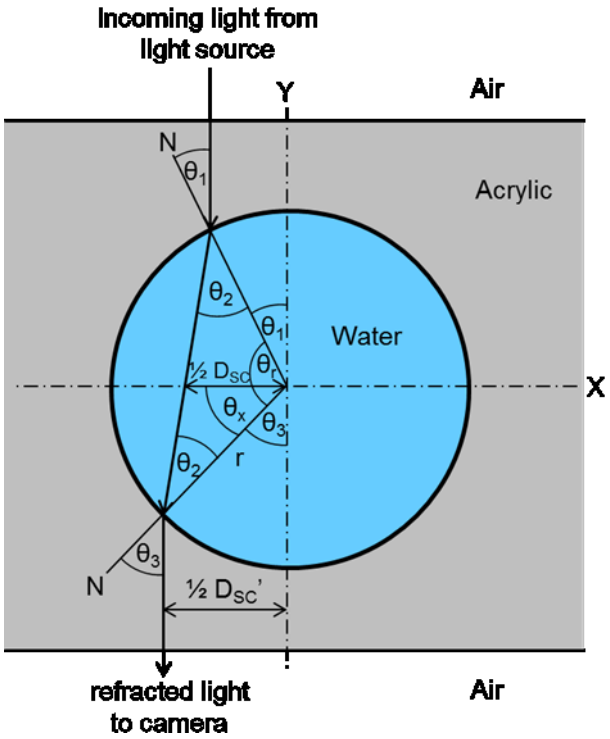

Figure 3.16 Schematic of light refraction in the nozzle
(view from top - nozzle horizontal cross sectional area)

Figure 3.17 shows the string cavitation diameter ratio D_{SC}^* for $Z/D \leq 3$ and $W_U/D = 7.5$. The result clearly shows that string cavitation diameter does not strongly depend on mean flow velocity V, which is the reason of the constant discharge coefficient C_d. As shown in the figure, smaller lift Z/D results in larger string cavitation diameter ratio due to the larger lateral inflow velocity and the resulting larger angular velocity in the nozzle hole, which is the reason of the extremely small C_d and large spray angle θ.

As explained above, at the boundary regime of Z/D = 3 string cavitation is not steady. Judging from thousands of photos, the probability of string cavitation occurrence for different needle lifts is obtained and this is plotted against mean flow velocity V in Figure 3.18. The string cavitation occurrence probability for $Z/D \leq 2$ switches from almost zero to almost one at the minimum velocity of string cavitation formation. On the other hand, in the case of Z/D = 3, it gradually increases from zero to one as mean flow velocity V increases. When it lies between zero and one, flow pattern in the injector and the nozzle hole is unsteady due to the instability of the swirling flow in the upstream channel.

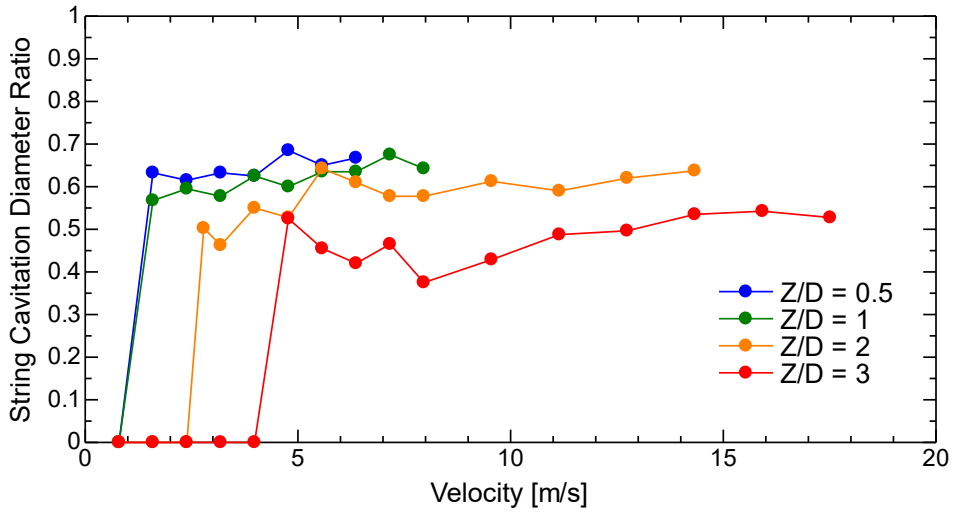

Figure 3.17 Mean flow velocity V versus string cavitation diameter ratio D_{SC}/D at wide upper-volume ($W_U/D = 7.5$)

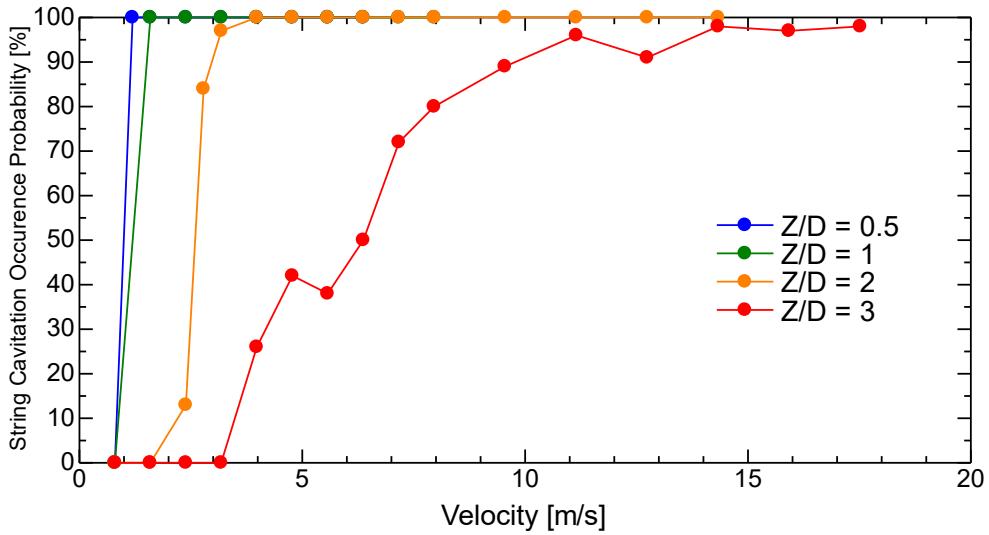

Figure 3.18 Mean flow velocity V versus string cavitation occurrence probability at wide upper-volume ($W_U/D = 7.5$)

3.4.4 High Speed Imaging Results

Figure 3.19 shows a sequence of thin string cavitation formation at transition regime of Z/D = 3, $W_U/D = 7.5$ and V = 8.0 m/s. As shown in the images, a thin string cavitation starts to appear not from the exit of the nozzle hole but within the upper part of the nozzle hole. It extends, then gradually shrank and finally disappeared in the nozzle hole after about 5 ms from its formation. The motion indicates that thin string cavitation does not consist of ambient air. It should be noted that a thick cavitation shown in Figure 3.7 is often observed and the thin string cavitation is rarely observed in the case.

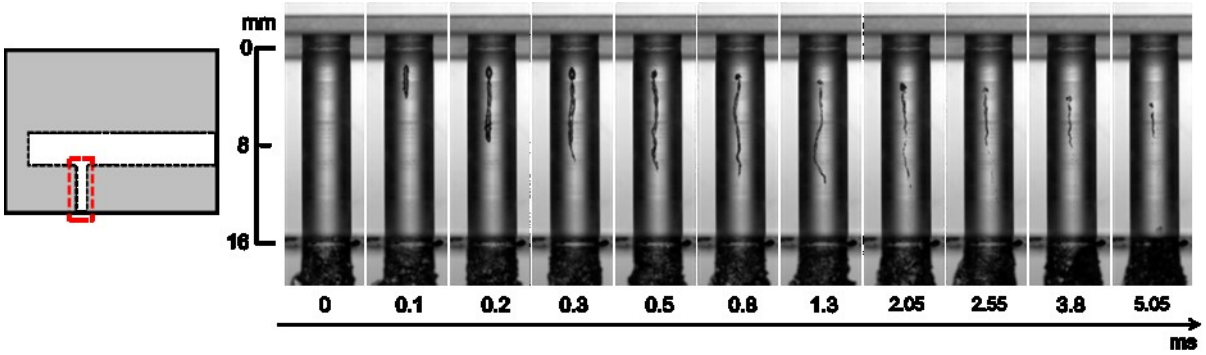

Figure 3.19 Formation of thin string cavitation (W_U/D = 7.5, Z/D = 3, V = 8.0 m/s)

Figure 3.20 shows an example of the formation process of a thick string cavitation. At time t = 0 ms, a thin and slanted string cavitation is seen from the inlet of nozzle hole to the middle of the nozzle hole. At t = 1.0 ms, a thick cavitation string flows in from the nozzle exit, and it follows the thin string cavitation and spreads upstream. Once a thin string cavitation is replaced by a thick string cavitation, the liquid flow rate is decreased and it takes a long time until it starts to shrink and disappear. The result indicates the stability of the thick string cavitation.

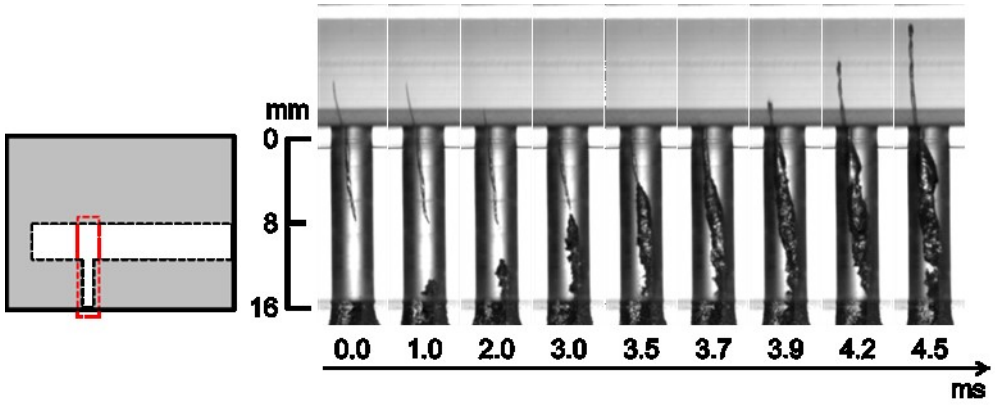

Figure 3.20 Formation of thick string cavitation (W_U/D = 7.5, Z/D = 3, V = 8.0 m/s)

Figure 3.21 shows the sequence of string cavitation disappearance. As shown in the figure, at t = 0 ms a thick string cavitation is seen. At t = 2.0 ms RIC appears near the right inlet of the nozzle hole probably due to the transition from the swirling flow to contraction flow in the upstream channel and soon starts to extend downstream while the string cavitation flows out of the nozzle hole at t = 4.5 ms. It usually takes a long time (about 20 ms) until string cavitation completely disappears.

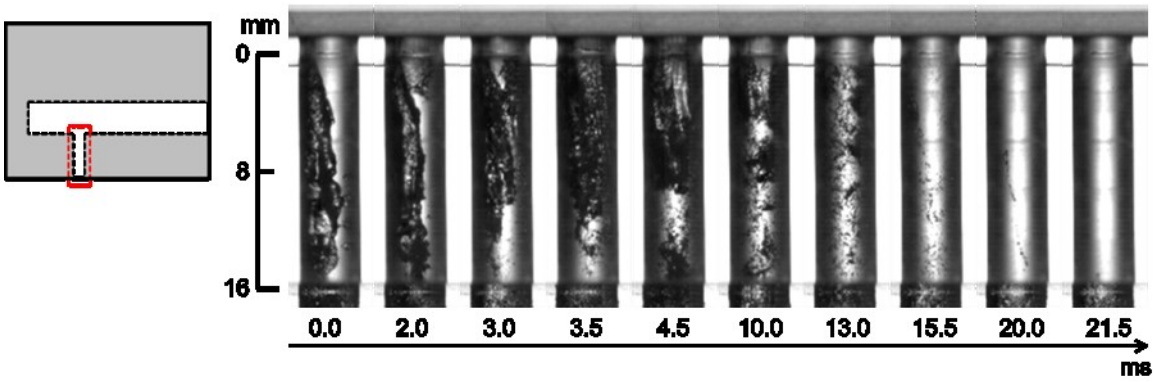

Figure 3.21 Collapse of thick string cavitation (W_U/D = 7.5, Z/D = 3, V = 8.0 m/s)

The effect of thick string cavitation on discharged liquid jet can be clearly seen in Figure 3.22. When a thick string cavitation starts to flow in from the nozzle exit (t = 50 ms), the liquid jet angle becomes widest due to the formation of the strongest helical flow in the nozzle hole and the swirling liquid skirt. When the thick string cavitation occupies the nozzle hole (t = 55 ms), liquid flow rate decreases by the decrease in the effective flow area in the nozzle hole and that in discharge coefficient, which then decreases the jet angle. These drastic and unpredictable changes of the cavitation and the liquid jet characteristics at transition regime of Z/D = 3 have to be avoided to control fuel spray characteristics.

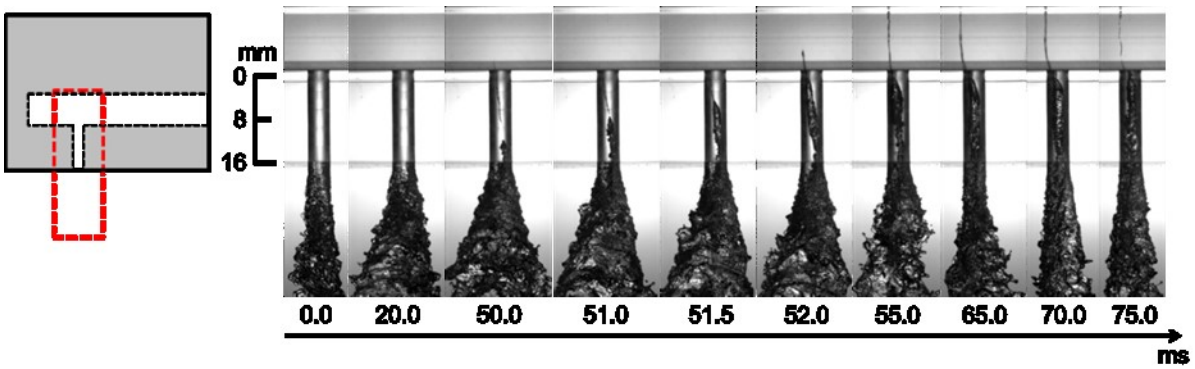

Figure 3.22 String cavitation formation and the jets (W_U/D = 7.5, Z/D = 3, V = 8.0 m/s)

3.4.5 Numerical Results

Figure 3.23 and Figure 3.24 show the simulated streamline in the injector and the velocity distribution on the horizontal plane 1 mm above the nozzle hole inlet in the nozzle hole upstream for low needle lift of Z/D = 2 and high needle lift of Z/D = 4, respectively. Figure 3.23 (a) clearly shows the formation of swirling flow in the upstream channel, and Figure 3.24 (a) tells the strong angular velocity at the low needle lift of Z/D = 2. On the other hand, the swirling flow is very weak for high needle lift Z/D = 4, as shown in Figure 3.24 (b). Figure 3.25 (a) and (b) show the simulated pressure distributions at the vertical cross section for Z/D = 2 and 4, respectively. As shown in Figure 3.25 (a), a slanted low-pressure region is observed upstream of the nozzle hole with Z/D = 2, which agrees with the position of the

slanted string cavitation formation. On the other hand for high lift of Z/D = 4 pressure in the upstream channel is so high that no string cavitation occurs. These numerical results confirm that the swirling flow in the upstream channel and the resulting string cavitation can be caused by the sudden conversion from the lateral momentum to the axial momentum in a narrow space at low needle lift even in the completely symmetric nozzle in the depth direction.

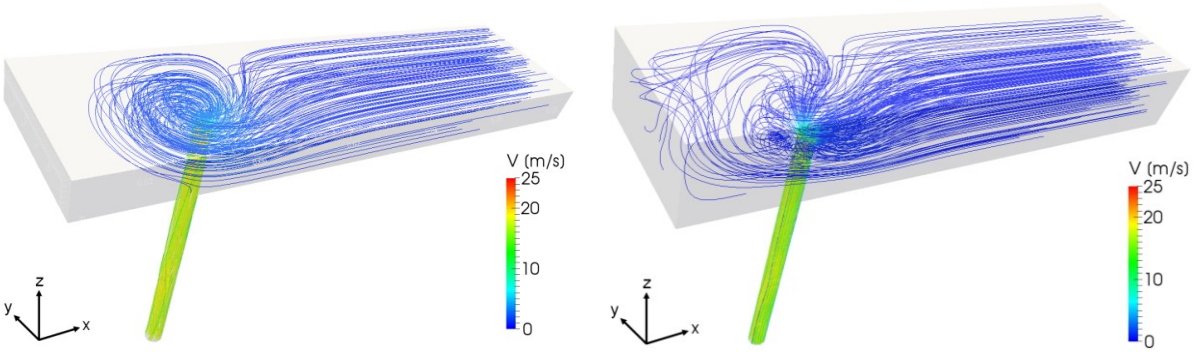

(a) Z/D = 2 (b) Z/D = 4

Figure 3.23 Streamline in the upstream channel (W_U/D = 7.5, V = 17.0 m/s)

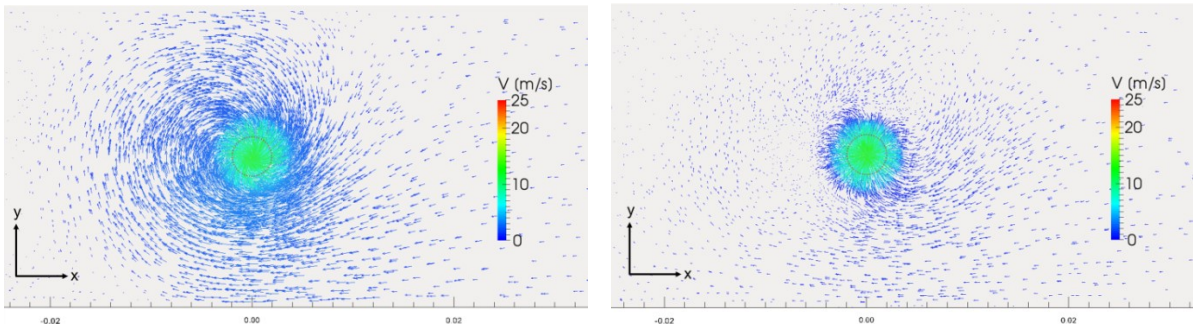

(a) Z/D = 2 (b) Z/D = 4

Figure 3.24 Velocity distribution on the upstream horizontal plane (1 mm above the nozzle hole inlet, W_U/D = 7.5, V = 17.0 m/s)

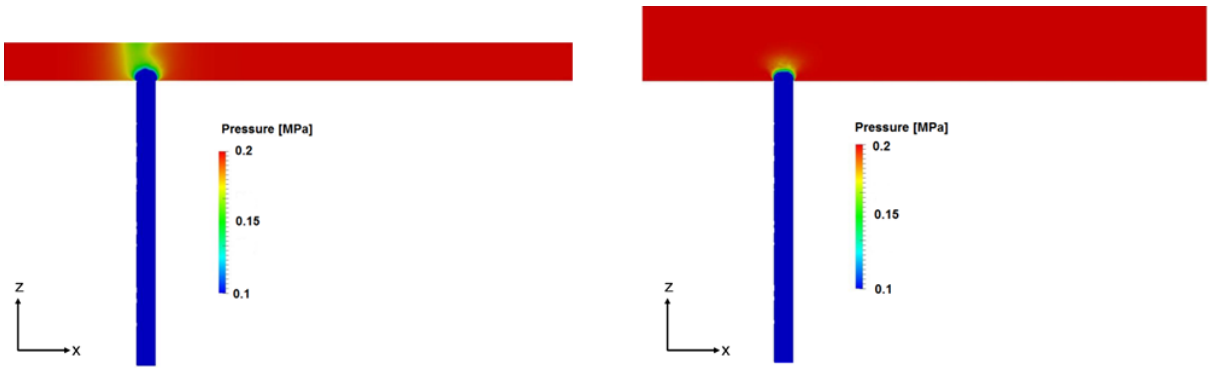

(a) Z/D = 2 (b) Z/D = 4

Figure 3.25 Pressure distribution on the vertical cross section across the nozzle center (W_U/D = 7.5, V = 17.0 m/s)

3.5 Summary

Visualization of cavitation inside scale-up nozzles of 4 mm in hole diameter with an asymmetric inflow at various needle lifts was carried out in the present study. As a result, the following conclusions were obtained:

1. It was confirmed that the formation of the thick string cavitation and the resulting swirling hollow cone liquid skirt and decrease in discharge coefficient at low needle lift ($Z/D \leq 3$ for $W_U/D = 7.5$ and $Z/D \leq 1$ for $W_U/D = 3.75$).
2. On the other hand, at high needle lift string cavitation is never observed even at high flow rate and the boundary between low lift with string cavitation and high lift with no string cavitation does not depend on liquid flow rate. Note that special attention needs to be paid when we use a multi-hole fuel injector at middle needle lift, which may result in occasional string cavitation and occasional hollow cone liquid skirt.
3. At narrow upper-volume of $W_U/D = 3.75$, which represents the case with a large nozzle-hole number, the swirling flow in the upstream channel and the resulting string cavitation only appears at very low needle lift of $Z/D \leq 1$ due to the limitation in the upstream space.
4. Numerical simulation was also conducted to examine the flow pattern and pressure distribution at low needle lift ($Z/D = 2$) and high needle lift ($Z/D = 4$) for wide upper-volume of $W_U/D = 7.5$. The results show a good agreement with the experiment results that swirling inflow was obtained at low lift of $Z/D = 2$ which leads to a slanted string cavitation.
5. These results conclude that thick string cavitation and the resulting hollow cone liquid skirt can be initiated by the conversion from the large lateral inflow momentum to the axial momentum in the nozzle hole within a narrow space at low needle lift even if the structure of the injector is very simple. The condition of the string cavitation formation can be estimated by simply knowing the lateral inflow momentum, needle lift and upstream channel width.

Chapter 4
Cavitation in Two-Dimensional Mini-Sac Nozzle

4.1 Introduction

Figure 4.1 (a) represents the schematic of a multi-hole mini-sac nozzle. Mini-sac nozzle has asymmetric inflow characteristic with more complicated geometry than the VCO nozzle. In mini-sac nozzles, nozzle holes are located at various positions in the sac with various nozzle angles. In the injector designing process, needle angle is varied. The needle moves to control the fuel injection into the combustion chamber. Although these nozzle shape factors affect cavitation and the injected liquid jet, their effects have not been understood yet. Since cavitation structure in 3D nozzles is complicated and difficult to be captured and measured quantitatively, in this study cavitation in simple 2D nozzles with a sac shown in Figure 4.1 (b) is investigated. The needle angle, the needle lift, and the nozzle angle were varied to understand their effects on cavitation and the injected liquid jets. Injection pressure is varied to observe the cavitation pattern under various mean flow velocities V in the nozzle. Particle image velocimetry (PIV) analysis is carried out to examine the flow pattern near the nozzle inlet and the nozzle exit as well as the turbulence intensity in the sac with various needle angles, needle lifts, and nozzle angles.

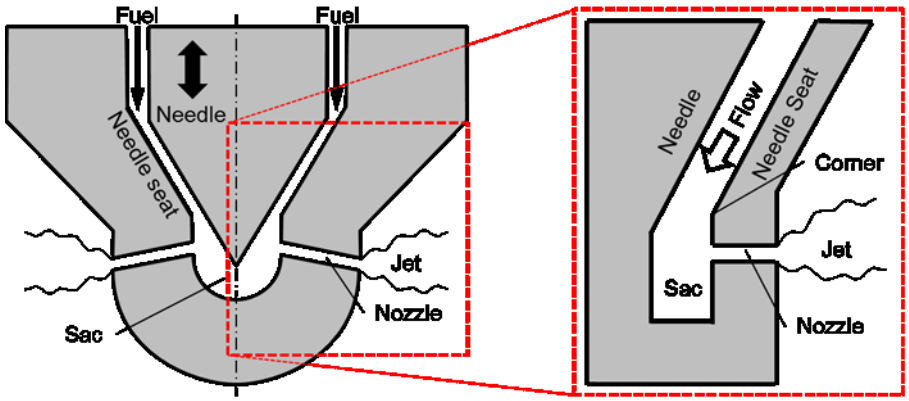

(a) Mini-sac nozzle (b) Model

Figure 4.1 Schematic of Mini-sac nozzle and its model

4.2 Experimental Setup

Figure 4.2 shows the schematic of experimental apparatus. Filtered tap water at 30±0.5 ºC in temperature was injected into the ambient air through various 2D mini-sac model nozzles. The injected liquid flow rate was measured by a flow meter (Keyence FD-SS20A). Still images of cavitation and a liquid jet were captured using a digital camera (Nikon D800) and a flash lamp as a backlight (Nisshindenki Co., Micro Flash Stroboscope, MS-1000/LH-15M, 2-4 μs in duration). High-speed images of cavitation for PIV analysis were taken using a high-speed camera (Photron FASTCAM SA-X2) and a metal-halide lamp (Kyowa Co. Ltd.,

MID-25FC). A diffuser was placed between the nozzle and backlight source to evenly distribute the light into the camera sensor.

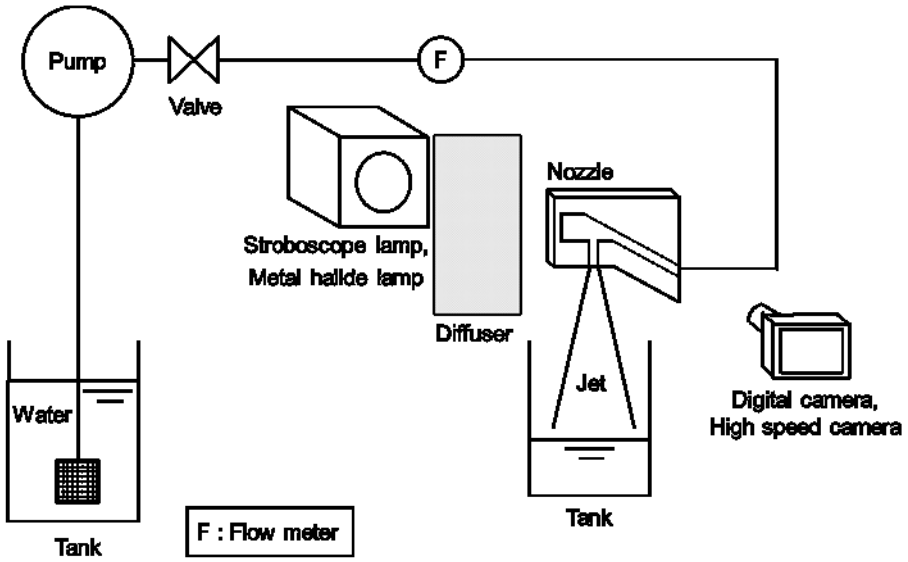

Figure 4.2 Schematic of experimental apparatus

Eight simplified 2D nozzles were manufactured with various needle angles θ_{Ne}, needle lifts S, and nozzle angles $\theta_{N,}$ as shown in Figure 4.3. The nozzle consists of stainless steel thin flat plates to form the side walls and front and back plates made of transparent acrylic plates. The width W, length L and thickness of the nozzles are 4.0 mm, 16.0 mm, and 1.0 mm, respectively (L/W = 4.0). The distance between the sac inlet corner and the nozzle inlet corner L_{SN} is 8.0 mm (L_{SN}/W = 2.0). The sac depth H_S and sac radius R_S are 28.0 mm and 16.0 mm, respectively (H_S/W = 7.0, R_S/W = 4.0). The inlet edges of the nozzles were made to be sharp whose radius R of the curvature is less than 30 micrometers (R/W < 1%). The three nozzles shown in the first set of the nozzles shown in Figure 4.3 (d), (b) and (c) have small needle angle (θ_{Ne} = 30º), medium needle angle (θ_{Ne} = 40º) and large needle angle (θ_{Ne} = 60º), respectively. Figure 4.3 (d), (e) and (f) have low needle lift (clearance S between the seat and the needle is 4.0 mm, S/W = 1), medium needle lift (S/W = 2) and high needle lift (S/W = 3), respectively. The other set of the nozzles shown in Figure 4.3 (d), (g) and (h) have large nozzle angle (θ_N = 90º), medium nozzle angle (θ_N = 65º) and small nozzle angle (θ_N = 35º), respectively. Note that the effective lengths of the slanted nozzles are L/sinθ_N. Table 4.1 (a) summarizes the principal dimensions of the nozzles.

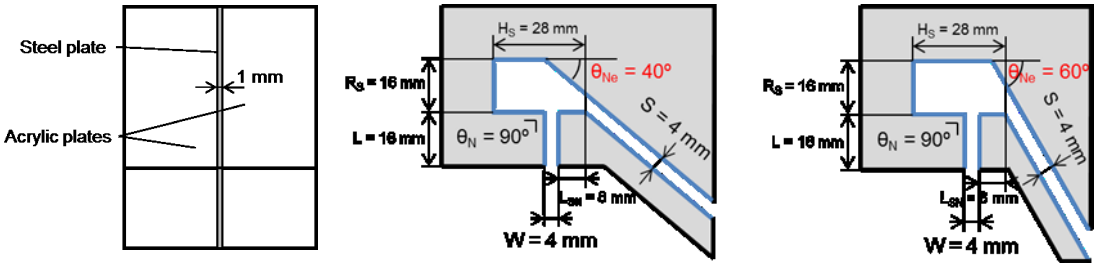

(a) Side view (b) Nozzle θ_{Ne}40 (S/W = 1, θ_N = 90º) (c) Nozzle θ_{Ne}60 (S/W = 1, θ_N = 90º)

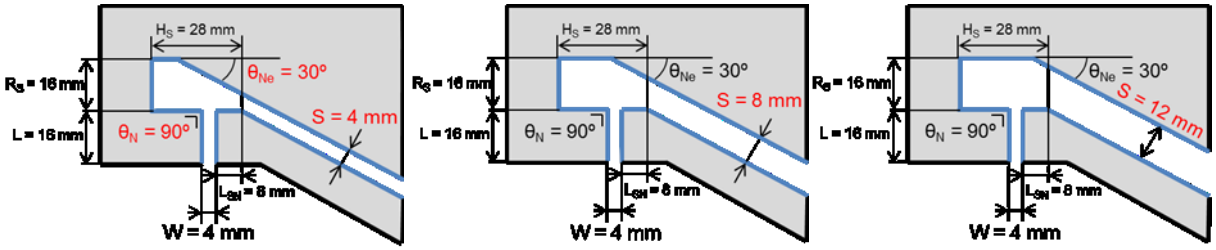

(d) Nozzle θ_{Ne}30, S1, θ_N90 (e) Nozzle S2 (θ_{Ne} = 30º, θ_N = 90º) (f) Nozzle S3 (θ_{Ne} = 30º, θ_N = 90º)

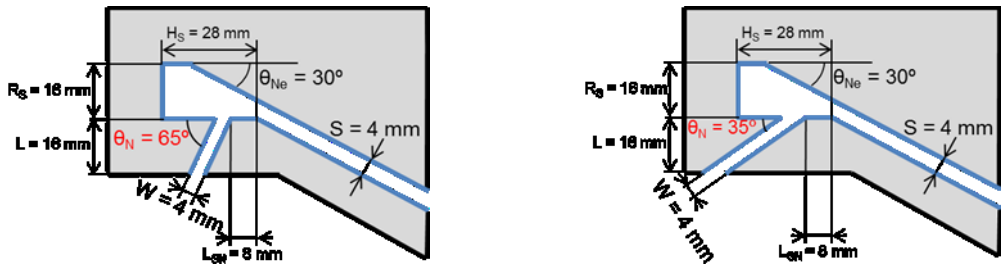

(g) Nozzle θ_N65 (S/W = 1, θ_{Ne} = 30º) (h) Nozzle θ_N35 (S/W = 1, θ_{Ne} = 30º)

Figure 4.3 Mini-sac model nozzles for various needle angle, needle lift, and nozzle angle

Additional eight simplified 2D nozzles were manufactured with various corner distance L_{SN}, sac depth H_S, and sac radius R_S, as shown in Figure 4.4. The width W, length L and thickness of the nozzles are same with the previous eight nozzles, i.e. 4.0 mm, 16.0 mm, and 1.0 mm, respectively. The needle lift S is 4.0 mm (S/W = 1.0). The needle angle θ_{Ne} and nozzle angle θ_N are 30º and 90º, respectively. The three nozzles shown in the first set of the nozzles as shown in Figure 4.4 (b), (c) and (d) have short corner distance (L_{SN}/W = 1.0), medium corner distance (L_{SN}/W = 2.0) and long corner distance (L_{SN}/W = 3.0), respectively. Figure 4.4 (d), (e) and (f) have deep sac (H_S/W = 7), medium sac depth (H_S/W = 6) and shallow sac (H_S/W = 5), respectively. The other set of the nozzles shown in Figure 4.4 (d), (g) and (h) have large sac radius (R_S/W = 4), medium sac radius (R_S/W = 3) and small sac radius (R_S/W = 2), respectively. Note that for R_S/W = 3 and 2, L_{SN}/W is 2.0, while for R_S/W = 4, L_{SN}/W is 3.0. Table 4.1 (b) summarizes the principal dimensions of the nozzles.

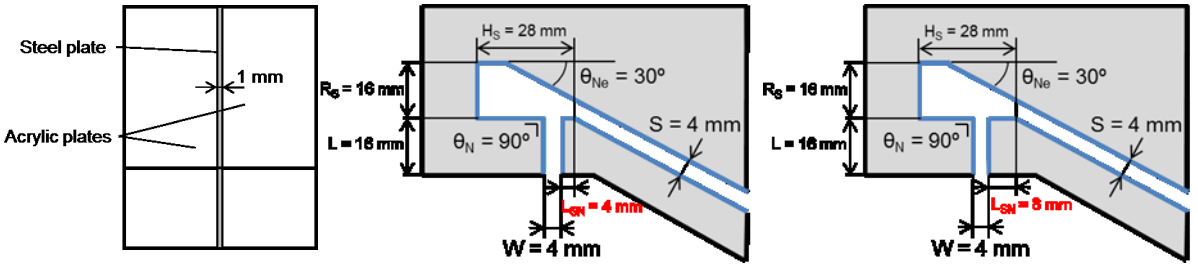

(a) Side view (b) Nozzle $L_{SN}1$ ($R_S/W = 4$, $H_S/W = 7$) (c) Nozzle $L_{SN}2$ ($R_S/W = 4$, $H_S/W = 7$)

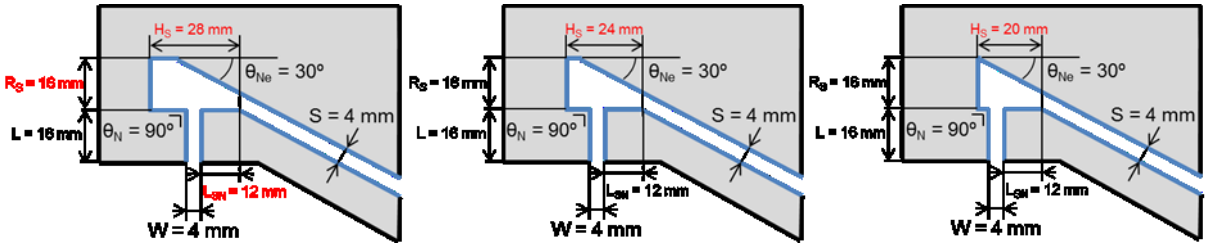

(d) Nozzle $L_{SN}3$, R_S4, H_S7 (e) Nozzle H_S6 ($L_{SN}/W = 3$, $R_S/W = 4$) (f) Nozzle H_S5 ($L_{SN}/W = 3$, $R_S/W = 4$)

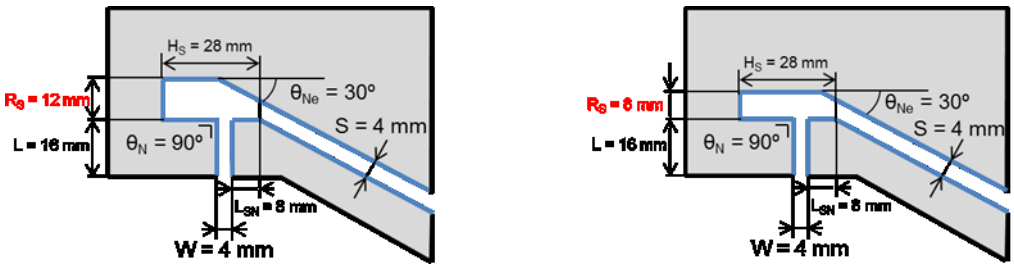

(g) Nozzle R_S3 ($L_{SN}/W = 2$, $H_S/W = 7$) (h) Nozzle R_S2 ($L_{SN}/W = 2$, $H_S/W = 7$)

Figure 4.4 Mini-sac model nozzles for various Needle seat corner to nozzle edge distance, sac depth, and sac radius

Table 4.1 Dimensions of the 2D mini-sac nozzles

(a) Needle angle, needle lift, nozzle angle

Nozzle	L [mm]	W [mm]	L_{SN} [mm]	H_S [mm]	R_S [mm]	S [mm]	θ_{Ne} [°]	S/W	θ_N [°]
$\theta_{Ne}40$	16.0	4.0	8.0	28.0	16.0	4.0	40	1.0	90
$\theta_{Ne}60$						4.0	60	1.0	90
$\theta_{Ne}30$, S1, θ_N90						4.0	30	1.0	90
S2						8.0	30	2.0	90
S3						12.0	30	3.0	90
θ_N65						4.0	30	1.0	65
θ_N35						4.0	30	1.0	35

(b) Needle seat corner to nozzle edge distance, sac depth, sac radius

Nozzle	L [mm]	W [mm]	L_{SN} [mm]	H_S [mm]	R_S [mm]	S [mm]	θ_{Ne} [º]	θ_N [º]	L_{SN}/W	H_S/W	R_S/W
$L_{SN}1$	16.0	4.0	8.0	28.0	16.0	4.0	30	90	1.0	7.0	4.0
$L_{SN}2$			8.0	28.0	16.0				2.0	7.0	4.0
$L_{SN}3$, R_S4, H_S7			12.0	28.0	16.0				3.0	7.0	4.0
H_S6			12.0	24.0	16.0				3.0	6.0	4.0
H_S5			12.0	20.0	16.0				3.0	5.0	4.0
R_S3			8.0	28.0	12.0				2.0	7.0	3.0
R_S2			8.0	28.0	8.0				2.0	7.0	2.0

Tracer particles with 25 µm and 113 µm in mean diameter and 1,030 kg/m^3 in density were introduced into the water for particle image velocimetry (PIV) analysis to measure the sac flow field, the nozzle inflow field, and the flow pattern near the nozzle exit. The captured size region for the sac part was approximately 32.0 mm in width and 17.3 mm in height with 768 × 416 pixels, respectively, and 40,000 fps in frame rate, so that the spatial resolution is 42 µm/pixel and the time interval between a pair of the PIV images is 25 µs. The width and the height of measured region upstream of the nozzle, which is called as pitch part, were approximately 8.5 × 3.5 mm with 512 × 208 pixels, respectively, and 100,000 fps in frame rate, so that the spatial resolution is 17 µm/pixel and time interval between a pair of the PIV images is 10 µs. The width and the height of the measured region of the nozzle inlet were approximately 6.7 and 3.6 mm with 384 and 208 pixels, respectively, and 120,000 fps in frame rate, so that the spatial resolution is 17 µm/pixel and the time interval between a pair of the PIV images is 8.3 µs. For the nozzle exit PIV, the size of the captured region was approximately 2.0 × 3.5 mm, which was captured with 128 × 216 pixels and frame rate of 150,000 fps, so that the spatial resolution is 16 µm/pixel and the time interval between a pair of the PIV images is 6.7 µs. The interrogation window size is 15 × 15 pixels, and the search window is 31 × 31 pixels in the PIV analysis which were set after the sensitivity analysis. The PIV setup is summarized in Table 4.2.

Table 4.2 PIV Setup

Analyzed Region	Captured Size [mm]	Captured Size [Pixel]	Spatial Resolution [µm/pixel]	Tracer Particle Size [µm]	Tracer Particle Mean Diameter [µm]	Interrogation Window [pixel]	Search Window [pixel]	Time Interval [µs]
Sac	32.0 × 17.3	768 × 416	42	75-150	113	15 × 15	31 × 31	25
Pitch	8.5 × 3.5	512 × 208	17	20-30	25			10
Nozzle Inlet	6.7 × 3.5	384 × 208	17					8.3
Nozzle Outlet	2.0 × 3.5	128 × 216	16					6.7

4.3 Results and Discussion

Figure 4.5 (a) shows images of cavitation and the injected liquid jets near the nozzle at various needle angles θ_{Ne}. Cavitation inception occurs near the right inlet edge. It extends downstream as mean velocity V increases, and reaches almost to the exit, which is called super cavitation [24], [75]. Further increase in V results in the imperfect hydraulic flip (IHF) [44], at which a cavitation sheet reaches the exit and ambient air flows up into the tail of cavitation. The length L_C of the cavitation along the right wall decreases with increasing needle angle θ_{Ne} and under constant V condition. Cavitation is thicker and larger cavitation clouds are shed near the tail of the super cavitation sheet at smaller needle angle θ_{Ne}. The liquid jet deforms asymmetrically due to the asymmetric cavitation. The left interface of the jet is almost straight without spreading outward. The right interface deforms largely especially at super cavitation with small needle angle (θ_{Ne} = 30º) due to the thick cavitation along the right wall reaching near the exit and does not deform largely at the imperfect hydraulic flip. The jet is slanted toward the right. The liquid interface velocity at the left side is larger than that at the right side.

Figure 4.5 (b) shows images of cavitation and the jet at various needle lift. Cavitation appears along the right wall at every needle lift case but note that a small cavitation also occurs at the left inlet at S/W = 2 and 3. Cavitation at lower needle lift develops at lower mean velocity V than that at higher needle lift. At V = 14.0 m/s, for example, even in the same mean velocity, cavitation at S/W = 1 reaches the middle of the nozzle while at S/W = 3 it just starts to develop after its inception. The liquid jet deformation on the right side is clearly observed at low needle lift S/W = 1. In the case of higher needle lift, i.e. S/W = 2 & 3, the jet is slightly deformed when the cavitation length reaches the middle of nozzle length and is suppressed when it turns to IHF. Note that the small cavitation occurring on the left side of nozzle inlet at S/W = 2 and 3 does not affect the left side jet deformation.

Figure 4.5 (c) shows images of cavitation with the jet at various nozzle angle θ_N. Cavitation appears along the right wall at θ_N = 90º. At θ_N = 65º, cavitation appears at the right and left sides with a cloudy cavitation structure for the left and a film cavitation structure for the right. Cavitation appears and develops only from the acute left inlet edge for θ_N = 35º. At θ_N = 90º, the cavitation film thickness is as thick as half of the nozzle width W due to the major inflow from the right. Smaller θ_N results in a thinner film cavitation which results in smaller contraction coefficient and shorter cavitation under constant V condition. For θ_N = 90º the liquid jet angle θ_J increases at super cavitation (V = 16.0 m/s). However for θ_N = 35º and 65º, the liquid jet angle θ_J increases only slightly even under high V and long cavitation condition.

Figure 4.5 (d) shows images of cavitation with the jet at various needle corner to nozzle inlet distance L_{SN}. Cavitation appears along the right wall at every case and the jet widen to the right side by the increase of mean velocity V. The cavitation development happens at lower velocity V for shorter distance of L_{SN} that at same velocity V, the cavitation at shorter distance L_{SN} is longer than the longer L_{SN}. The jet is deformed at super cavitation and is suppressed when it turns to IHF.

Figure 4.5 (e) shows images of cavitation with the jet at various sac depth H_S/W. Cavitation appears along the right nozzle wall at every case and the jet occurs asymmetrically to the right side by the increase of mean velocity V. The cavitation and jet deformation show a similar result for every sac depth cases that the cavitation length is almost same at same velocity V, as well as the liquid jet angle. Same with another case, the jet is deformed at super cavitation and is suppressed when it turns to IHF.

Figure 4.5 (f) shows images of cavitation with the jet at various sac radius R_S/W. The cavitation and jet deformation phenomena show the same tendency with the other cases, that cavitation appears along the right nozzle wall and the jet occurs asymmetrically to the right side by the increase of mean velocity V, and the jet is deformed at super cavitation and is suppressed when it turns to IHF.

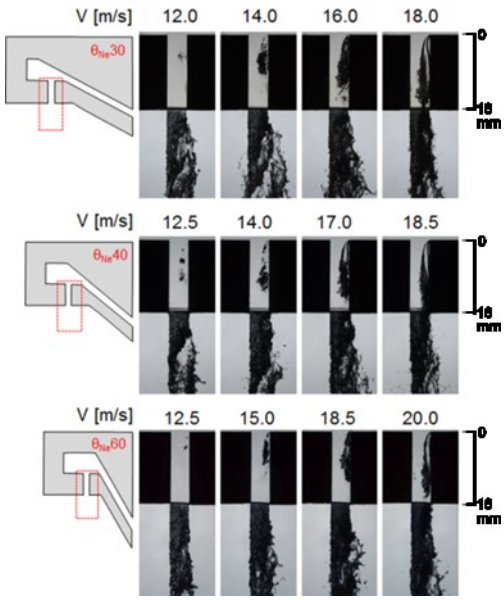

(a) Effect of θ_{Ne}

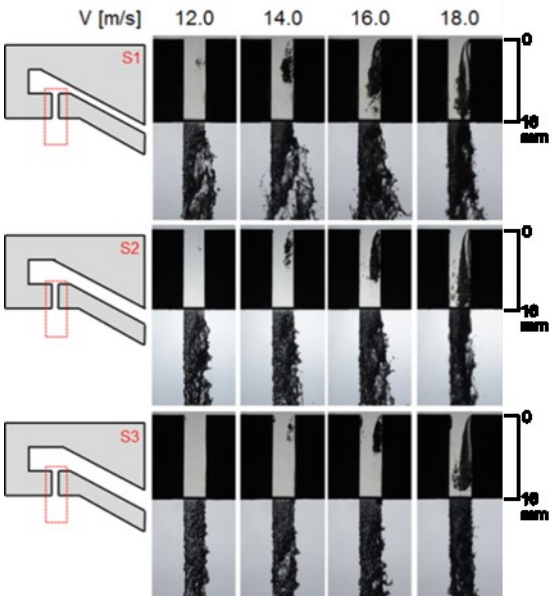

(b) Effect of S/W

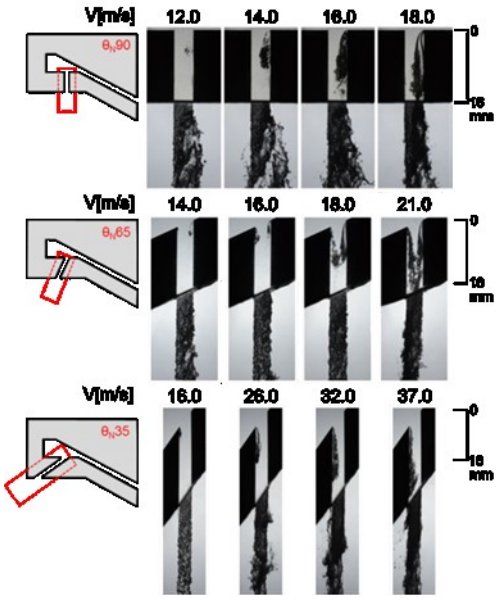

(c) Effect of θ_N

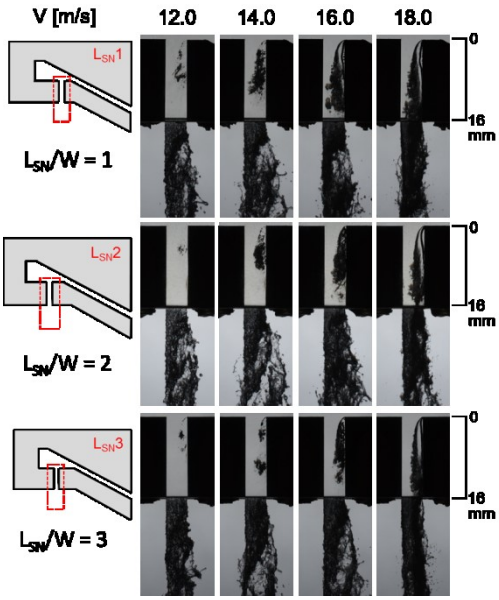

(d) Effect of L_{SN}

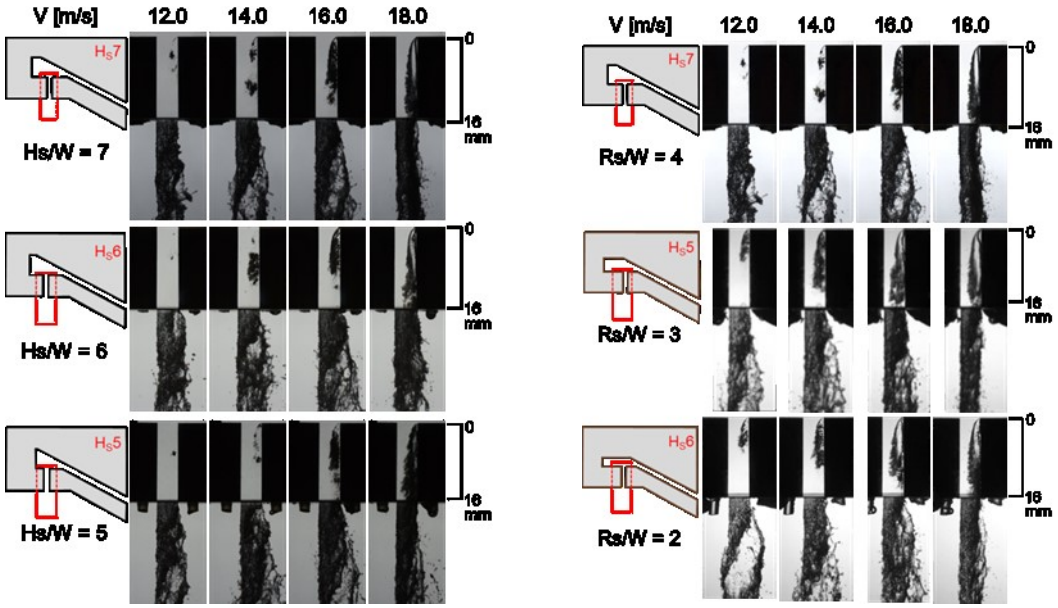

(e) Effect of H_S/W (f) Effect of R_S/W

Figure 4.5 Cavitation in mini-sac nozzle with various nozzle geometry parameters, and mean velocities V

The length of cavitation L_C along the right wall at θ_{Ne} = 30º, 40º and 60º which is normalized by the nozzle length L and its standard deviation are plotted against the mean velocities V in Figure 4.6 (a). The length of cavitation L_C along the right wall at S/W = 1, 2 and 3 which is normalized by the nozzle length L and its standard deviation are plotted against the mean velocities V in Figure 4.6 (b), while the length of cavitation along the right wall L_{CR} at θ_N = 65º and 90º, as well as that along the left wall L_{CL} at θ_N = 35º which are normalized by the actual nozzle length $L/\sin\theta_N$ and its standard deviation, are plotted against V in Figure 4.6 (c). As we can see in Figure 4.6 (a), small and medium needle angles (θ_{Ne} = 30º, 40º) show similar results, however, medium needle angle has a larger fluctuation in L_C and the hydraulic flip occurs at higher V. Large needle angle (θ_{Ne} = 60º) clearly results in a shorter L_C and its larger fluctuation. For needle lift case, the trend lines are very similar for every needle lift where the lower needle lift appears at lower mean velocity than the higher needle lift as shown in Figure 4.6 (b). As shown in Figure 4.6 (c), small θ_N clearly results in a shorter L_C. Note that hydraulic flip does not occur at θ_N = 35º even at very high V of 37.5 m/s. Figure 4.6 (d) shows the length of cavitation L_C along the right wall at L_{SN}/W = 1, 2 and 3, which is normalized by the nozzle length L and its standard deviation are plotted against the mean velocities V, while Figure 4.6 (e) shows that of H_S/W = 7, 6 and 5, and Figure 4.6 (f) shows that of R_S/W = 4, 3 and 2. As shown in Figure 4.6 (d) for needle corner to nozzle inlet distance L_{SN} case, the trend lines are very similar for every L_{SN}/W where the smaller L_{SN}/W appears at slightly lower mean velocity than the larger L_{SN}/W. For sac depth case, as shown in Figure 4.6 (e), cavitation develops at almost same mean velocity V, but for H_S/W = 7, cavitation occurs at slightly higher mean velocity V. The similar result is obtained for the sac radius case, as shown in Figure 4.6 (f), that cavitation develops at almost same mean velocity V, but for R_S/W = 4, cavitation occurs at slightly higher mean velocity V.

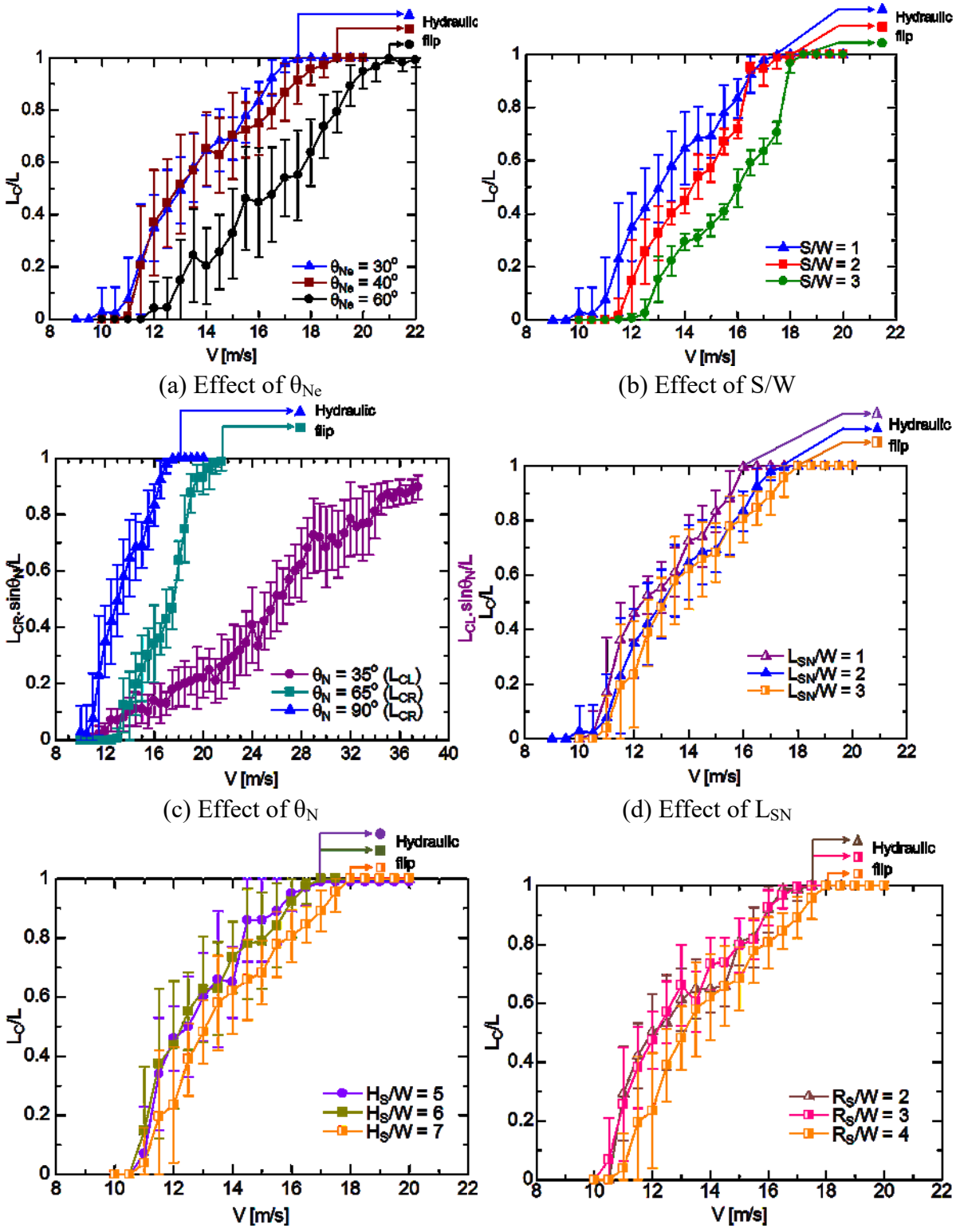

(a) Effect of θ_{Ne} (b) Effect of S/W

(c) Effect of θ_N (d) Effect of L_{SN}

(e) Effect of H_S/W (f) Effect of R_S/W

Figure 4.6 Cavitation length ratio L_C/L versus mean velocity V with its standard deviation at various nozzle geometry parameters

Figure 4.7 shows measured jet angle θ and its standard deviation. Jet angle θ is defined at one nozzle length downstream from the nozzle exit. The angle θ increases as mean velocity

V increases unless imperfect hydraulic flip is formed [76]. When imperfect hydraulic flip occurs, jet angle θ decreases with increase in V. For the nozzles with smaller needle angle θ_{Ne}, lower needle lift S/W and larger nozzle angle θ_N, jet angles θ are larger. It is known that the thicker cavitation induces larger cavitation vortex shedding, which leads to a larger jet deformation and results in a wider jet angle [76], which will be discussed later in this chapter.

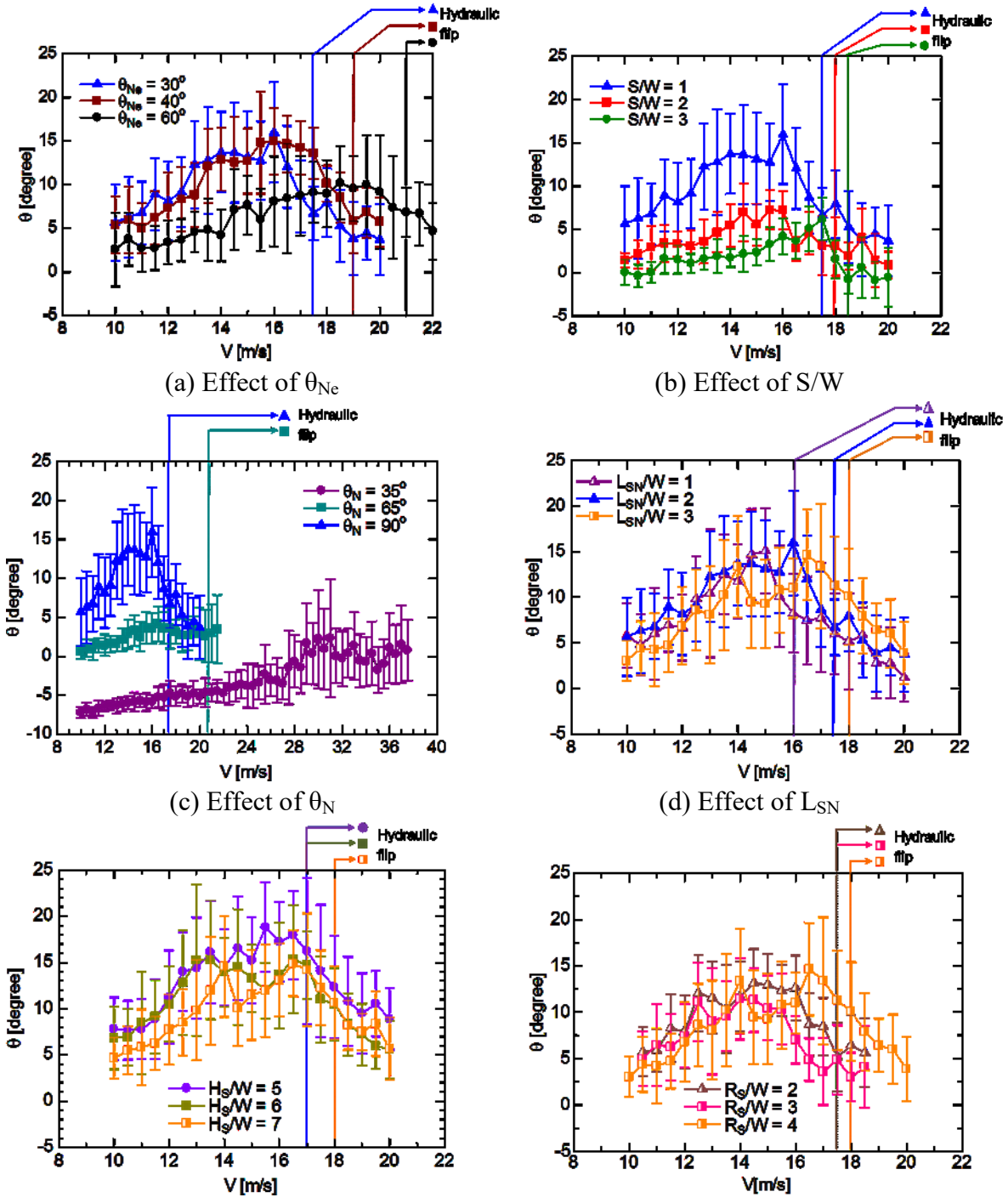

(a) Effect of θ_{Ne} (b) Effect of S/W

(c) Effect of θ_N (d) Effect of L_{SN}

(e) Effect of H_S/W (f) Effect of R_S/W

Figure 4.7 Jet angle θ versus mean velocity V with its standard deviation at various nozzle geometry parameters

The thickness of cavitation W_C at super cavitation is measured at various downward positions y from the nozzle inlet using image analysis. Figure 4.8 (a), (b), (c), (d), (e), and (f) show the right cavitation thickness ratio W_C/W with various needle angles θ_{Ne}, needle lifts S/W, nozzle angles θ_N, needle seat corner to nozzle inlet distance L_{SN}, sac depth H_S, and sac radius R_S, respectively. In the case of nozzle angle $\theta_N = 35°$, film cavitation structure occurs along the left wall, and left cavitation thickness ratio W_{CL}/W was measured. The figures clearly show that the nozzles with smaller needle angle θ_{Ne}, smaller needle lift S/W, larger nozzle angle θ_N, shorter distance between needle seat corner to nozzle inlet distance L_{SN}, shallow sac depth H_S, and smaller sac radius R_S result in a thicker cavitation due to the larger lateral inflow velocity at the nozzle inlet, which leads to smaller contraction coefficient C_C, longer cavitation length L_C/L and larger jet angle θ. Note that in the case of sac radius, the smaller sac radius ($R_S/W = 2$ & 3) has an obvious thicker cavitation than the larger sac radius ($R_S/W = 4$) because the needle seat corner to nozzle inlet distances for these nozzles are shorter ($L_{SN}/W = 2$).

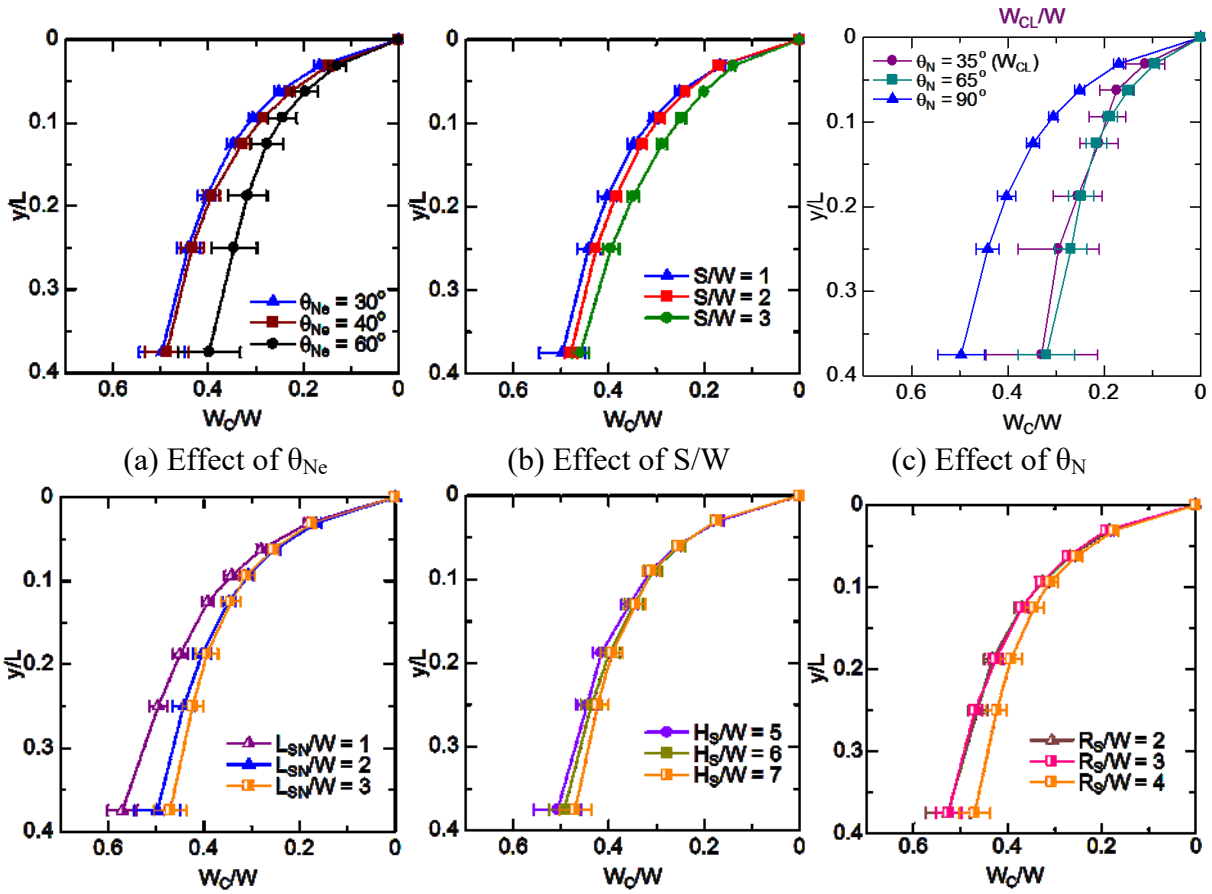

(a) Effect of θ_{Ne} (b) Effect of S/W (c) Effect of θ_N

(d) Effect of L_{SN} (e) Effect of H_S/W (f) Effect of R_S/W

Figure 4.8 Cavitation thickness ratio W_C/W with its standard deviation at super cavitation at various nozzle geometry parameters

Figure 4.9 (a) and (b) show the velocity field near the nozzle inlet area for $\theta_{Ne} = 30°$ and 60°, respectively, and the liquid velocities V for both cases are 15.0 m/s. The velocity fields

are the average of 100 velocity fields obtained by PIV analysis. The result shows that the lateral inflow velocity component at the right inlet edge for θ_{Ne} = 30º is clearly larger than that for θ_{Ne} = 60º since the needle valve for smaller θ_{Ne} decreases the thickness of the separated boundary layer formed downstream of the sac inlet. The larger lateral inflow explains why cavitation at θ_{Ne} = 30º is thicker, which decreases static pressure at vena contracta and increases cavitation length, than that at θ_{Ne} = 60º.

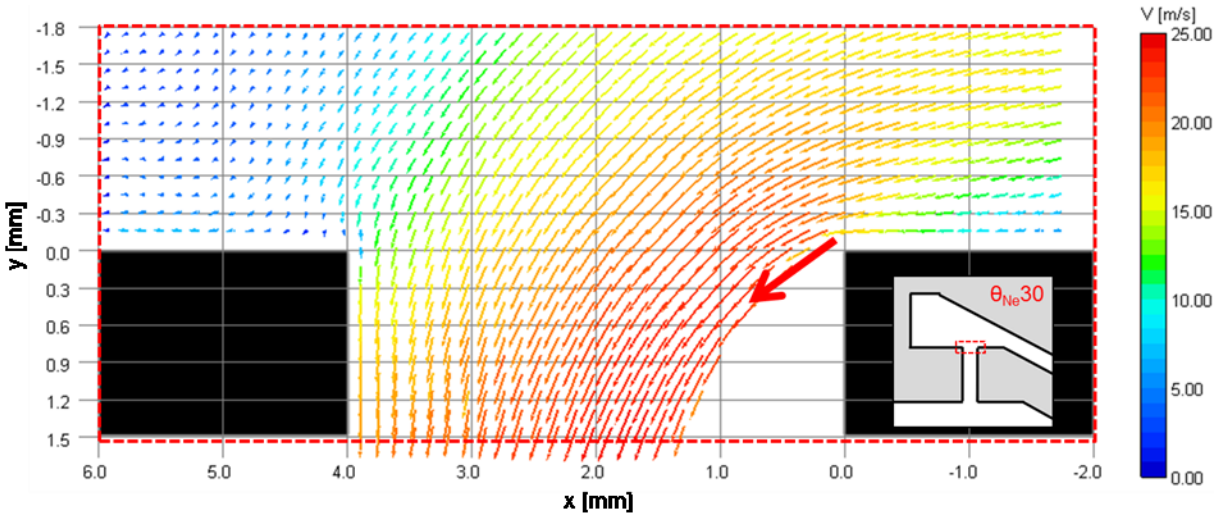

(a) θ_{Ne} = 30º

(b)

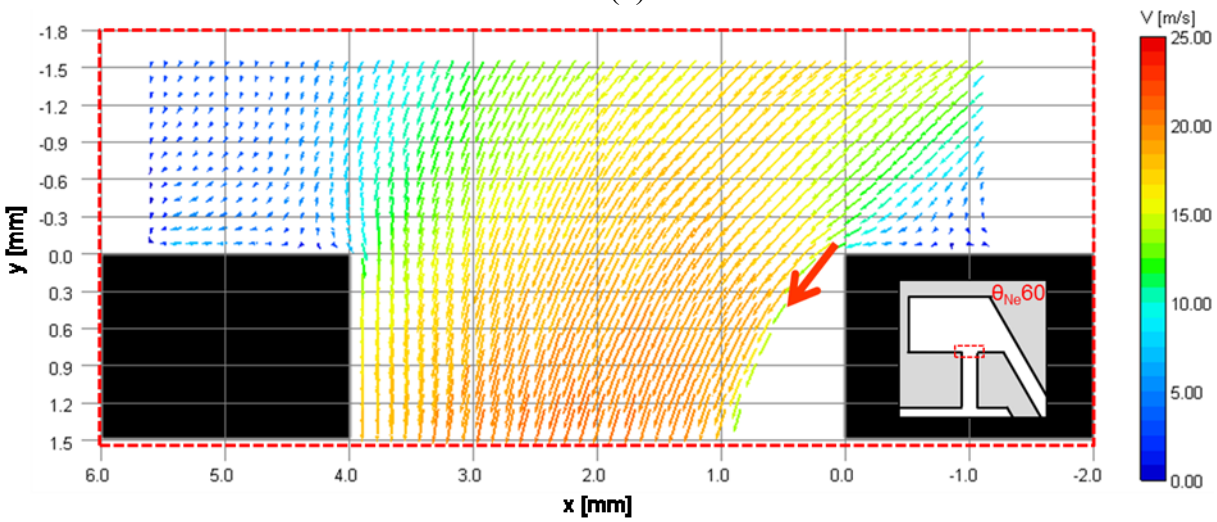

(b) θ_{Ne} = 60º

Figure 4.9 Velocity field in nozzle-hole inlet (V = 15.0 m/s)

In Figure 4.10 (a), definitions of inflow angle θ_{Vin} and cavitation thickness ratio W_C/W are explained. The inflow velocity V_{in} is selected from the nearest local velocity to the nozzle inlet where cavitation occurs, that is x ≈ 0.1 mm and y ≈ -0.1 mm. V_{in} is calculated from V_{Xin} and V_{Yin} which are obtained from PIV analysis. Cavitation thickness ratio W_C/W is measured at 0.375L distance from the nozzle inlet at super cavitation condition. Figure 4.10 (b) shows the graph of correlation between inflow angle θ_{Vin} and cavitation thickness ratio W_C/W. Large

inflow angle θ_{Vin} results in large cavitation thickness W_C/W. Knowing the inflow angle, we can predict the cavitation thickness in the nozzle by using this correlation. These results conclude that the cavitation thickness and length can be predicted by knowing the angle θ_{Vin} of inlet velocity at the nozzle inlet edge, which is governed by the nozzle geometry. The cavitation thickness is one of the important cavitation characteristics which is useful to determine the flow characteristic in the nozzle-hole as well as the jet deformation.

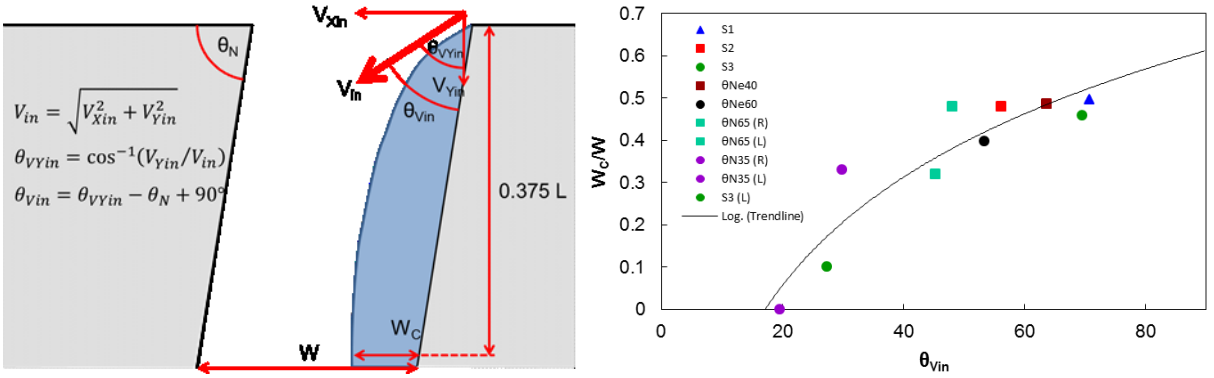

(a) Inflow angle θ_{Vin} definition (b) θ_{Vin} vs. W_C/W

Figure 4.10 Correlation between inflow angle and cavitation thickness

Turbulence intensity I in this work using 2D nozzles is simply defined by:

$$I = \frac{u'}{U}, \quad u' = \sqrt{k}, \quad k = \frac{1}{2}\left(\overline{u'_x}^2 + \overline{u'_y}^2\right), \quad U = \sqrt{\overline{u_x}^2 + \overline{u_y}^2} \qquad (4.1), (4.2), (4.3), (4.4)$$

$$u'_x = u_x - \overline{u_x}, \quad u'_y = u_y - \overline{u_y} \qquad (4.5), (4.6)$$

where u' is the root of the turbulence kinetic energy k measured in the 2D plane, and U is the mean velocity as expressed in Eq. (4.4). The turbulence kinetic energy k is defined by Eq. (4.3), which is characterized by measured root-mean-square of velocity fluctuations u'_x and u'_y defined by Eq. (4.5) and (4.6), respectively.

Figure 4.11 (a) and (b) show the measured turbulence intensity I for θ_{Ne} = 30º and 60º, respectively. Mean liquid velocities V in the nozzles are 17.5 m/s for both nozzles. The turbulence intensity was obtained by averaging 100 PIV analysis data, which is then plotted as the contour graph. The result shows that turbulence intensity is large in the recirculation flow area, and that turbulence intensity near the nozzle inlet for θ_{Ne} = 60º is clearly larger than that for θ_{Ne} = 30º. The large turbulence near the nozzle inlet is the reason why cavitation length and thickness fluctuate largely in the case of θ_{Ne} = 60º. Thus it was found to be important to consider the turbulence of the inflow which leads to unstable cavitation in the nozzle-hole.

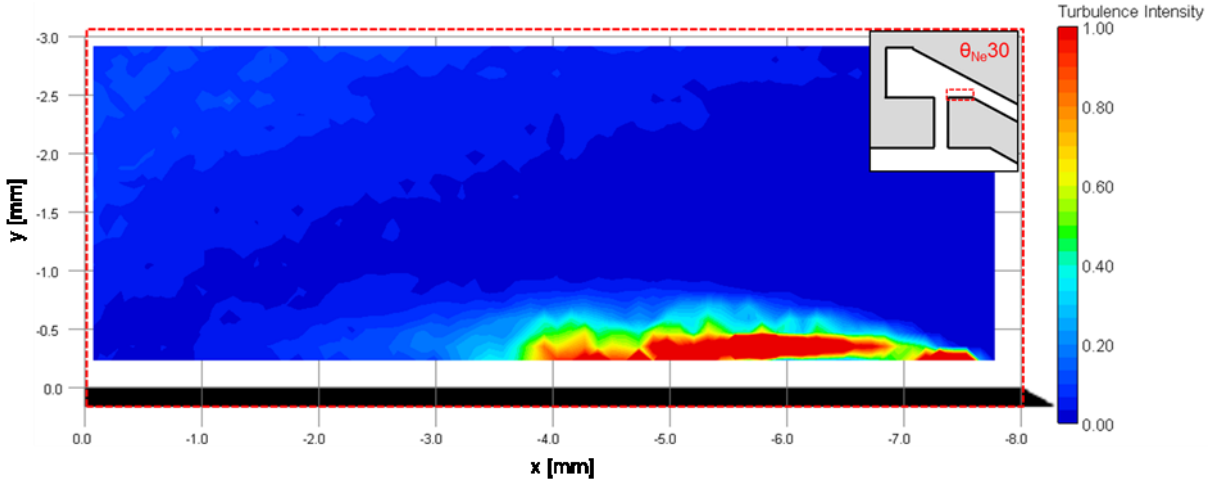

(a) $\theta_{Ne} = 30^{o}$

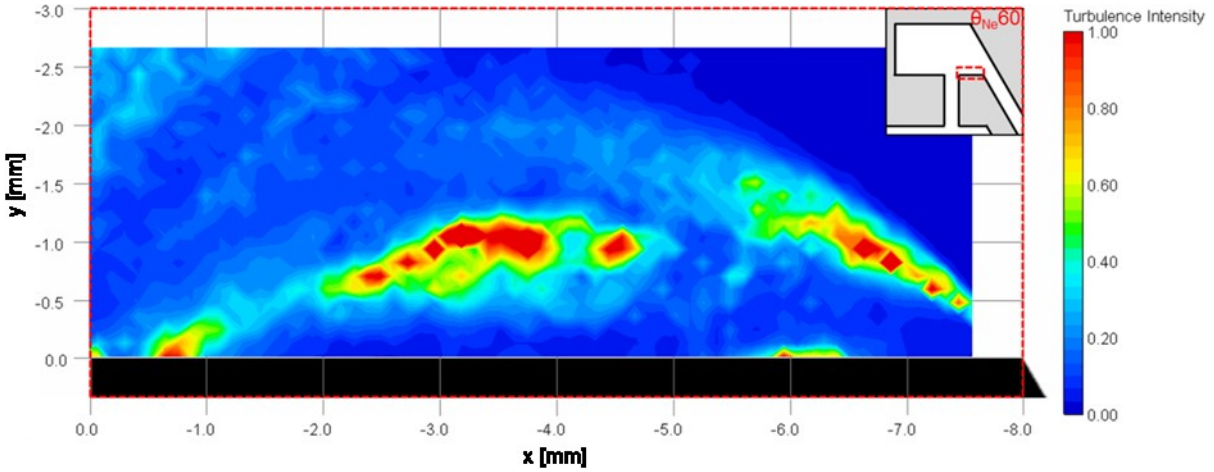

(b) $\theta_{Ne} = 60^{o}$

Figure 4.11 Turbulence intensity in mini-sac (V = 17.5 m/s)

Figure 4.12 (a) and (b) show the velocity field in the sac when the cavitation length L_C/L in the nozzle approximately 0.7 for low needle lift (S/W = 1) and high needle lift (S/W = 3), respectively. The results show that the incoming flow velocity to the sac depends on the gap S between the needle wall and its seat. The large gap decreases the incoming flow velocity so that the lateral inflow velocity component is small in a nozzle with large needle lift, as proven in Figure 4.12. In the same manner, the large lateral inflow explains why cavitation at S/W = 1 is thick, which decreases static pressure at vena contracta and increases cavitation length. We can also point out that the flow in the deep sac has a very slow velocity and it does not have a significant impact to the cavitation in the nozzle and the injected jet.

Figure 4.12 (c) and (d) show the velocity field in the sac when the normalized cavitation length L_C/L is approximately 0.8 (super cavitation regime) for deep sac (H_S/W = 7) and shallow sac (H_S/W = 5), respectively. The results show that for the shallow sac, recirculation flow velocity in the sac is higher than that for the deep sac. In the experiment on cavitation in mini-sac nozzle with real geometry, which is discussed in the next chapter, it is revealed that the recirculation flow in the sac is the cause of string cavitation. Thus from this result it can be stated that the shallow sac may increase the probability of string cavitation occurrence in sac.

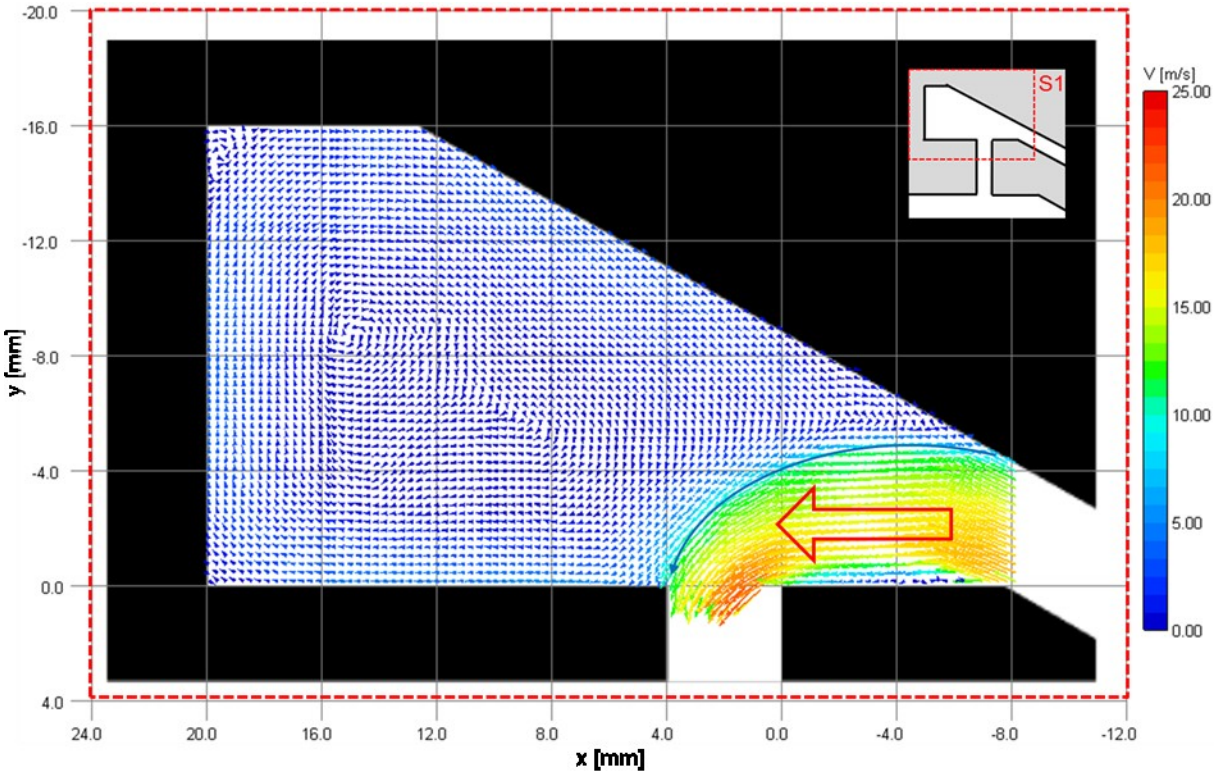

(a) S/W = 1 (V = 15.0 m/s)

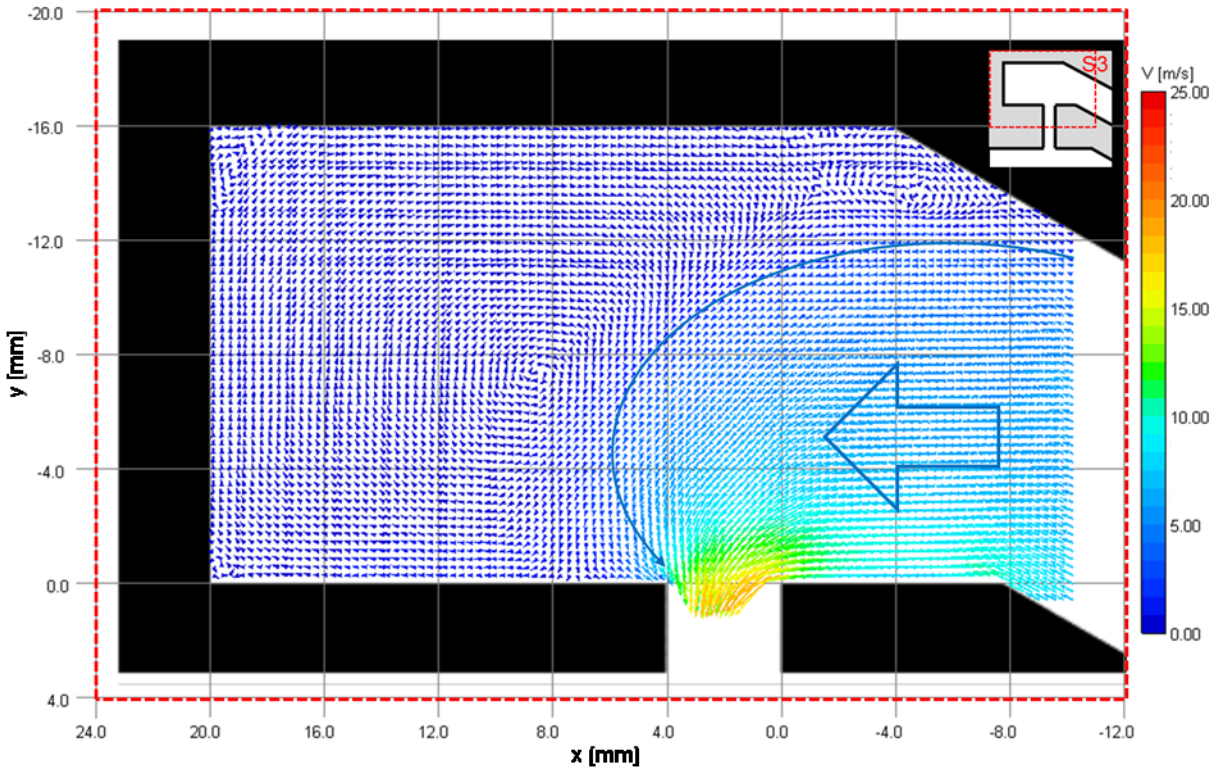

(b) S/W = 3 (V = 17.5 m/s)

Figure 4.12 Velocity field in mini-sac

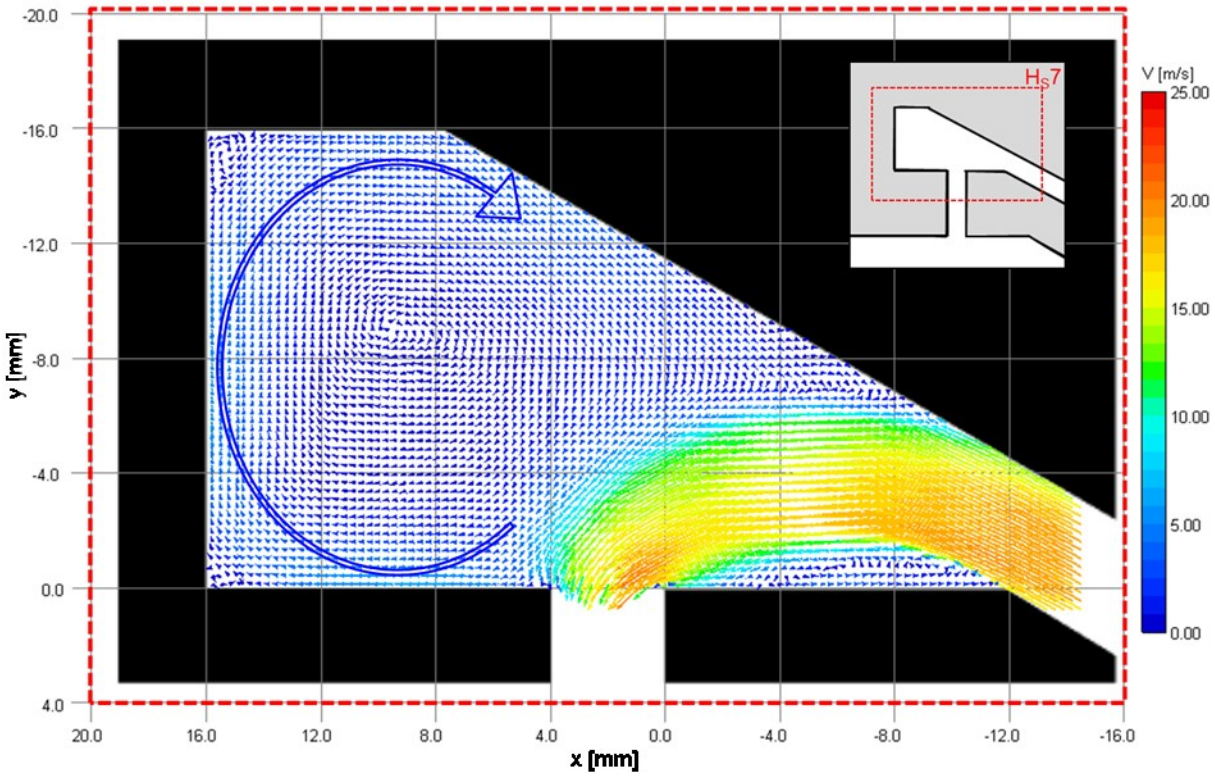

(c) $H_S/W = 7$ (V = 16.0 m/s)

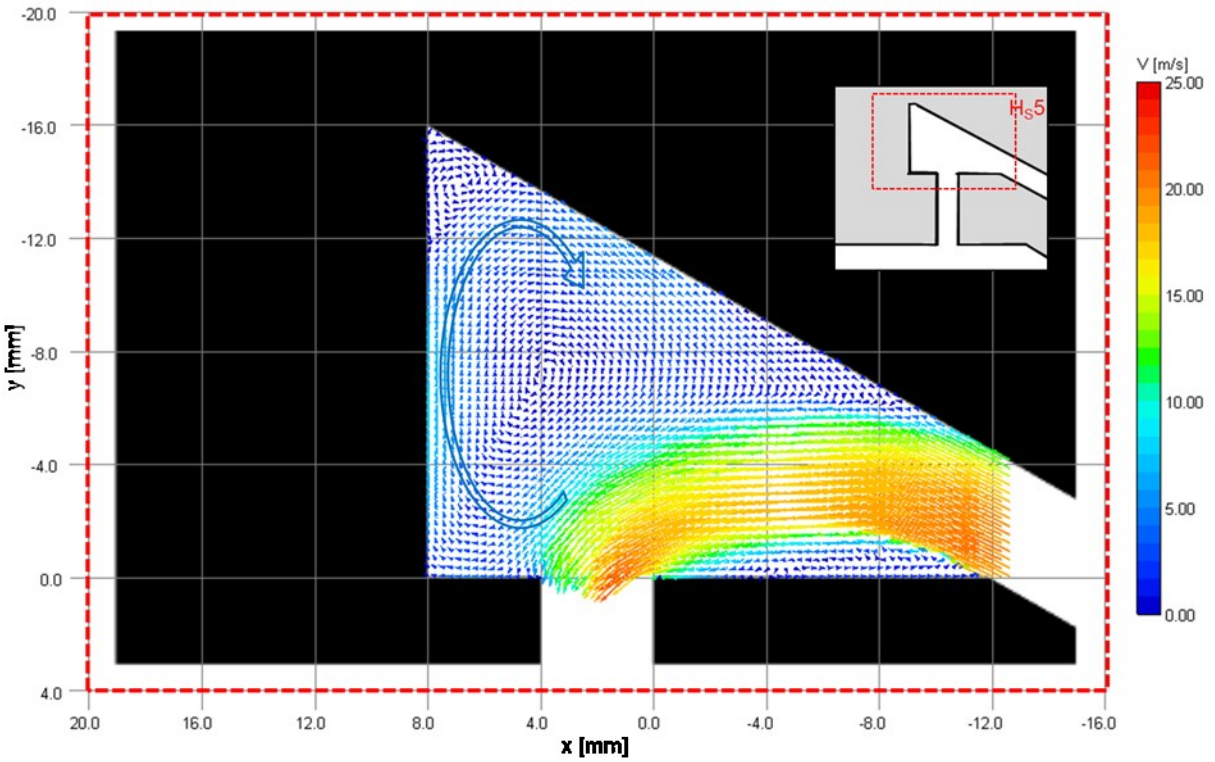

(d) $H_S/W = 5$ (V = 16.0 m/s)

Figure 4.12 Velocity field in mini-sac

Figure 4.13 (a) and (b) show the instantaneous velocity fields near the nozzle exit obtained by PIV for θ_N = 90º and 65º, respectively. The liquid velocities V for both cases are 15.0 m/s. As a result of the large cavitation clouds shedding from the tail of the thick film cavitation for large θ_N of 90º, large vortices of about 1 mm remain near the nozzle exit, as shown in Figure 4.13 (a). The large vortices induce large deformation of the liquid jet at the right interface, which will be shown later in this paper. In the case of θ_N = 65º with thin cavitation along the right wall, only small-scale turbulences are observed as shown in Figure 4.13 (b). From this result, it can be concluded that the cavitation thickness plays important role in large vortices generation, which then induces a large deformation of the injected liquid jet.

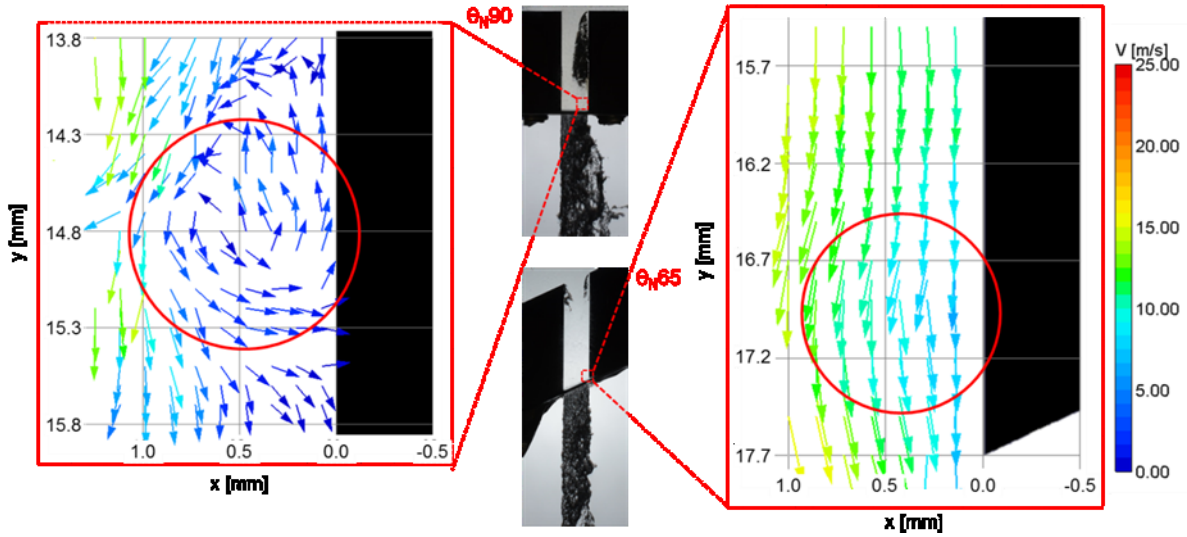

(a) θ_N = 90º (b) θ_N = 65º

Figure 4.13 Velocity field just above the nozzle exit for θ_N = 90º and 65º (V = 15.0 m/s)

Figure 4.14 shows a high-speed image sequence of a liquid jet and measured velocity field near the nozzle exit obtained at the same time for super cavitation of V = 15.0 m/s and θ_N = 90º. A cavitation cloud with a vortex flow shed from the tail of the sheet cavitation is observed at time t = 0 - 0.5 ms. Since the vortex is formed near the nozzle exit at super cavitation, it flows out of the nozzle exit at t = 0.5 ms and deforms the liquid jet drastically at t = 0.7 – 0.9 ms, which leads to a large jet angle and atomization enhancement. This result shows the importance of cavitation cloud shedding, which leads to vortex flow in a nozzle of fuel injector. The phenomenon shows a great impact on liquid jet deformation before the primary jet breakup of the injected liquid.

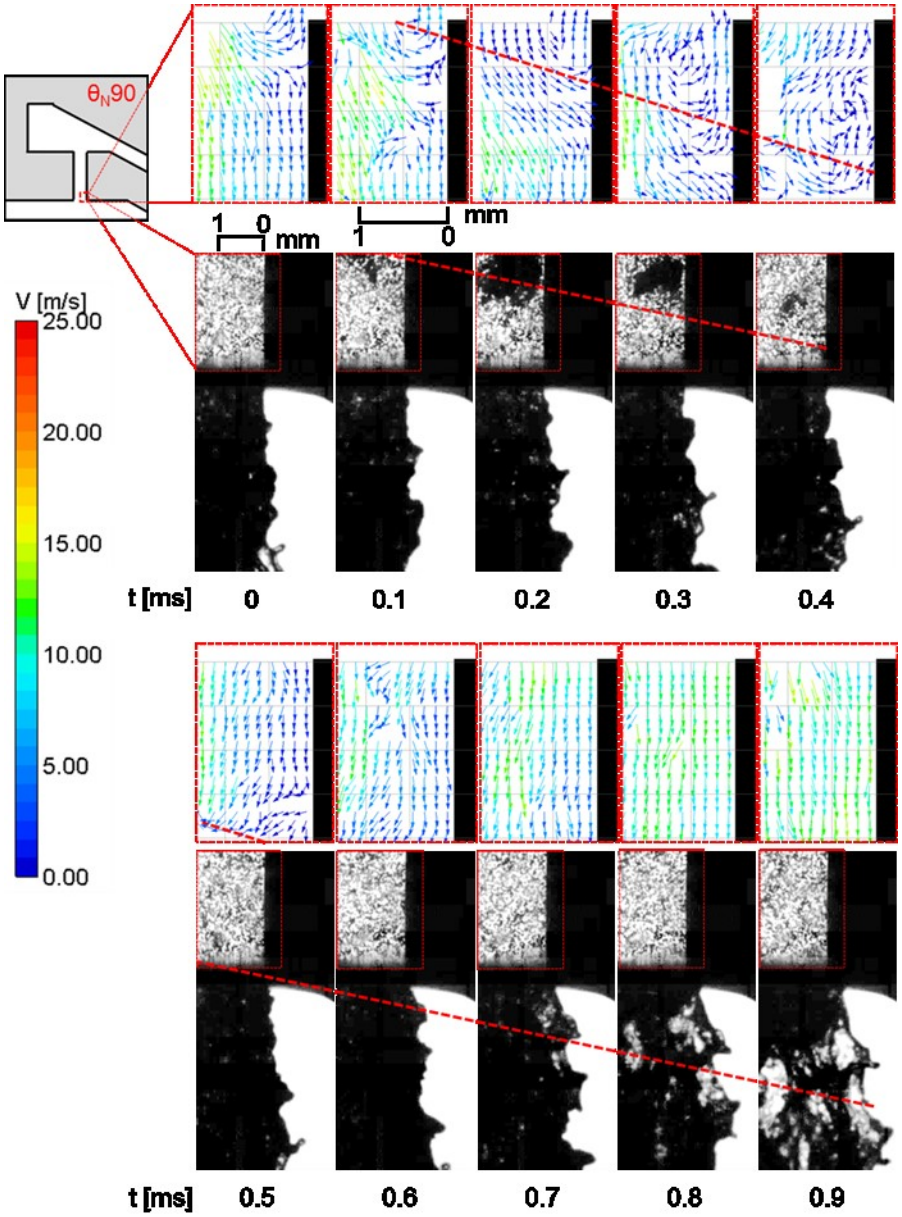

Figure 4.14 A vortex induced by cloud cavitation and liquid jet deformation by the vortex (θ_N = 90º, V = 15.0 m/s)

Not only the above single event of vortex induced liquid jet deformation, some series of cavitation cloud shedding has to be examined. Therefore, high-speed visualization of cavitation for S/W = 1 and V = 16.6 m/s was conducted. A high-speed image of cavitation in the nozzle-hole is shown in Figure 4.15. The images were captured with 87,137 fps so that the images with 11.5 μs time interval were obtained. A large cavitation cloud is shed at t = 459 μs and a small cloud is shed at t = 2066, 3903, and 4822 μs.

Image analysis was conducted to measure void fraction in the region shown in Figure 4.16. The photos were converted to binary images with an appropriate threshold, and void fraction α at the region shown with a red rectangle at y = 11.2 – 12.8 mm from the nozzle inlet was measured.

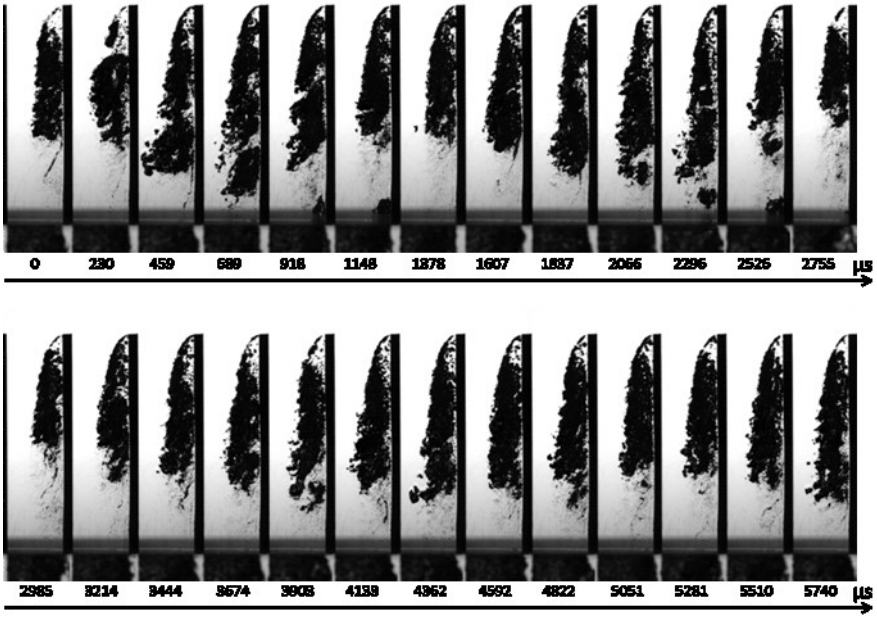

Figure 4.15 High speed images of cavitation in mini-sac nozzle (S/W = 1, V = 16.6 m/s)

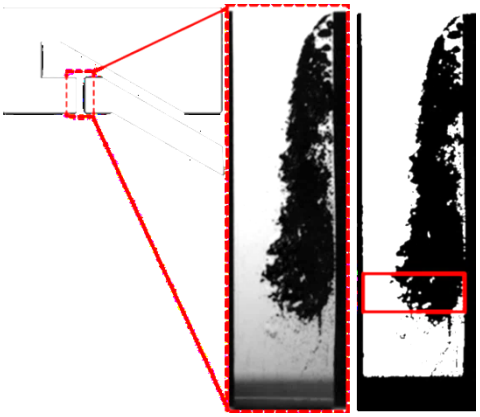

Figure 4.16 Original and binary images (S/W = 1, V = 16.6 m/s)

Figure 4.17 shows measured cavitation fraction in the area. The cavitation fraction α fluctuates largely. When a large cloud is shed at t = 400 – 800 μs, α reaches 0.8. When a small cloud is shed at t = 1,800 – 2,400 μs and 3,800 – 4,800 μs, α reaches 0.4. Three clouds are shed within 5 ms, which gives about 0.6 kHz in shedding frequency. It was reported by Sou et al. [24] that small cavitation clouds were shed from thin cavitation film in 2D symmetric nozzle. The present result implies that the lateral inflow increases cavitation thickness and decreases cavitation shedding frequency.

Figure 4.18 shows the relationship of inflow angle θ_{in}, cavitation thickness W_C/W, velocity V_{SupCav} at super cavitation, and jet angle θ_{SupCav} at super cavitation condition for various nozzle geometries. The result summarizes the effect of the nozzle geometry factors on internal flow characteristics and the injected jet. It is obvious that the increase of inflow angle θ_{in} increases cavitation thickness W_C/W, decreases the mean flow velocity V_{SupCav} at super cavitation, and increases jet angle θ_{SupCav} at super cavitation. The data show that the effects of

nozzle angle θ_N, needle lift S/W, and needle angle θ_{Ne} are dominant for cavitation and the resulting liquid jet. This information is useful when designing a new mini-sac nozzle by considering all geometry factors.

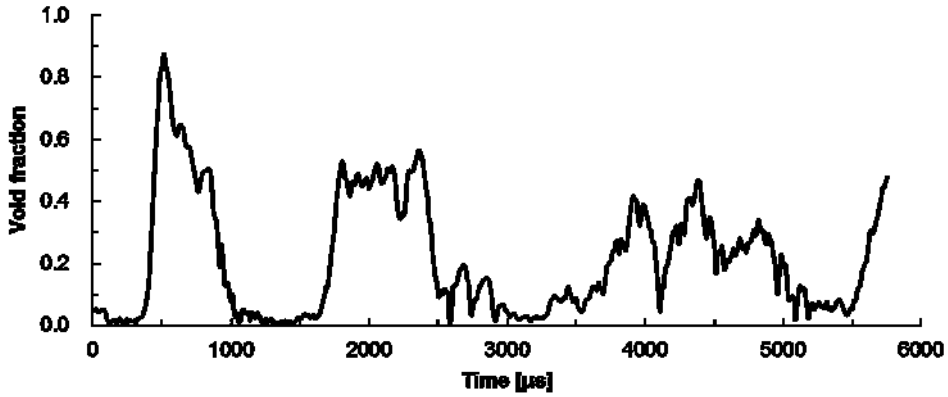

Figure 4.17 Cavitation fraction in the area between 11.2 mm to 12.8 mm from nozzle inlet (S/W = 1, V = 16.6 m/s)

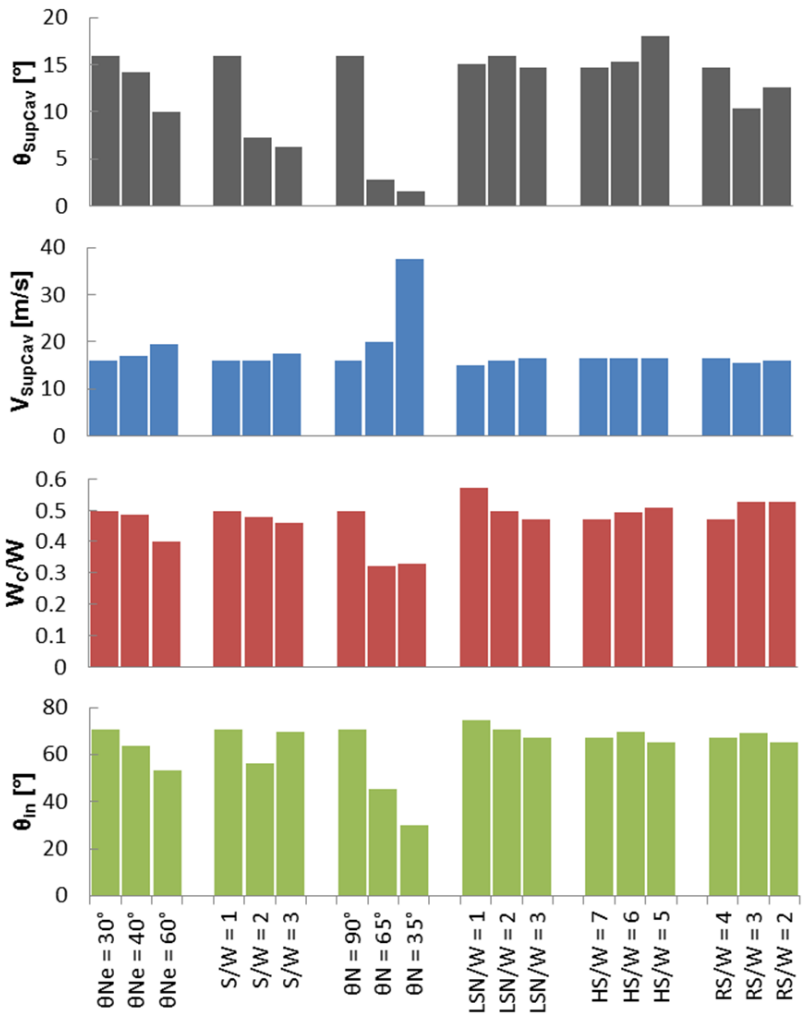

Figure 4.18 Graphs of inflow angle, cavitation thickness, velocity, and jet angle at super cavitation for various nozzle geometries conditions

4.4 Summary

In order to clarify the effects of some geometry factors of the mini-sac diesel fuel injector on cavitation and the liquid jet, such as needle angle, needle lift, nozzle angle, distance between needle seat corner and nozzle inlet, sac depth, and sac radius, a visualization of cavitation and the discharged liquid jet into the ambient air as well as PIV analysis were conducted using some 2D mini-sac model nozzles with various needle angles θ_{Ne}, needle lift S, nozzle angles θ_N, needle seat corner and nozzle inlet distance L_{SN}, sac depth H_S, and sac radius R_S. As a result, the following conclusions were obtained.

(1) Small needle angle θ_{Ne} and low needle lift S lead to a large lateral inflow velocity component and result in a thick and long cavitation, which is the cause of large cavitation clouds and vortices shedding and large jet angle.
(2) Large needle angle θ_{Ne} increases a turbulence of the inflow, which increases the fluctuations of cavitation length, cavitation thickness, and liquid jet angle even at hydraulic flip.
(3) For large nozzle angle, cavitation clouds shed from the tail of the sheet cavitation are large due to a thick sheet formation downstream of the acute inlet edge, which leads to large jet angle.
(4) Nozzle with shallow sac has larger recirculation flow velocity in sac, which might be a main cause of string cavitation phenomenon.
(5) The cavitation thickness and length can be predicted by knowing the angle of inlet velocity at the nozzle inlet edge, which is governed by the nozzle geometry.
(6) The lateral inflow velocity component, which is strongly affected by the flow in the sac, determines the inflow angle, and therefore cavitation thickness, cavitation length, the cavitation cloud size, and the resulting liquid jet angle and atomization.

Chapter 5
Cavitation in Mini-Sac Nozzle

5.1 Introduction

Mini-sac type nozzle is generally used as a fuel injector in diesel engine. As explained in the previous chapters, in the mini-sac nozzle injector designing process, nozzle-holes are set at certain positions in the sac with certain nozzle angles. The needle valve moves to control the fuel injection into the combustion chamber. It is obvious that internal flow pattern in the injector changes with the needle lift. Since the transient characteristic in diesel fuel injection directly connected with the fuel-air mixture preparation in the combustion chamber, it is very important to understand the effect of needle lift on cavitation occurring in the nozzle as well as its effect on the injected liquid jet. However, their effects have not been clearly understood yet. In the previous chapter, experiment using mini-sac nozzles with 2D structure was explained, Since the real shape of fuel injector is three-dimensional, further study to reveal cavitation characteristic in 3D nozzle is necessary. However, cavitation in cylindrical nozzle is complicated and difficult to be captured and measured quantitatively due to the refraction at the injector walls.

In this study cavitation in transparent mini-sac 3-hole nozzles was investigated. Experiment using two different fluids, i.e. water and sodium iodide solution was conducted. The sodium iodide was used to adjust the refractive index, thus refractive index matching between the fluid and the nozzle acrylic can be obtained. The needle lift was varied to understand its effects on cavitation and the injected liquid jets as well as internal flow pattern in the sac. Injection pressure is varied to observe the cavitation pattern under various mean flow velocities V in the nozzle. Stereoscopic particle image velocimetry (PIV) analysis was carried out to measure vertical flow structure in the sac.

5.2 Experimental Setup

In this experiment, two different fluids were used, i.e. water and sodium iodide solution. As mentioned above, sodium iodide (NaI) was added to water to match the refractive index between the acrylic nozzle and the liquid, so the effect of refraction can be minimized. Note that the physical properties of the solution are different from those of water. Figure 5.1 (a) shows the schematic of imaging experimental apparatus. Filtered tap water at 30±0.5 ºC in temperature was injected into the ambient air through the mini-sac nozzle. The injected liquid flow rate was measured by a flow meter (Keyence FD-SS20A). Still images of cavitation and a liquid jet were captured using a digital camera (Nikon D800) and a flash lamp as a backlight (Nisshindenki Co., Micro Flash Stroboscope, MS-1000/LH-15M, 2-4 μs in duration). High-speed images of string cavitation in sac were taken using a high-speed camera (Photron FASTCAM SA-Z) and a metal-halide lamp (Kyowa Co. Ltd., MID-25FC). A diffuser was placed between the nozzle and backlight source to evenly distribute the light into the camera

sensor. Figure 5.1 (b) shows the schematic picture of experimental apparatus for stereoscopic PIV experiment. For this experiment, two high speed cameras (JAI Co. Ltd., AM-200GE) with 1600 × 1200 pixels resolution, two lenses for each high speed camera (AI Micro-Nikkor 105 mm f/2.8) with four teleconverters ×1.4 (two teleconverters for each high speed camera) laser sheet generator (YAG: Nd3+, 532nm in wavelength, 100mJ/pulse of energy output, and 5ns in pulse duration, 1.4 mm in sheet thickness) were used. The cameras and lenses were set so that the spatial resolution after calibration is 15 μm/pixel. The laser sheet generator was used to illuminate a specific plane area in the sac. Tracer particles are usually introduced to the liquid for the PIV analysis. In this experiment, microbubbles were formed in the tank due to the intensive interaction among the atmospheric air and the liquid jet which is directed directly to the liquid interface, as shown in Figure 5.1 (b). These microbubbles, whose diameters were about 20 – 90 μm were utilized as the tracer particles for the PIV analysis. Figure 5.1 (c) shows the image of experimental setup of stereoscopic PIV.

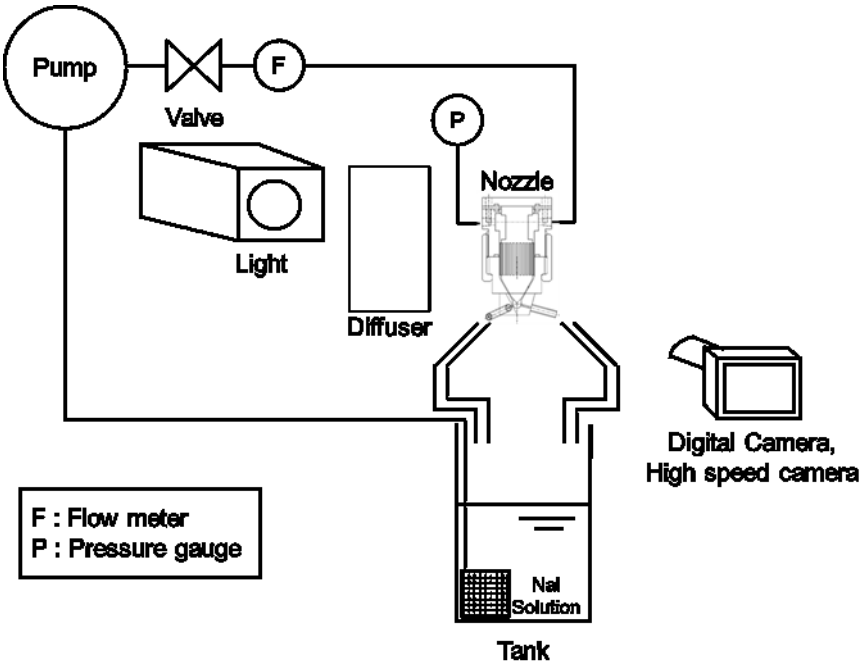

(a) Schematic picture of imaging experimental apparatus

Figure 5.1 Experimental apparatus

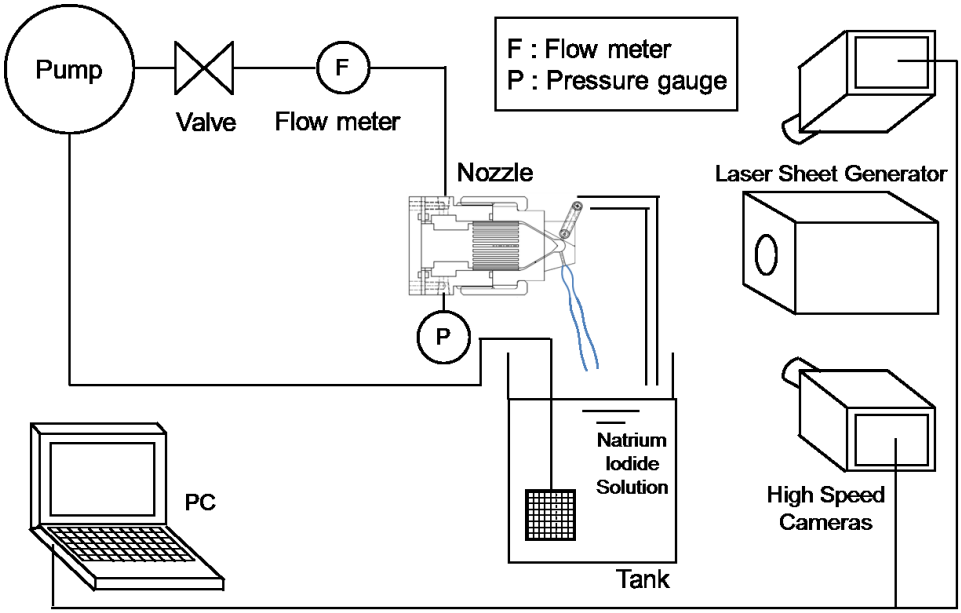

(b) Schematic picture of stereoscopic PIV experimental apparatus

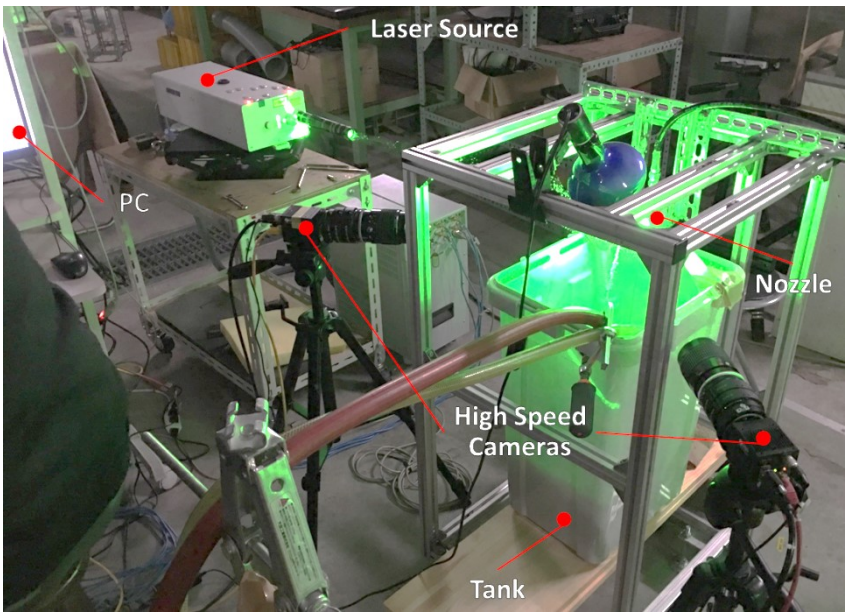

(c) Experimental setup of stereoscopic PIV

Figure 5.1 Experimental apparatus

In this experiment, a large mini-sac nozzle with true-shape, 3-holes of 2 mm in diameter was used as shown in Figure 5.2. The nozzle model consist of several parts which then assambled together to form the overall nozzle, as we can see in Figure 5.2 (a). The nozzle tip indicated with grey color has a flat sides and bottom for imaging. At the upper part of the nozzle body, a needle lift adjustment part, whose thicknesses are 3, 5, 9, and 13 mm, was set so that the needle lift ratio Z/D can be set to Z/D = 0.5, 1, 2, and 3. The visualization of cavitation inside a nozzle was conducted only in one nozzle, which is called as main nozzle-hole, while the exit of the other two holes are covered by a larger cylinders which then

connected to a hoses in order to drive the injected liquid into the receiving tank. Visualization of cavitation inside the nozzle and sac was done from two sides, i.e. front side and bottom side. String cavitation in the sac and three-dimensional velocity components in the sac were captured from the bottom.

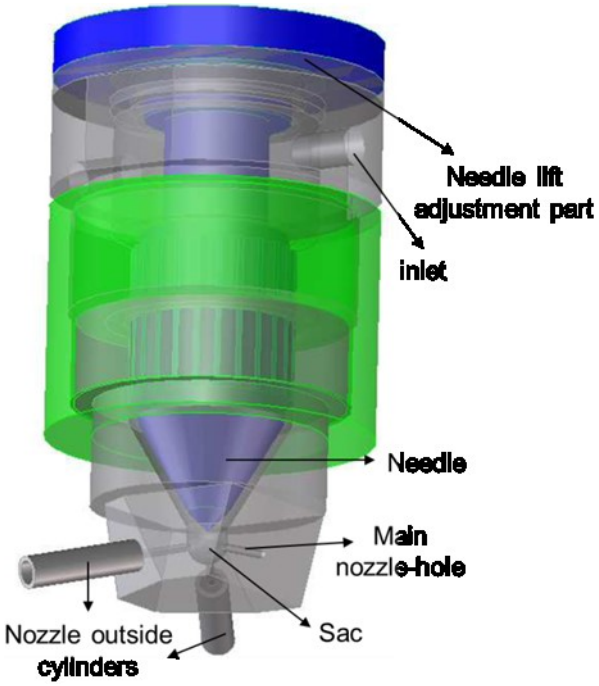

(a) Nozzle model

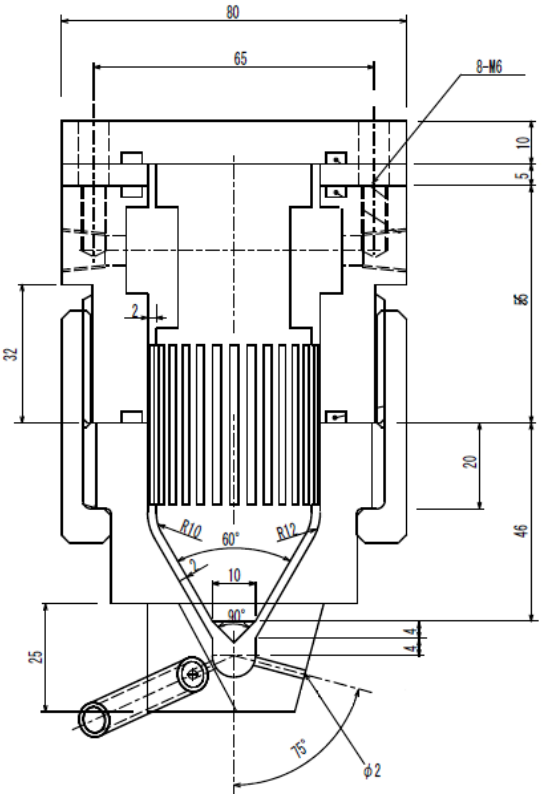

(b) Detail nozzle drawing

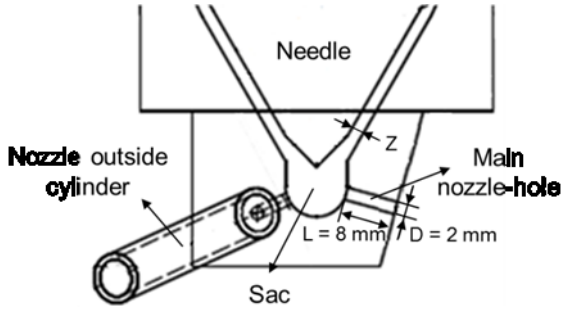

(c) Front view

Figure 5.2 Transparent scaled-up mini-sac nozzle model

In order to solve the refraction problem, refractive index matching was conducted to adjust refractive index of liquid with that of acrylic nozzle (n = 1.49). As reported by Bai and Katz [77], refractive index of water (n = 1.33) can be adjusted by adding sodium iodide (NaI). The formula of sodium iodide refractive index n is given by Eq. (5.1):

$$n = 0.2425c^2 + 0.0951c + 1.335 \quad (5.1)$$

where c is the definition of sodium iodide solution concentration, which is defined by Eq. (5.2):

$$c = \frac{m_{NaI}}{m_{NaI} + m_{H_2O}} \tag{5.2}$$

where m_{NaI} is the mass of sodium iodide and m_{H2O} is that of water. From Eq. (5.1), we get the required concentration c of 62.7%.

Fluid properties change due to sodium iodide addition into the water. Bai and Katz showed the two fluid properties, i.e. viscosity μ and density ρ, for sodium iodide solution based on Zaytsev & Aseyev's work [78]. The empirical expressions for calculating viscosity μ and density ρ are given by Eq. (5.3) and (5.4):

$$loq_{10}\mu = loq_{10}\mu_0 + \left[64\times10^{-2} + \left(-55.8\times10^{-4}T\right)\right]\cdot c \tag{5.3}$$

$$loq_{10}\rho = loq_{10}\rho_0 + \left[0.40367 + \left(-249\times10^{-6}T\right) + 183.2\times10^{-8}T^2\right]\cdot c \tag{5.4}$$

where T is water temperature and expressed in °C, $\mu_{0\ is}$ the viscosity of pure water which can be determined from Slott formula given by Eq. (5.5) and ρ_0 is the density of pure water which can be estimated from Eq. (5.6):

$$\mu_0 = 0.59849\left(43.252 + T\right)^{-1.5423} \tag{5.5}$$

$$\rho_0 = 1000 - 0.062T - 0.00355T^2 \tag{5.6}$$

Knowing the solution concentration c = 0.627 and controlling water temperature T (= 30°C), the solution density ρ and viscosity μ can be obtained, i.e. density ρ = 1770 kg/m^3 and dynamic viscosity μ = 2.73 × 10^{-3} Pa.s. Other liquid properties which are important for cavitation and jet analysis are vapor pressure and surface tension. As reported by Patil et al. [79], vapor pressures of aqueous electrolyte solutions were measured in the temperature range of 303.15 - 343.15 K (30 - 70°C) and concentration range of 1.0 – 8.6 mol/kg. From linear extrapolation calculation, the vapor pressure P_v of sodium iodide solution used in this study (molality = 11.215 moles) is almost equal to 2.3 kPa. While surface tension of aqueous electrolyte solutions was reported by Matubayasi et al. [80] from their work. Surface tension γ of sodium iodide solution used in this study is 83 mN/m. For water (T = 30 °C), the viscosity μ is 0.79 × 10^{-3} Pa.s [81], density ρ is 995 kg/m^3 [81], Vapor pressure P_v is 4.24 kPa [82], and surface tension γ is 71 mN/m [83]. Table 5.1 summarizes the liquid properties of the two liquids, i.e. water and sodium iodide solution at 30°C.

Table 5.1 Liquid properties of water and sodium iodide solution at 30°C

	Water	Sodium Iodide Solution
Dynamic viscosity μ [Pa.s]	0.79×10^{-3}	2.73×10^{-3}
Density ρ [kg/m^3]	995	1767
Vapor pressure P_v [kPa]	4.2	≈ 2.3
Surface tension γ [mN/m]	71.2	≈ 83
Molality [moles]	-	11.22

Figure 5.3 shows refractive index matching images. Figure 5.3 (a) and (b) are images of nozzle filled with water and sodium iodide solution respectively, while Figure 5.3 (c) and (d) are those of nozzle-hole filled with water and sodium iodide solution, respectively. As we can see in the images in Figure 5.3 (a) and (c), the lines of millimeter paper are distorted or even disappeared when a nozzle filled with water is placed in front of the millimeter paper, while in Figure 5.3 (b) and (d), we can see that the line of millimeter paper can be clearly seen and the distortion is minimized. Note that the refractive index of sodium iodide solution in Figure 5.3 (b) is still not perfectly matched with the acrylic refractive index so that the line distortion can be observed.

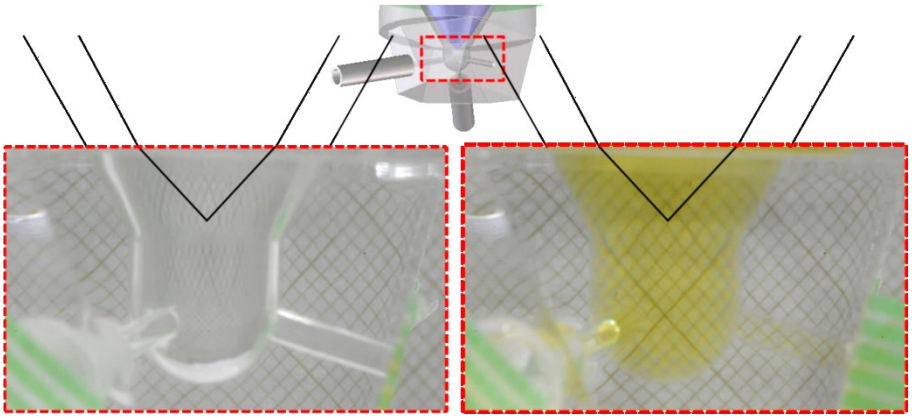

(a) Before index matching (b) After index matching

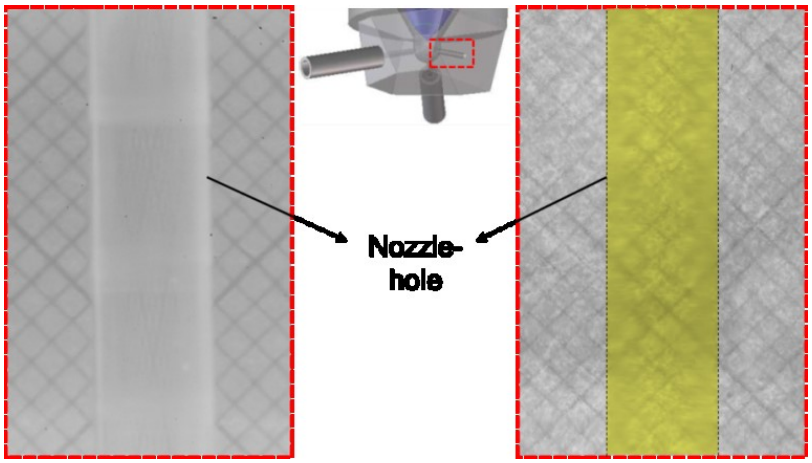

(c) Before index matching (nozzle-hole) (d) After index matching (nozzle-hole)

Figure 5.3 Refractive index matching

In stereoscopic PIV experiment, two high-speed cameras were utilized and placed with 50 degrees to the normal of the object plane. A circle calibration plate with many dots, three of which are big dots of 500 μm in diameter, was inserted into the sac for the Scheimpflug calibration. The plate was placed 1 mm upward the nozzle-hole inlet, where string cavitation occurs. By using camera controller software (FtrPIV, ver.3.0.15.9, Flowtech Research) and PIV analysis software (FtrPIV, ver.3.1.32.12, Flowtech Research), Scheimpflug calibration can be done as shown in Figure 5.4.

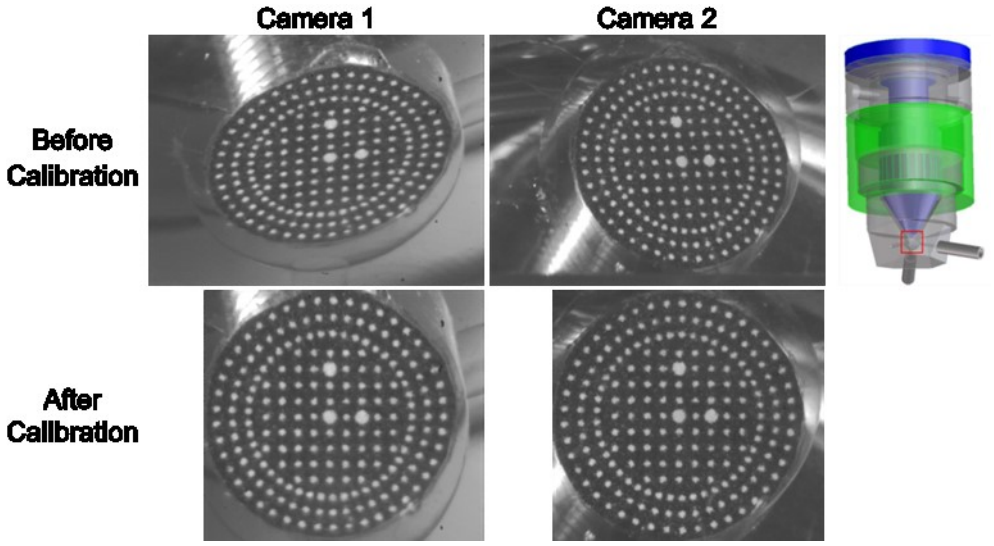

Figure 5.4 Scheimpflug calibration of the two cameras (before and after)

5.3 Results and Discussion

5.3.1 Visualization Results

Visualization of cavitation and the jets by using water and sodium iodide solution was done for every needle lift case, i.e. Z/D = 0.5, 1, 2, and 3, with various velocity V and injection pressure P_i. Figure 5.5 (a), (b), (c), and (d) show averaged backlight images of cavitation and jet for sodium iodide solution and water under Z/D = 0.5, 1, 2, and 3 condition, respectively. The averaged image was derived from 20 still images. Since two different liquids with different densities were used in this experiment, the cavitation number σ is used to compare the results with sodium iodide solution and water. The cavitation number σ is defined by Eq. (5.7):

$$\sigma = \frac{P_b - P_v}{\frac{1}{2}\rho V^2} \tag{5.7}$$

where P_b is back pressure, i.e atmospheric pressure, P_v is the vapor saturation pressure of liquid and ρ is liquid density.

From the images shown in Figure 5.5 (a) under low needle lift condition (Z/D = 0.5), cavitation develops and the liquid jet angle expands with the decrease of σ. Special remarks should be stated from other observation that a thin string cavitation occurs in the sac, connecting two nozzle-holes. The string cavitation in the sac and nozzle-holes avoids total hydraulic flip, which keeps the jet angle wide. In Figure 5.5 (b), cavitation and the jets at Z/D = 1 show a similar patterns with those for Z/D = 0.5. Note that the jet angle is slightly suppressed by the decrease in σ when the cavitation turns to hydraulic flip. Since string cavitation also occurs at Z/D = 1, the case can be considered as the transition with and without string cavitation. In the case of higher needle lift (Z/D = 2 and 3) as shown in Figure 5.5 (c) and (d), cavitation becomes longer and the injected liquid jet widen with the decrease in σ but the jet angle is suddenly suppressed when cavitation turns to hydraulic flip. Since the jet angle is completely suppressed in hydraulic flip regime in these needle lift conditions, it can be said that vortical flow does not exist or even though it exists, its effect on overall flow in the nozzle is very weak.

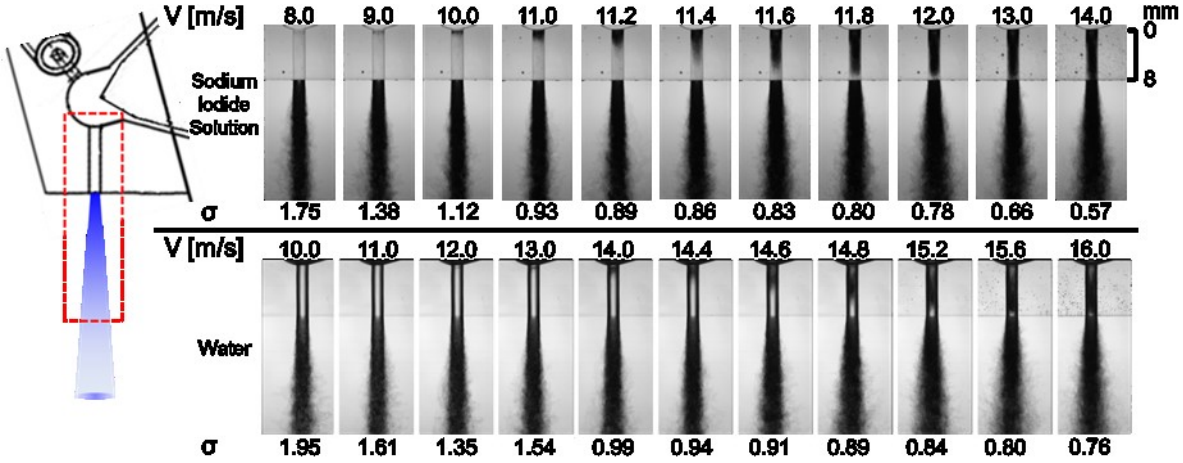

(a) Front View, Z/D = 0.5

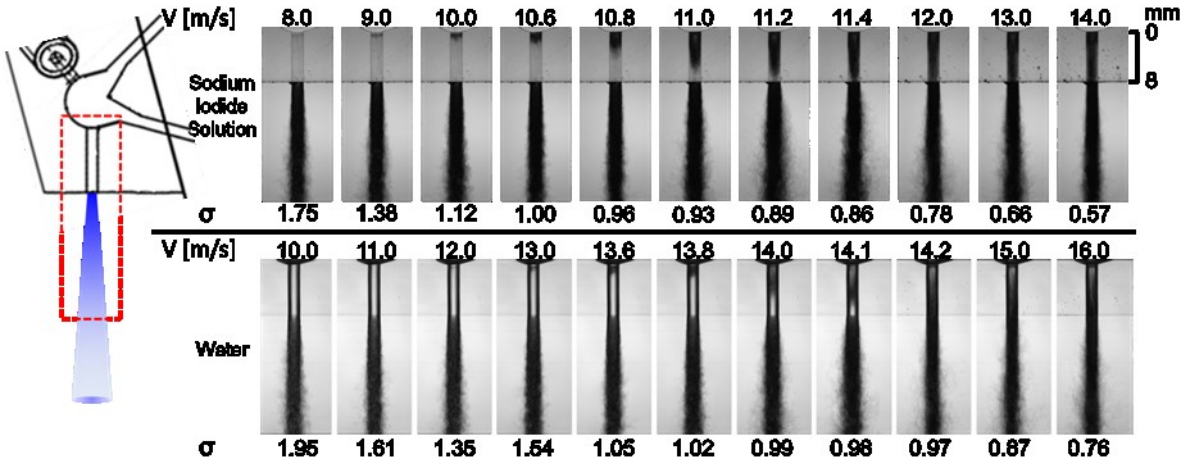

(b) Front View, Z/D = 1

Figure 5.5 Averaged backlight images of cavitation and jet for sodium iodide solution and water

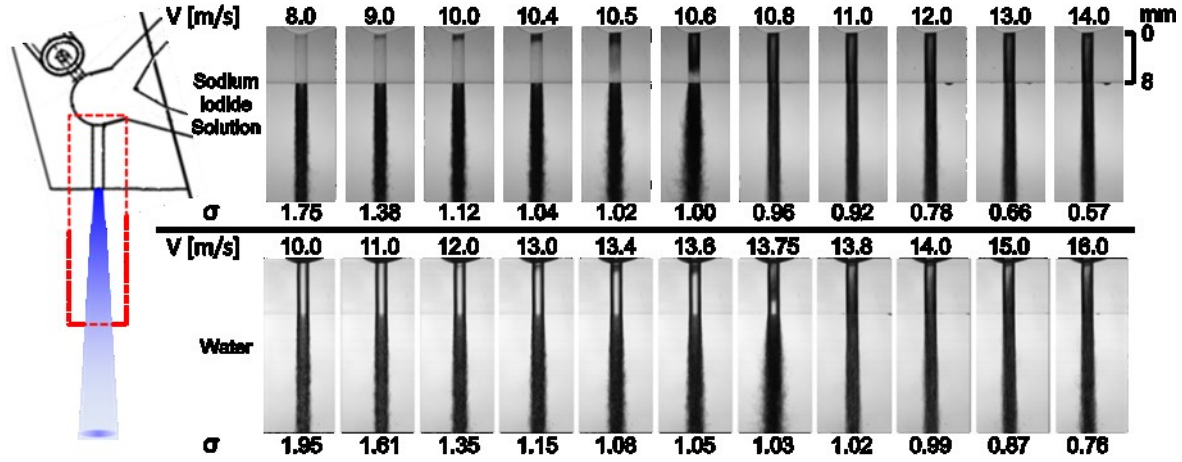

(c) Front View, Z/D = 2

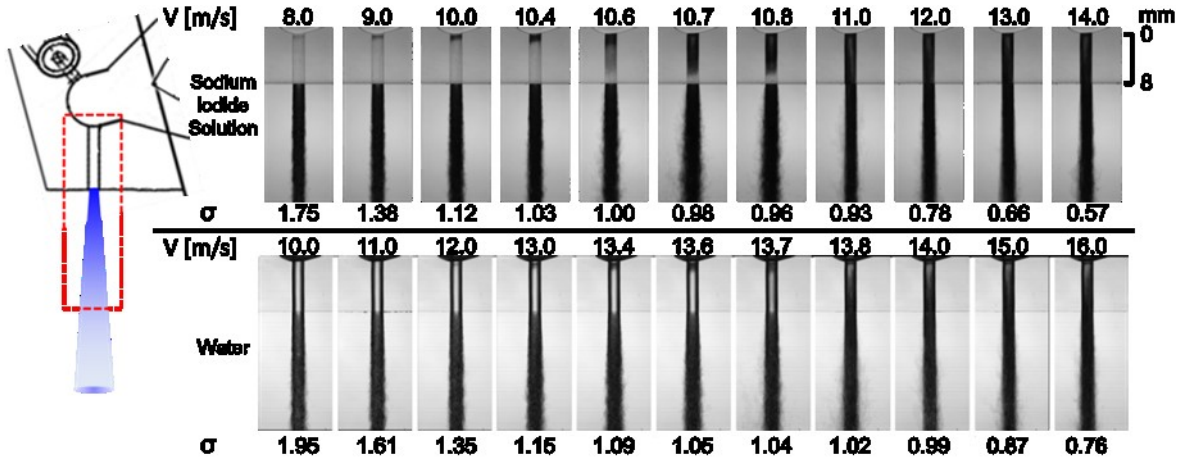

(d) Front View, Z/D = 3

Figure 5.5 Averaged backlight images of cavitation and jet for sodium iodide solution and water

5.3.2 Image Analysis

Image analysis was conducted to quantitatively measure the cavitation length and the jet angle for every needle lift cases and both liquids, i.e. sodium iodide solution and water. The measurement was done to 20 random sampling images for every mean flow velocity V and needle lift Z/D.

Figure 5.6 shows cavitation length ratio L_C/L with its standard deviation versus mean flow velocity V at various needle lifts Z/D for sodium iodide solution, and Figure 5.7 shows those for water. The result confirms the observation result that cavitation extends with the increase of mean flow velocity V. Cavitation length suddenly increases at certain velocity to form super cavitation. It is clear that cavitation under lower needle lift condition extends at higher mean flow velocity V than that under higher needle lift condition.

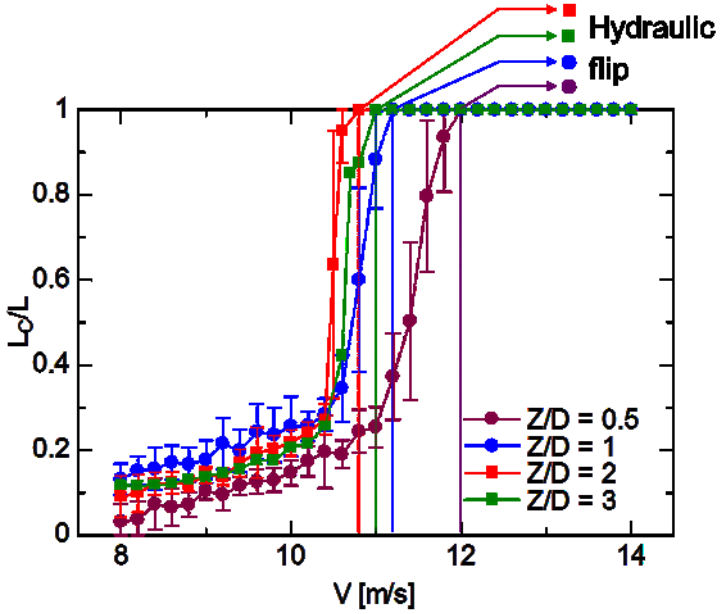

Figure 5.6 Mean flow velocity V versus cavitation length ratio L_C/L with its standard deviation at various needle lifts Z/D (sodium iodide solution)

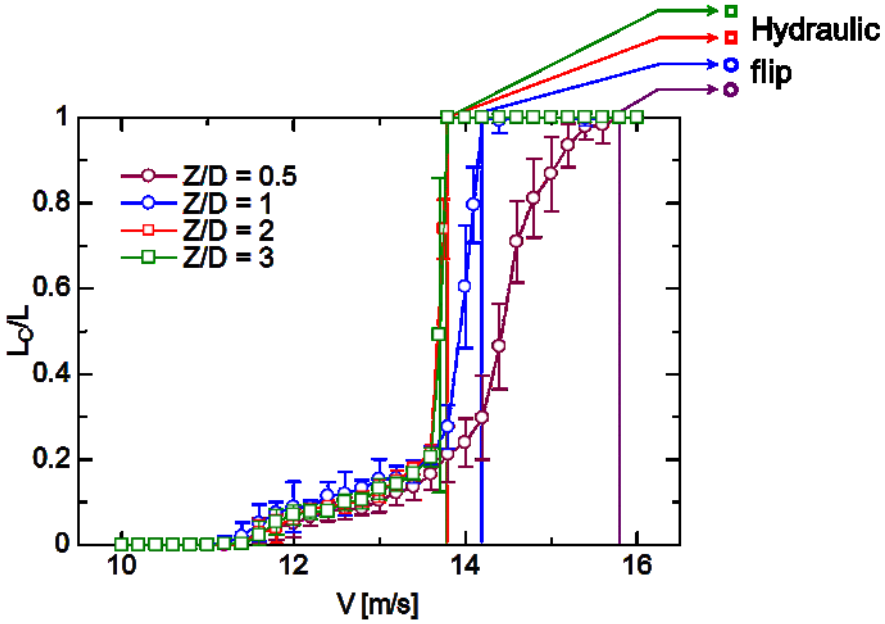

Figure 5.7 Mean flow velocity V versus cavitation length ratio L_C/L with its standard deviation at various needle lifts Z/D (water)

Figure 5.8 shows the relationship between jet angle θ with its standard deviation versus mean flow velocity V at various needle lifts Z/D for sodium iodide solution and Figure 5.9 shows those for water. Under very low needle lift condition (Z/D = 0.5), the jet angle increases with velocity, even if cavitation turns to hydraulic flip (in this case it should be called as imperfect hydraulic flip). It is obvious that jet angle fluctuates a lot in this needle lift case. Vortical flow characteristic in the sac and nozzle should be the reason of this fluctuation

and the wide jet angle as well. For Z/D = 1, the jet angle θ increases by the increase of cavitation length L_C, and then gradually decreases with the increase of mean flow velocity V when it turns to hydraulic flip. For this needle lift of Z/D = 1, it can be said that the effect of vortical flow remains in the sac and nozzle, that the jet angle still wide with large fluctuation at super cavitation and hydraulic flip. While in the case of higher needle lifts (Z/D = 2 and 3), it is confirmed that the jet angle tends to widen with the velocity increase or cavitation length increase, but then it is suddenly suppressed when the cavitation turns to hydraulic flip. From both figures, it can be confirmed that the tendencies of the cavitation development and the jet angle are same for both liquids, where only mean flow velocity V is different due to the density difference.

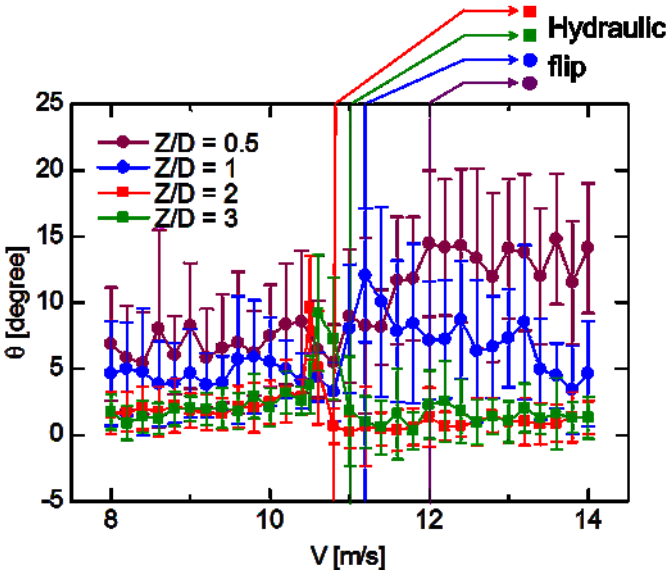

Figure 5.8 Mean flow velocity V versus jet angle θ with its standard deviation at various needle lifts Z/D (sodium iodide solution)

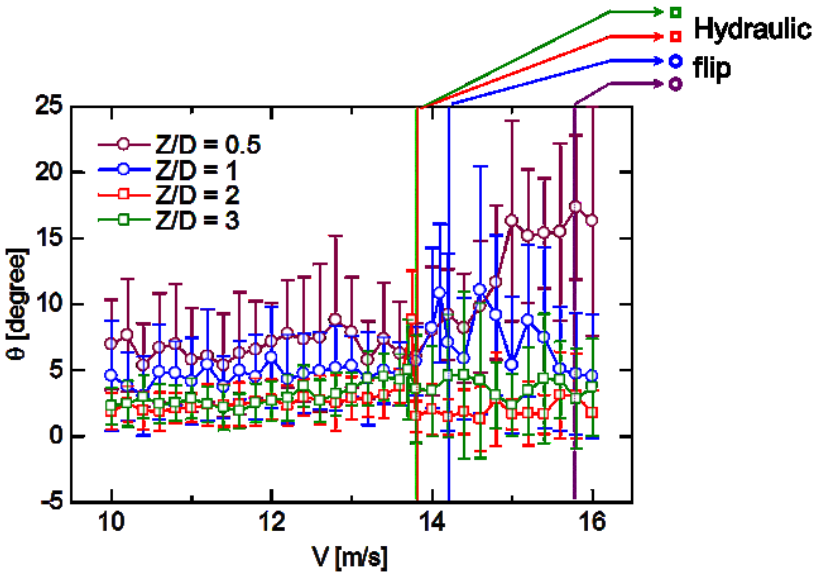

Figure 5.9 Mean flow velocity V versus jet angle θ with its standard deviation at various needle lifts Z/D (water)

Generalization should be made to make the result applicable to various liquids. The cavitation number σ defined by Eq. (5.7) was used to make this generalization. Figure 5.10 shows cavitation length ratio L_C/L versus cavitation number σ at various needle lifts Z/D for the two liquids. We can see that the cavitation extends to super cavitation and hydraulic flip when $\sigma = 1 \pm 0.05$.

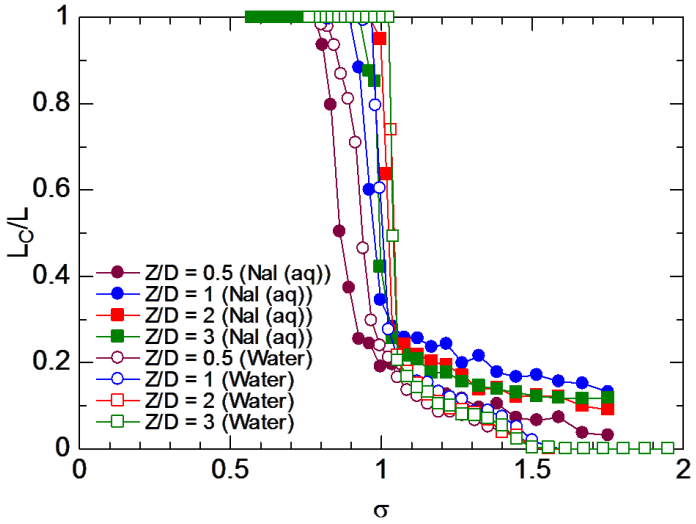

Figure 5.10 Cavitation number σ versus cavitation length ratio L_C/L at various needle lifts Z/D (sodium iodide solution and water)

5.3.3 String Cavitation in the Sac

Visualization of string cavitation in the sac was conducted with sodium iodide solution. Figure 5.11 shows the bottom view of the sac taken with a very long time instance of 1 second. For Z/D = 0.5 at t = 0.00 s, string cavitation occurs in the sac and is connected from main nozzle-hole (hole no. 1, located at the bottom part of the image) to hole no. 2 (located at upper left part). 0.06 s later string cavitation is observed and connected from hole no. 2 to hole no. 3 (located at upper right part of the image). At t = 0.23 s, string cavitation is formed from hole no. 1 to hole no. 3. At t = 0.32 s, two cavitation strings occur simultaneously from hole no. 2 to hole no. 3 and from hole no. 1 to hole no. 3.

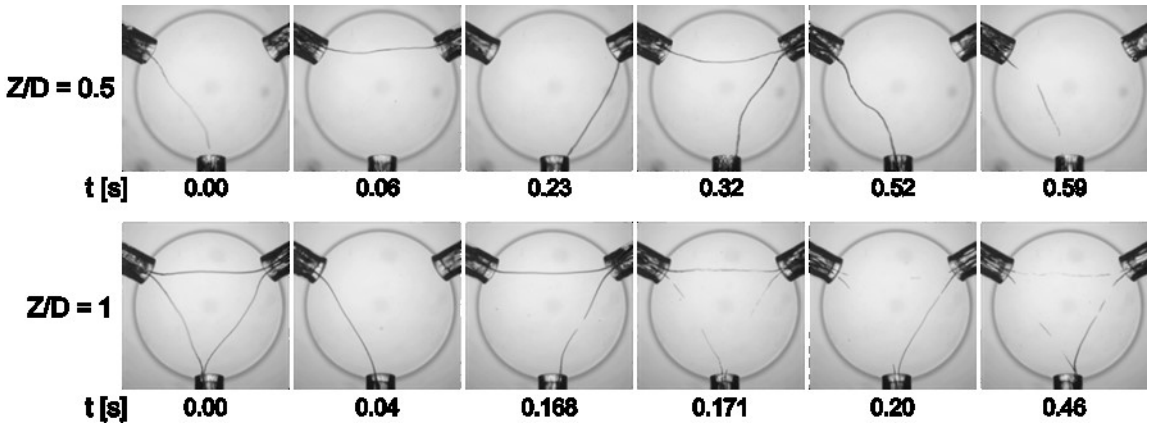

Figure 5.11 Bottom view of string cavitation in the sac (σ = 0.76)

Figure 5.12 shows merged images of made of 3,100 of string cavitation images in the sac for Z/D = 0.5 and 1. The merged images interpret the occupation of string cavitation in sac, thus we can understand the area of string cavitation occupation in the sac. String cavitation appears in random manner regardless the needle lift and cavitation number. Note that small dots in the sac are the accumulated micro bubbles.

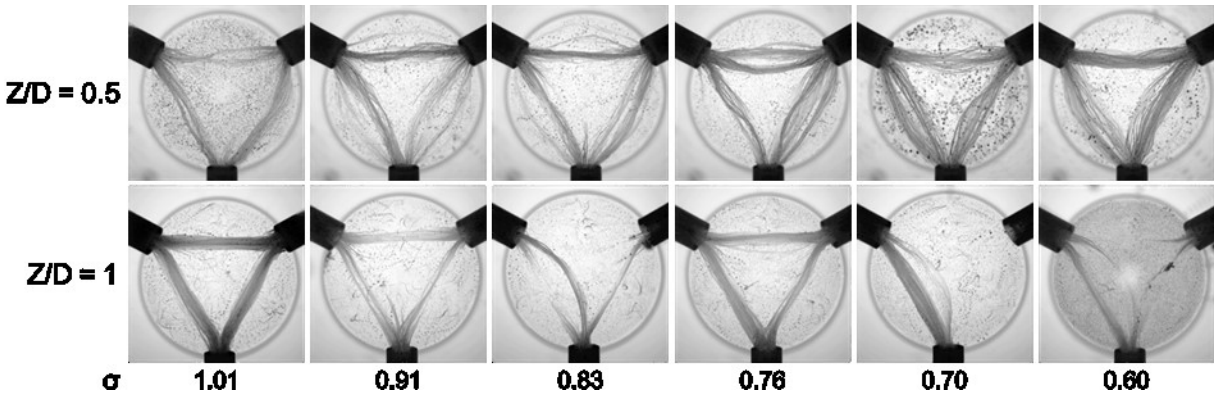

Figure 5.12 Merged images of string cavitation in the sac (random instance of 1 second period)

Figure 5.13 shows images of string cavitation occurrence probability in the sac for Z/D = 0.5 and 1. The string cavitation occurrence probability was calculated from 3,100 images for each case.

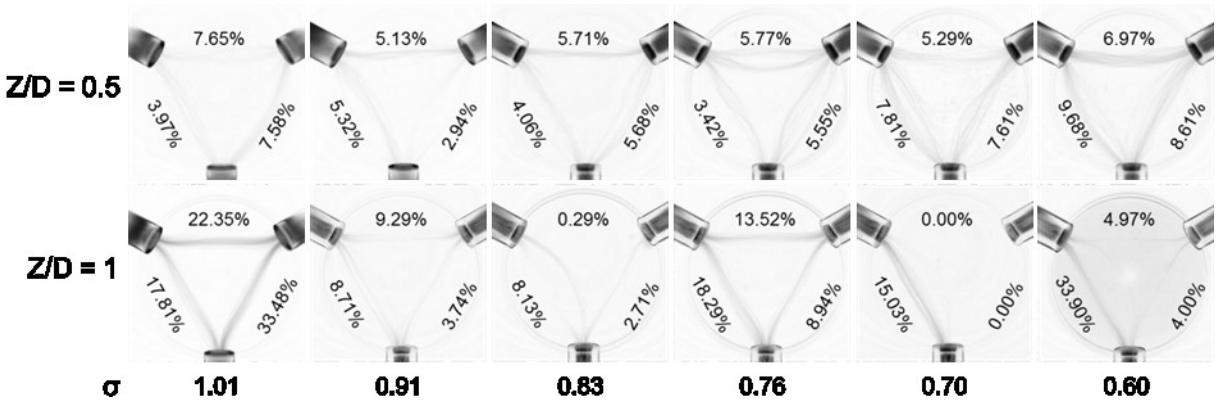

Figure 5.13 Probability of string cavitation occurrence in the sac (random instance of 1 second period)

Stereoscopic PIV was conducted to get the velocity distribution in the sac, especially in the area where string cavitation occurs. A plane was selected and a laser sheet, whose thickness 1.4 mm, was used to illuminate the selected area.

Figure 5.14 (a) and (b) show samples of instantaneous distributions in the plane at super cavitation regime for very low needle lift (Z/D = 0.5) and high needle lift condition (Z/D = 3), respectively. Since string cavitation is not steady, two results are shown for both needle lift cases. As shown in Figure 5.14 (a), string cavitation appears from the main nozzle (located at

the bottom of part of the image) to another nozzle on the left side in the first example, while in the second image it appears from main nozzle to the other nozzle on the right side. The PIV results show a vortical-velocity distribution around the string cavitation. For high needle lift string cavitation does not occur. In Figure 5.14 (b), there is no large vortical flow structure in the sac.

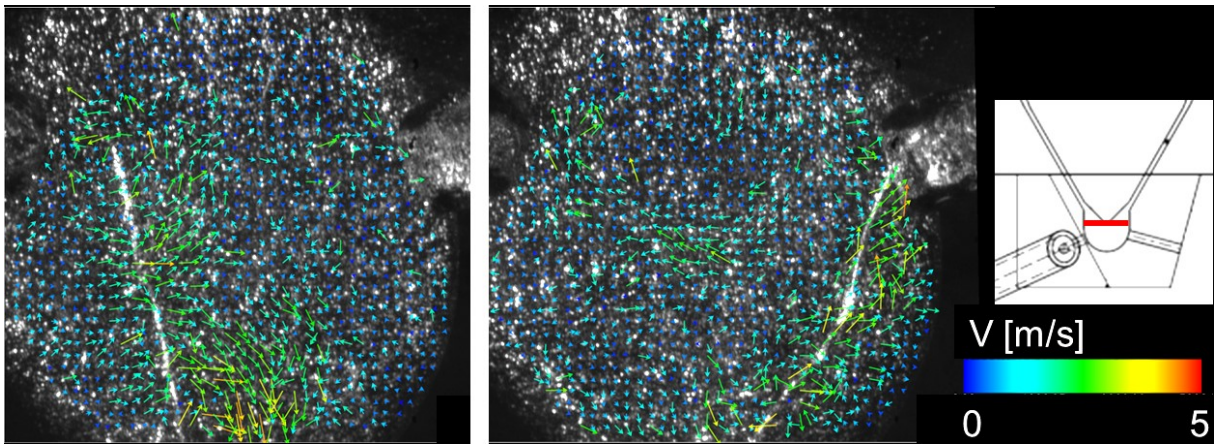

(a) Z/D = 0.5, V = 11.6 m/s

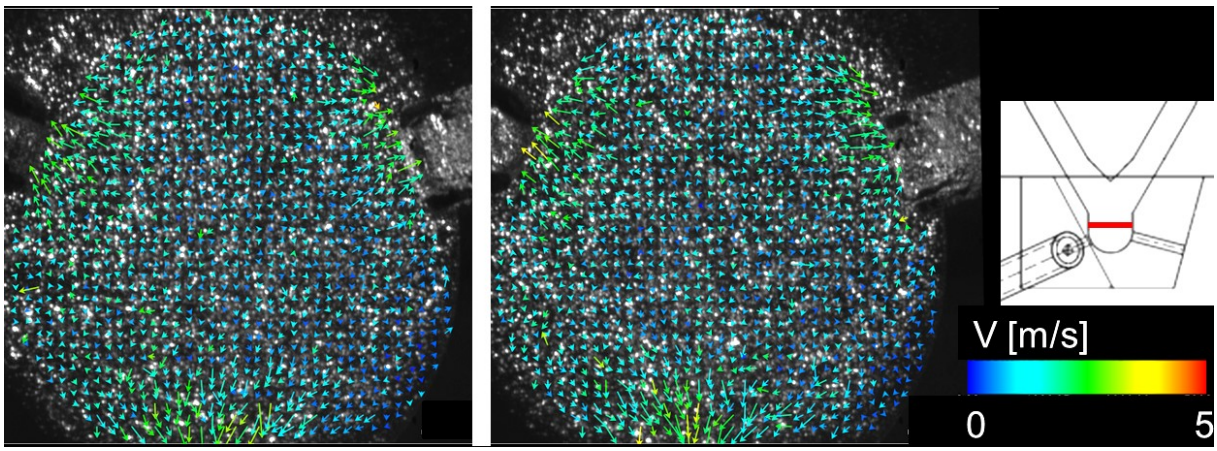

(b) Z/D = 3, V = 10.6 m/s

Figure 5.14 Instantaneous velocity-vector sample results of PIV in plane direction at the sac plane (view from sac bottom)

In order to more clearly show the vortical flow structure in the sac with string cavitation, some more velocity data are shown. Figure 5.15 (a) and (b) show the averaged velocity distributions in the horizontal plane for very low needle lift (Z/D = 0.5, V = 11.6 m/s) and high needle lift (Z/D = 3, V = 10.6 m/s), respectively. The results were obtained by averaging 500 velocities. As shown in the figures, high velocity is observed near the nozzle inlet.

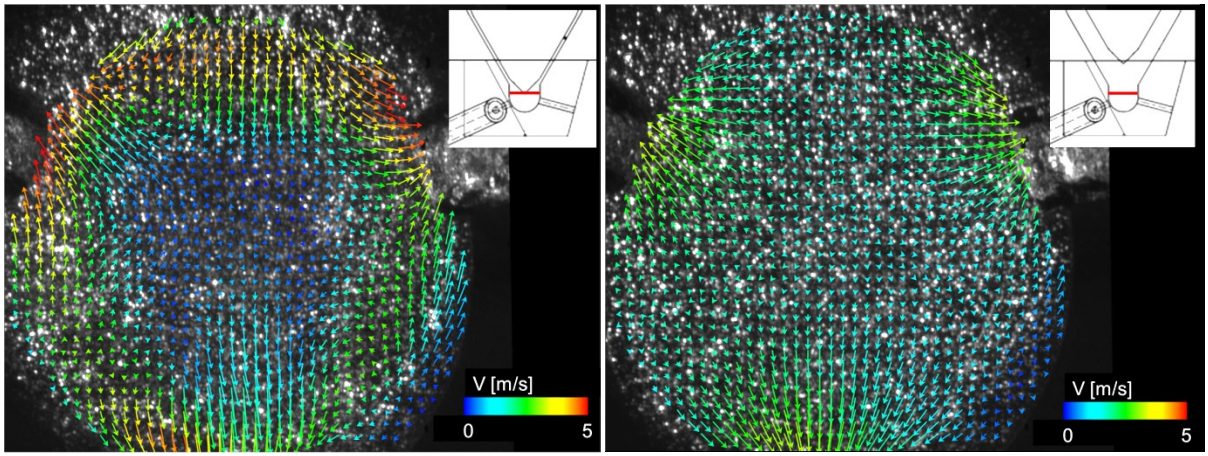

(a) Z/D = 0.5, V = 11.6 m/s (b) Z/D = 3, V = 10.6 m/s

Figure 5.15 Averaged velocity-vector results of PIV in plane direction at the sac plane (view from sac bottom)

Figure 5.16 (a) and (b) show the contour maps of mean downward velocity in normal direction of the sac plane (view from sac bottom) at super cavitation for very low needle lift (Z/D = 0.5 m/s, V = 11.6 m/s) and high needle lift (Z/D = 3, V = 10.6 m/s), respectively. The results were obtained by averaging 500 sample results. From Figure 5.16 (a), it is clear that in the center area of the sac under very low needle lift condition, the flow appears to be going in the upward direction (indicated with blue color), which confirms the vortical flow in the sac. While in the Figure 5.16 (b), the flows near the center direct downward due to small inflow velocity to the sac.

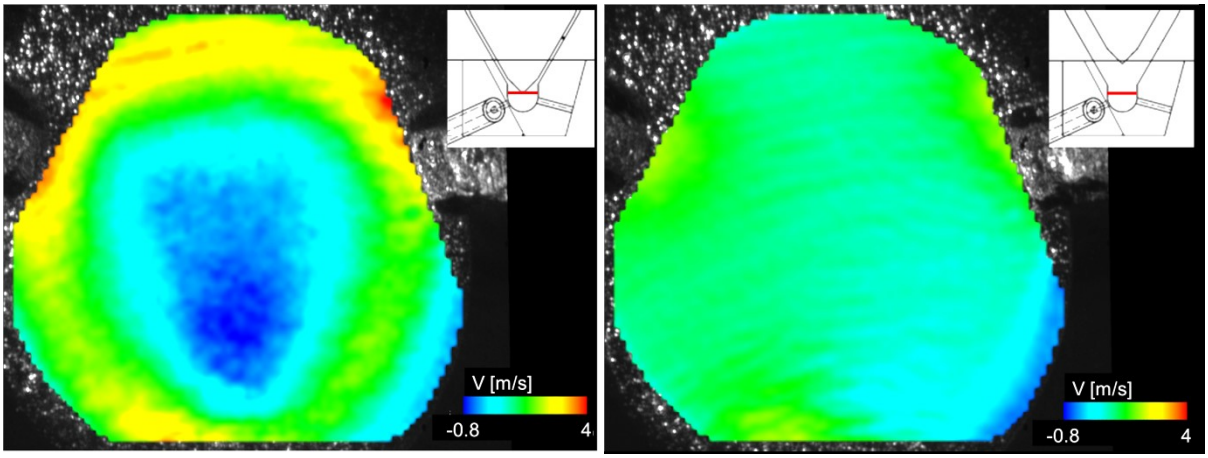

(a) Z/D = 0.5, V = 11.6 m/s (b) Z/D = 3, V = 10.6 m/s

Figure 5.16 Contour map of scalar velocity in downward direction of the sac plane (view from sac bottom)

Figure 5.17 (a) and (b) show the contour maps of the magnitude of the horizontal velocity for very low needle lift (Z/D = 0.5 m/s, V = 11.6 m/s) and high needle lift (Z/D = 3, V = 10.6 m/s), respectively. The results were obtained by averaging 500 sample results. In the

case of very low needle lift shown in Figure 5.17 (a), velocity near the holes is large and not symmetric, while in the case of high needle lift, the velocity contour shown in Figure 5.17 (b) seems rotational symmetry.

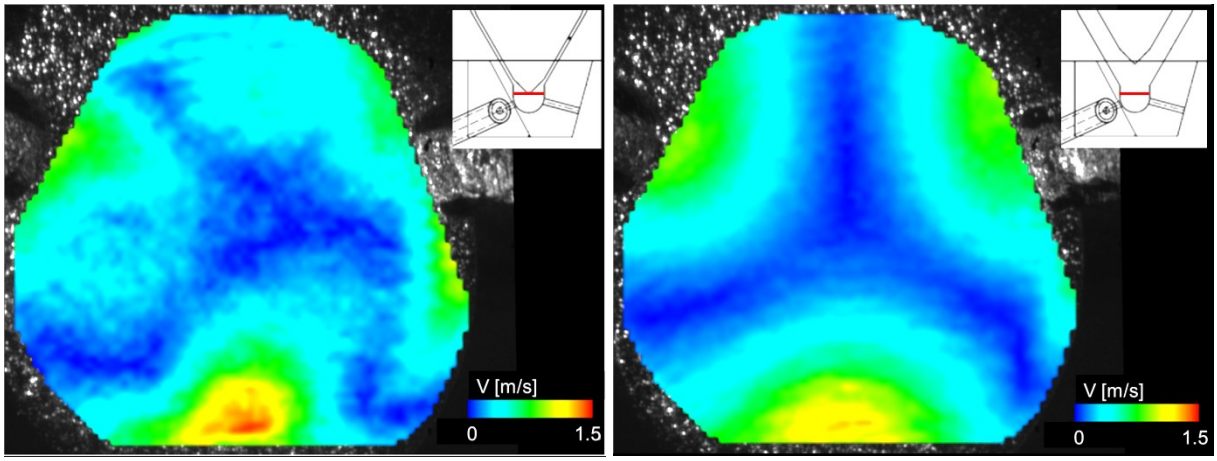

(a) Z/D = 0.5, V = 11.6 m/s (b) Z/D = 3, V = 10.6 m/s

Figure 5.17 Contour map of scalar velocity in plane direction at the sac plane (view from sac bottom)

Additional PIV experiment was conducted to obtain 2D velocity distribution in the vertical plane for very low needle lift condition (Z/D = 0.5) and super cavitation condition (V = 11.6 m/s). As shown in Figure 5.18, a good agreement with 2D mini-sac nozzle result that the incoming flow from the needle gap into the sac entrance is fast and separation flow with a certain velocity vector and magnitude was obtained. This confirms that the 2D mini-sac nozzle model is useful to represent the real mini-sac nozzle.

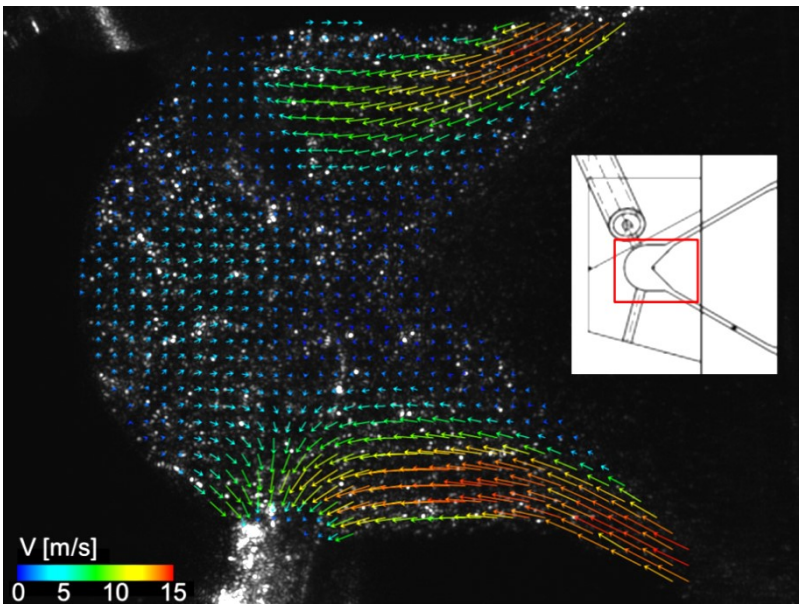

Figure 5.18 Averaged velocity-vector results of PIV in the sac center longitudinal plane at Z/D = 0.5, V = 11.6 m/s (view from front)

5.4 Summary

In this study, cavitation in real shape mini-sac nozzle with 3-holes was investigated. Experiment by two different fluids, i.e. water and sodium iodide solution, was conducted. The sodium iodide solution was used for refractive index matching. The needle lift was varied to understand its effects on cavitation and the injected liquid jets as well as to understand the internal flow pattern in the sac. Injection pressure is varied to observe the cavitation pattern under various mean flow velocities V in the nozzle. Stereoscopic particle image velocimetry (PIV) analysis was carried out to examine the velocity distribution in the sac. As a result, the following conclusions were obtained.

(1) For low needle lift case ($Z/D \leq 1$), a thin string cavitation occurs in the sac surrounded by vortical flow.

(2) Even in very high velocity, hydraulic flip does not completely occur and the jet angle does not decrease, while in the case of higher needle lift ($Z/D = 2, 3$), the jet angle is suppressed when the cavitation turns to hydraulic flip.

(3) Cavitation occurrences for the two liquids are different in mean flow velocity V due to the different liquid density ρ. Thus, generalization was made by expressing the cavitation number σ instead of mean flow velocity V. The result shows that cavitation extends to super cavitation when cavitation number $\sigma = 1 \pm 0.05$ for both liquid cases.

(4) In the center of the sac under very low needle lift condition, flow appears to be going in the upward direction which is the reason of the formation of vortical flow and string cavitation.

Chapter 6
Conclusions

In this study, cavitation in nozzles of fuel injectors for diesel engines was investigated using some nozzles with simplified geometry and real injector geometry. The experiment was conducted to understand how cavitation forms and affects the injected liquid jet. Two-dimensional and cylindrical nozzles with a simple asymmetric inflow and complex inflow through the sac were used in order to reveal the effects of nozzle geometry on cavitation and liquid jet deformation. As a result, the following conclusions were obtained in the study:

- With an asymmetric inflow, cavitation occurs asymmetrically and the liquid jet behaves asymmetrically especially when needle lift is low. A higher needle lift results in smaller lateral inflow momentum and, therefore, thinner cavitation which results in shorter cavitation and smaller liquid jet angle.
- An asymmetric cavitation induces asymmetric liquid jet and spray. Velocity distribution of the injected liquid jets is not uniform, that is, the cavitating side of the jet has slower velocity than the non-cavitating side, which induces non-uniform velocity distribution of injected spray.
- When a cavitation cloud was shed from the nozzle it had a large impact on liquid jet deformation.
- Modified cavitation number based on local pressure at vena contracta can be utilized to quantitatively predict the onset and development of cavitation in nozzles.

- In cylindrical nozzle with a lateral inflow, the thick string cavitation and the resulting swirling hollow cone liquid skirt at low needle lift. On the other hand, at high needle lift string cavitation is never observed even at high flow rate and the boundary between low lift with string cavitation and high lift with no string cavitation does not depend on liquid flow rate. Special attention needs to be paid when we use a multi-hole fuel injector at middle needle lift, which may result in occasional string cavitation and unstable hollow cone liquid skirt.
- At narrow upper-volume of $W_U/D = 3.75$, which represents the case with a large nozzle-hole number, the swirling flow in the upstream channel and the resulting string cavitation only appears at very low needle lift of $Z/D < 1$ due to the limitation in the upstream space.
- Simulated pressure distribution agrees with observed slanted string cavitation profile at low lift.
- Thick string cavitation and the resulting hollow cone liquid skirt can be initiated by the conversion from the large lateral inflow momentum to the axial momentum in the nozzle hole within a narrow space at low needle lift even if the structure of the injector

is very simple. The condition of the string cavitation formation can be estimated by simply knowing the lateral inflow momentum, needle lift and upstream channel width.

- In mini-sac nozzle, small needle angle and low needle lift lead to a large lateral inflow velocity component and result in a thick and long cavitation, which is the cause of large cavitation clouds and large jet angle.
- Large needle angle increases the turbulence of the inflow, which increases the fluctuations of cavitation length, cavitation thickness, and liquid jet angle even at hydraulic flip.
- For large nozzle angle, cavitation clouds shed from the tail of the sheet cavitation are large due to a thick sheet formation downstream of the acute inlet edge, which leads to large jet angle.
- By knowing the angle of inlet velocity near the nozzle inlet edge which can be derived from PIV analysis or CFD, cavitation thickness and length can be predicted. The angle of inlet velocity is governed by the nozzle geometry.
- A large vertical flow structure which is induced by cavitation cloud shedding and causes large liquid jet deformation was measured by PIV analysis, which has been guessed in previous studies.

- In mini-sac nozzle with real 3D geometry for low needle lift cases ($Z/D \leq 1$), a thin string cavitation and large vortical flow structure appear in the sac. As a result, total hydraulic flip does not occur even at very high velocity, and the jet angle is large. On the other hand, in the case of high needle lift ($Z/D \geq 2$), the jet angle is suppressed when the cavitation turns to hydraulic flip.
- At the center of the sac under low needle lift condition, the flow appears to be going in the reverse direction than the surrounding flow and makes a recirculation flow. This should be the main cause of vortical flow formation in the sac, which leads to a string cavitation phenomenon.

It was found that cavitation in nozzle-hole of fuel injector is mainly determined by the angle of inlet flow to the nozzle, which is affected by the nozzle-hole upstream geometry, such as needle lift and sac geometry. By knowing the inflow angle by PIV or CFD and the mean flow velocity, we can estimate cavitation thickness, cavitation length by introducing the modified cavitation number, the diameter of cavitation cloud, and the liquid jet angle. It should be noted that string cavitation takes place at low needle lift and wide upstream channel width and at the transition regime string cavitation becomes unstable, and the injected liquid jet also becomes unstable. Based on the above knowledge, we can control cavitation and establish a new strategy to design new fuel injectors.

Bibliography

[1] European Parliament and Council of the European Union, "Regulation (EC) No 715/2007 of the European Parliament and of the Council of 20 June 2007 on type approval of motor vehicles with respect to emissions from light passenger and commercial vehicles (Euro 5 and Euro 6) and on access to vehicle repair and mai," *Off. J. Eur. Union*, vol. L171, no. December 2006, pp. 1–16, 2007.

[2] Lord Rayleigh, "On the pressure developed in a liquid during the collapse of a spherical cavity," *Philos. Mag. Ser. 6*, vol. 34, no. 200, pp. 94–98, 1917.

[3] M. S. Plesset, "The dynamics of cavitation bubbles," *J. Appl. Mech.*, vol. 16, no. 3, pp. 277–282, 1949.

[4] C. E. Brennen, *Cavitation and bubble dynamics*, vol. 9, no. 1. 1977.

[5] R. Payri, F. J. Salvador, J. Gimeno, and J. de la Morena, "Study of cavitation phenomena based on a technique for visualizing bubbles in a liquid pressurized chamber," *Int. J. Heat Fluid Flow*, vol. 30, no. 4, pp. 768–777, 2009.

[6] R. E. A. Arndt, "Cavitation in Vortical Flows," *Annu. Rev. Fluid Mech.*, vol. 34, pp. 143–175, 2002.

[7] J. Choi, C.-T. Hsiao, G. Chahine, and S. Ceccio, "Growth, oscillation and collapse of vortex cavitation bubbles," *J. Fluid Mech.*, vol. 624, pp. 255–279, 2009.

[8] A. Philipp and W. Lauterborn, "Cavitation erosion by single laser-produced bubbles," *J. Fluid Mech.*, vol. 361, pp. 75–116, 1998.

[9] W. K. Chan, "Detection of cavitation erosion in centrifugal pumps," *Int. J. Heat Fluid Flow*, vol. 9, no. 1, pp. 74–77, 1988.

[10] D. Bertetta, S. Brizzolara, S. Gaggero, M. Viviani, and L. Savio, "CPP propeller cavitation and noise optimization at different pitches with panel code and validation by cavitation tunnel measurements," *Ocean Eng.*, vol. 53, pp. 177–195, 2012.

[11] M. K. Khair and H. Jääskeläinen, "Diesel Fuel Injection." [Online]. Available: https://www.dieselnet.com/tech/diesel_fi.php. [Accessed: 19-Apr-2016].

[12] S. Moon, Y. Matsumoto, and K. Nishida, "Entrainment, Evaporation and Mixing Characteristics of Diesel Sprays around End-of-Injection," *SAE Tech. Pap.*, 2009.

[13] E. Villermaux, P. Marmottant, and J. Duplat, "Ligament-Mediated Spray Formation," *Phys. Rev. Lett.*, vol. 92, no. 7, p. 074501, 2004.

[14] D. Potz, W. Christ, and B. Dittus, "Diesel system – The determining interface between injection system and combustion chamber," *Thermo-and Fluid-Dynamic Process. Diesel Engines*, pp. 133–143, 2002.

[15] B. Mahr, "Future and Potential of Diesel Injection Systems," *Proc. THIESEL 2002 Conf. Thermo- Fluid-Dynamic Process. Diesel Engines*, pp. 5–17, 2002.

[16] W. Bergwerk, "Flow pattern in diesel nozzle spray holes," *Arch. Proc. Inst. Mech. Eng. 1847-1982 (vols 1-196)*, vol. 173, no. 1959, pp. 655–660, Jun. 1959.

[17] H. Hiroyasu, M. Arai, and M. Shimizu, "Break-up Length of a Liquid Jet and Internal

Flow in a Nozzle," in *Proc. 5th. ICLASS (1991)*, 1991, pp. 275–282.

[18] H. Hiroyasu, M. Arai, and M. Shimizu, "Effect of Internal Flow Conditions Inside Injector Nozzles on Jet Breakup Processes," in *Recent advances in spray combustion: Spray atomization and drop burning phenomena. Volume I*, K. K. Kuo, Ed. American Institute of Aeronautics ad Astronautics, Inc., 1995, pp. 173–184.

[19] H. Chaves, M. Knapp, A. Kubitzek, F. Obermeier, and T. Schneider, "Experimental Study of Cavitation in the Nozzle Hole of Diesel Injectors Using Transparent Nozzles," *SAE Tech. Pap.*, Feb. 1995.

[20] L. C. Ganippa, G. Bark, S. Andersson, and J. Chomiak, "Comparison of Cavitation Phenomena in Transparent Scaled-up Single-Hole Diesel Nozzles," in *Cav2001*, 2001.

[21] C. Stanley, T. Barber, B. Milton, and G. Rosengarten, "Periodic cavitation shedding in a cylindrical orifice," *Exp. Fluids*, vol. 51, no. 5, pp. 1189–1200, 2011.

[22] C. Stanley, G. Rosengarten, B. Milton, and T. Barber, "Investigation of Cavitation in a Large-Scale Transparent Nozzle," in *FISITA 2008 Student Congress*, 2008.

[23] Z. He, Z. Shao, Q. Wang, W. Zhong, and X. Tao, "Experimental study of cavitating flow inside vertical multi-hole nozzles with different length–diameter ratios using diesel and biodiesel," *Exp. Therm. Fluid Sci.*, vol. 60, pp. 252–262, 2015.

[24] A. Sou, S. Hosokawa, and A. Tomiyama, "Effects of cavitation in a nozzle on liquid jet atomization," *Int. J. Heat Mass Transf.*, vol. 50, no. 17–18, pp. 3575–3582, 2007.

[25] A. Sou, M. I. Maulana, S. Hosokawa, and A. Tomiyama, "Ligament Formation Induced by Cavitation in a Cylindrical Nozzle," *J. Fluid Sci. Technol.*, vol. 3, no. 5, pp. 633–644, 2008.

[26] A. Sou, S. Hosokawa, and A. Tomiyama, "Cavitation in Nozzles of Plain Orifice Atomizers with Various Length-to-Diameter Ratios," *At. Sprays*, vol. 20, no. 6, pp. 513–524, 2010.

[27] K. Ramamurthi and S. Patnaik, "Influence of periodic disturbances on inception of cavitation in sharp-edged orifices," *Exp. Fluids*, vol. 33, no. 5, pp. 720–727, 2002.

[28] S. H. Park, H. K. Suh, and C. S. Lee, "Effect of Cavitating Flow on the Flow and Fuel Atomization Characteristics of Biodiesel and Diesel Fuels," *Energy & Fuels*, vol. 22, no. 1, pp. 605–613, 2008.

[29] H. K. Suh and C. S. Lee, "Effect of cavitation in nozzle orifice on the diesel fuel atomization characteristics," *Int. J. Heat Fluid Flow*, vol. 29, no. 4, pp. 1001–1009, 2008.

[30] H. K. Suh, S. H. Park, and C. S. Lee, "Experimental investigation of nozzle cavitating flow characteristics for diesel and biodiesel fuels," *Int. J. Automot. Technol.*, vol. 9, no. 2, pp. 217–224, Apr. 2008.

[31] J. Hult, P. Simmank, S. Matlok, S. Mayer, Z. Falgout, and M. Linne, "Interior flow and near-nozzle spray development in a marine-engine diesel fuel injector," *Exp. Fluids*, vol. 57, no. 4, p. 49, 2016.

[32] C. Mauger, L. Méès, M. Michard, A. Azouzi, and S. Valette, "Shadowgraph, Schlieren and interferometry in a 2D cavitating channel flow," *Exp. Fluids*, vol. 53, no. 6, pp. 1895–1913, 2012.

[33] C. Mauger, L. Méès, M. Michard, and M. Lance, "Velocity measurements based on shadowgraph-like image correlations in a cavitating micro-channel flow," *Int. J. Multiph. Flow*, vol. 58, pp. 301–312, 2014.

[34] C. Badock, R. Wirth, A. Fath, and A. Leipertz, "Investigation of cavitation in real size diesel injection nozzles," *Int. J. Heat Fluid Flow*, vol. 20, no. 5, pp. 538–544, 1999.

[35] R. Miranda, H. Chaves, U. Martin, and F. Obermeier, "Cavitation in an asymmetric transparent real size VCO nozzle," in *Proc. ICLASS (2003)*, 2003, pp. 3–10.

[36] S. H. Collicott and H. Li, "True-scale True-pressure Internal Flow Visualization for Diesel Injectors," *SAE Tech. Pap.*, vol. 2006, Apr. 2006.

[37] N. Mitroglou, M. McLorn, M. Gavaises, C. Soteriou, and M. Winterbourne, "Instantaneous and ensemble average cavitation structures in Diesel micro-channel flow orifices," *Fuel*, vol. 116, pp. 736–742, 2014.

[38] N. Mitroglou, M. Gavaises, J. M. Nouri, and C. Arcoumanis, "Cavitation Inside Enlarged and Real-Size Fully Transparent Injector Nozzles and Its Effect on Near Nozzle Spray Formation," in *DIPSI Workshop 2011 on Droplet Impact Phenomena & Spray Investigation*, 2011.

[39] C. Arcoumanis, M. Gavaises, J. M. Nouri, E. Abdul-Wahab, and R. W. Horrocks, "Analysis of the Flow in the Nozzle of a Vertical Multi-Hole Diesel Engine Injector," *SAE Tech. Pap.*, no. 724, 1998.

[40] C. Arcoumanis, H. Flora, M. Gavaises, N. Kampanis, and R. Horrocks, "Investigation of cavitation in a vertical multi-hole injector," *SAE Tech. Pap.*, vol. 108, pp. 661–678, Mar. 1999.

[41] H. Roth, M. Gavaises, and C. Arcoumanis, "Cavitation Initiation, Its Development and Link With Flow Turbulence in Diesel Injector Nozzles," *SAE 2002 World Congr. Exhib.*, vol. 2002, no. 724, 2002.

[42] T. Hayashi, M. Suzuki, and M. Ikemoto, "Visualization of Internal Flow and Spray Formation with Real Size Diesel Nozzle," in *12th International Conference on Liquid Atomization and Spray Systems (ICLASS 2012)*, 2012.

[43] T. Hayashi, M. Suzuki, and M. Ikemoto, "Effects of internal flow in a diesel nozzle on spray combustion," *Int. J. Engine Res.*, vol. 14, no. 6, pp. 646–654, Dec. 2013.

[44] C. Soteriou, R. J. Andrews, N. Torres, M. Smith, and R. Kunkulagunta, "Through the Diesel Nozzle Hole - A Journey of Discovery II," in *Annual Meeting of the Institute for Liquid Atomization and Spray Systems Europe*, 2001.

[45] A. Andriotis, M. Gavaises, and C. Arcoumanis, "Vortex flow and cavitation in diesel injector nozzles," *J. Fluid Mech.*, vol. 610, p. 153, Sep. 2008.

[46] B. a. Reid, G. K. Hargrave, C. P. Garner, and R. M. McDavid, "An optical comparison of the cavitation characteristics of diesel and bio-diesel blends in a true-scale nozzle geometry," *Int. J. Engine Res.*, vol. 14, no. 6, pp. 622–629, 2013.

[47] S. Martynov, D. Mason, M. R. Heikal, S. S. Sazhin, and M. Gorokhovski, "Modelling of Cavitation Flow in a Nozzle and Its Effect on Spray Development," *Jets*, 2006.

[48] B. Argueyrolles, S. Dehoux, P. Gastaldi, L. Grosjean, F. Levy, A. Michel, and D. Passerel, "Influence of injector nozzle design and cavitation on coking phenomenon,"

SAE Tech. Pap., pp. 1405–1415, 2007.

[49] J. Ishimoto, "Integrated Computation of Micro-Cavitation in Gasoline Injector Atomization," in *11th Triennial International Conference on Liquid Atomization and Spray Systems (ICLASS 2009)*, 2009.

[50] H. Watanabe, M. Nishikori, T. Hayashi, M. Suzuki, N. Kakehashi, and M. Ikemoto, "Visualization analysis of relationship between vortex flow and cavitation behavior in diesel nozzle," *Int. J. Engine Res.*, vol. 16, no. 1, pp. 5–12, Jan. 2015.

[51] Wikipedia, "Flow visualization," 2016. [Online]. Available: https://en.wikipedia.org/wiki/Flow_visualization. [Accessed: 22-Jun-2016].

[52] W. Merzkirch, *Flow Visualization*, 2ndEdition ed. Academic Press, Inc., 1987.

[53] H. Löffelmann, "Visualizing Local Properties and Characteristic Structures of Dynamical Systems," Vienna University of Technology, 1998.

[54] J. B. Ghandhi and D. M. Heim, "An optimized optical system for backlit imaging," *Rev. Sci. Instrum.*, vol. 80, no. 5, pp. 80–83, 2009.

[55] M. Versluis, "High-speed imaging in fluids," *Exp. Fluids*, vol. 54, no. 2, 2013.

[56] J. D. Hrubes, "High-speed imaging of supercavitating underwater projectiles," *Exp. Fluids*, vol. 30, no. 1, pp. 57–64, 2001.

[57] R. J. H. Klein-Douwel, P. J. M. Frijters, L. M. T. Somers, W. A. de Boer, and R. S. G. Baert, "Macroscopic diesel fuel spray shadowgraphy using high speed digital imaging in a high pressure cell," *Fuel*, vol. 86, no. 12–13, pp. 1994–2007, 2007.

[58] V. Sick, M. C. Drake, and T. D. Fansler, "High-speed imaging for direct-injection gasoline engine research and development," *Exp. Fluids*, vol. 49, no. 4, pp. 937–947, 2010.

[59] C. Crua, T. Shoba, M. Heikal, M. Gold, and C. Higham, "High-speed microscopic imaging of the initial stage of diesel spray formation and primary breakup," *SAE Int.*, vol. 28, pp. 1085–1092, 2010.

[60] E. W. Eagle, S. B. Morris, and M. S. Wooldridge, "High-speed imaging of transient diesel spray behavior during high pressure injection of a multi-hole fuel injector," *Fuel*, vol. 116, pp. 299–309, 2014.

[61] A. K. Prasad, "Particle Image Velocimetry," *Curr. Sci.*, vol. 79, no. 1, pp. 51–60, 2000.

[62] C. E. Willert and M. Gharib, "Digital particle image velocimetry," *Exp. Fluids*, vol. 10, no. 4, pp. 181–193, 1991.

[63] J. Westerweel, "Fundamentals of digital particle image velocimetry," *Meas. Sci. Technol.*, vol. 8, no. 12, pp. 1379–1392, 1997.

[64] J. G. Santiago, S. T. Wereley, C. D. Meinhart, D. J. Beebe, and R. J. Adrian, "A particle image velocimetry system for microfluidics," *Exp. Fluids*, vol. 25, no. 4, pp. 316–319, 1998.

[65] a. K. Prasad, "Stereoscopic particle image velocimetry," *Exp. Fluids*, vol. 29, no. 2, pp. 103–116, 2000.

[66] R. J. Adrian, "Twenty years of particle image velocimetry," *Exp. Fluids*, vol. 39, no. 2,

pp. 159–169, 2005.

[67] M. Jahanmiri, “Particle Image Velocimetry: Fundamentals and Its Applications,” 2011.

[68] A. K. Prasad and R. J. Adrian, “Stereoscopic particle image velocimetry applied to liquid flows,” *Exp. Fluids*, vol. 15, no. 1, pp. 49–60, 1993.

[69] M. Gaydon, M. Raffel, C. Willert, M. Rosengarten, and J. Kompenhans, “Hybrid stereoscopic particle image velocimetry,” *Exp. Fluids*, vol. 23, no. 4, pp. 331–334, 1997.

[70] A. Liberzon, R. Gurka, and G. Hetsroni, “XPIV-Multi-plane stereoscopic particle image velocimetry,” *Exp. Fluids*, vol. 36, no. 2, pp. 355–362, 2004.

[71] R. Lindken, J. Westerweel, and B. Wieneke, “Stereoscopic micro particle image velocimetry,” *Exp. Fluids*, vol. 41, no. 2, pp. 161–171, 2006.

[72] C. Soteriou, R. Andrews, and M. Smith, “Direct Injection Diesel Sprays and the Effect of Cavitation and Hydraulic Flip on Atomization,” *SAE Tech. Pap.*, 1995.

[73] A. Sou, M. I. Maulana, K. Isozaki, S. Hosokawa, and A. Tomiyama, “Effects of Nozzle Geometry on Cavitation in Nozzles of Pressure Atomizers,” *J. Fluid Sci. Technol.*, vol. 3, no. 5, pp. 622–632, 2008.

[74] M. Gavaises, “Flow in valve covered orifice nozzles with cylindrical and tapered holes and link to cavitation erosion and engine exhaust emissions,” *Int. J. Engine Res.*, vol. 9, no. 6, pp. 435–447, 2008.

[75] H. Chaves and C. Ludwig, “Characterization of cavitation in transparent nozzles depending on the nozzle geometry,” in *Proceedings of the 20th ILASS - Europe Meeting 2005*, 2005.

[76] A. Sou, R. H. Pratama, T. Tomisaka, and Y. Kibayashi, “Cavitation Flow in Nozzle of Liquid Injector,” in *International Conference on Liquid Atomization and Spray Systems (ICLASS 2012)*, 2012.

[77] K. Bai and J. Katz, “On the refractive index of sodium iodide solutions for index matching in PIV,” *Exp. Fluids*, vol. 55, no. 4, p. 1704, 2014.

[78] I. D. Zaytsev and G. G. Aseyev, *Properties of aqueous solutions of electrolytes*. CRC press, 1992.

[79] K. R. Patil, A. D. Tripathi, G. Pathak, and S. S. Katti, “Thermodynamic properties of aqueous electrolyte solutions. 2. Vapor pressure of aqueous solutions of sodium bromide, sodium iodide, potassium chloride, potassium bromide, potassium iodide, rubidium chloride, cesium chloride, cesium bromide, cesium iodide,” *J. Chem. Eng. Data*, vol. 36, no. 2, pp. 225–230, 1991.

[80] N. Matubayasi, K. Tsunemoto, I. Sato, R. Akizuki, A. Matuzawa, and Y. Natsukari, “Thermodynamic Quantities of Surface Formation of Aqueous Electrolyte Solutions.,” *J. Colloid Interface Sci.*, vol. 243, pp. 444–456, 2001.

[81] D. R. Lide, *CRC Handbook of Chemistry and Physics 86TH Edition 2005-2006*. 2005.

[82] T. L. Brown, H. E. LeMay, B. E. Bursten, C. J. Murphy, and P. M. Woodward, *Chemistry: The Central Science*, 12th ed. Pearson Prentice Hall.

[83] “Revised Release on Surface Tension of Ordinary Water Substance,” Moscow, 2014.

List of Publications

This PhD dissertation is written based on the following papers:

Journal Papers:

(1) Akira Sou and Raditya Hendra Pratama: Effects of Asymmetric Inflow on Cavitation in Fuel Injector and Discharged Liquid Jet, Atomization and Sprays, Volume 26, Issue 9, 2016.

(2) Raditya Hendra Pratama, Akira Sou, Tokihiro Katsui, and Shigeru Nishio: String Cavitation in a Fuel Injector, Atomization and Sprays, forthcoming article.

Conference Papers:

(1) Akira Sou, Raditya Hendra Pratama, and Tsuyoshi Tomisaka: Cavitation in a Nozzle of Fuel Injector, Proceedings of the 8th International Symposium on Cavitation, CAV2012 – Submission No. 48, 2012.

(2) Raditya Hendra Pratama and Akira Sou: String Cavitation in Fuel Injector, Proceedings of 16th Conference of the Institute for Liquid Atomization and Spray Systems – Asia (ILASS-Asia 2013), No. A131, 2013.

(3) Raditya Hendra Pratama, Akira Sou, Yoshitaka Wada, and Hideaki Yokohata: Cavitation in Mini-Sac Nozzle and Injected Liquid Jet, Proceedings of 8th Conference on Thermo- and Fluid Dynamic Processes in Direct Injection Engines (THIESEL 2014), No. A.2.1, 2014.

(4) Raditya Hendra Pratama, Akira Sou, Yoshitaka Wada, Hideaki Yokohata, "Cavitation Flow in Nozzle of Liquid Injector Cavitation in Mini-Sac Nozzle and Injected Liquid Jet", Proceedings of 13th International Conference on Liquid Atomization and Spray Systems (ICLASS 2015), No. 216, 2015.